Implementation of novel sensors on underwater gliders

Michael P. Hemming

To cite this version:

Michael P. Hemming. Implementation of novel sensors on underwater gliders. Oceanography. Sorbonne Université; University of East Anglia, 2018. English. NNT : 2018SORUS612 . tel-03292856

Implementation of Novel Sensors on Underwater Gliders

A thesis submitted jointly to the
School of Environmental Sciences
University of East Anglia and
Laboratoire d’Océanographie et du Climat
Université de Pierre et Marie Curie
in partial fulfilment of the co-tutelle agreement and
the requirements for the degree of
Doctor of Philosophy

Michael Paul Hemming

October 2018

Thése de doctorat de l'université Pierre et Marie Curie dans le cadre de l'accord co-tutelle avec l'université d'East Anglia.

Sujet de la thése :

Implementation of Novel Sensors on Underwater Gliders

Spécialité : Océanographie Physique et Biogéochimie

École doctorale des Sciences de l'Environnement d'Ile de France (ED 129)

réalisée au

Laboratoire d'Océanographie et du Climat : Expérimentations et Approches Numériques

présentée par

Michael Paul HEMMING

pour obtenir le grade de :

Docteur de l'université Pierre et Marie Curie et l'université d'East Anglia

Soutenue le 20 Décembre 2018 à l'université d'East Anglia

devant le jury composé de:

Dr.	S. Henson	Rapporteuse	University of Southampton
Dr.	A. Manning	Rapporteur	University of East Anglia
Dr.	P. Testor	Examinateur	Université Pierre et Marie Curie

Supervisors:
Prof. Dr. Jan Kaiser,
Prof. Dr. Karen Heywood,
Dr. Jacqueline Boutin,
Dr. Dorothee Bakker

DSTL and DGA supervision:
Tim Clarke,
Carole Nahum

Defence jury:
Dr. Pierre Testor
(LOCEAN examiner: external UEA, internal LOCEAN),
Dr. Andrew Manning
(LOCEAN Reporter: internal UEA, external LOCEAN),
Dr. Stephanie Henson
(LOCEAN Reporter: external UEA, external LOCEAN)

Abstract

Around a quarter of global anthropogenic carbon emissions have been absorbed by the ocean. Underwater gliders have been identified as important tools for gathering information related to climate change and ocean acidification processes.

The REP14 - MED experiment involved the deployment of eleven gliders in the northwestern Mediterranean Sea; one of these had an experimental ion sensitive field effect transistor (ISFET) sensor attached. A comparison between pH observed by the glider and ship during the deployment indicated problems with the sensor accuracy and stability. Sunlight caused an apparent sensor pH decrease of up to 0.1 close to the surface around local noon. The pH corrected for drift, temperature, and pressure is presented with other ocean variables measured by the glider.

The timing of the phytoplankton spring bloom in the northwestern Mediterranean Sea varies year-on-year. A glider with an ISFET pH sensor was deployed close to the BOUSSOLE mooring site. This deployment offered a second opportunity to test the ISFET sensor with improvements. Similarly to during the REP14 - MED experiment, ISFET pH measurements were corrected for drift, temperature and pressure effects. Measurements at the BOUSSOLE mooring indicated that the spring bloom started around March 19. Mean net community production (N) rates were estimated from the glider dissolved oxygen concentrations, as well as glider and buoy dissolved inorganic carbon concentrations derived using other parameters. N ranged between $-82 \pm 317\,\mathrm{mmol\,m^{-2}\,d^{-1}}$ and $460 \pm 870\,\mathrm{mmol\,m^{-2}\,d^{-1}}$.

Horizontal spatial scales of variability highlight physical and biogeochemical processes, and are useful for designing ocean observing systems. Spatial scales of variability were estimated from semivariograms using glider measurements. Spatial scales of variability were mostly small at depths affected by biology, and large at depths affected by large-scale processes, such as weather, although this was not true in every case. Some direction-dependency was found, which may be related to ocean currents, or the density of glider meridional measurements.

keywords: pH sensor; underwater gliders; biogeochemistry; net community production; spatial scales; northwestern Mediterranean Sea

Résumé

Aujourd'hui environ un quart des émissions globales de carbone anthropique a été absorbé par l'océan. Cet accroissement de la concentration en CO_2 a fait augmenter l'acidité de l'océan ce qui peut impacter les organismes calcifiants dû à des changements dans la chimie des carbonates de l'eau de mer. Récemment des planneurs ('gliders') sous-marins ont été identifiés comme des outils importants pour recueillir des informations reliées au changement climatique et aux processus d'acidification.

Durant l'expérience REP14-MED en juin 2014, 11 gliders ont été déployés au large de la côte de Sardaigne en mer Méditerranée nord occidentale. Un capteur expérimental ISFET (Ion Sensitive Field Effect Transistor) mesurant le pH a été testé sur l'un de ces gliders. Une comparaison entre les mesures de pH recueillies par le glider et par le bateau durant le déploiement témoigne de problèmes concernant la précision absolue et la stabilité de l'instrument. Un biais constant en profondeur et variable en temps a été appliqué afin de compenser la dérive multidirectionnelle du capteur et les mesures de température et pression ont été corrigées. De plus, la lumière du soleil a provoqué une diminution apparente du pH pouvant atteindre jusqu'à 0,1 près de la surface vers midi. Cela a mis en évidence l'importance de protéger le capteur de la lumière lors de futurs déploiements. Le pH corrigé présenté avec les autres variables océaniques mesurées par le glider illustrent des liens clairs avec les processus physiques et biogéochimique.

En mer Méditerranée nord occidentale, la date de début du bloom phytoplanctonique printanier varie d'une année à l'autre, entre mars et avril. En mars 2016, un glider équipé d'un capteur ISFET a été déployé près des bouées BOUSSOLE / DyFAMed en mer Méditerranée nord occidentale. Ce déploiement a fourni une seconde opportunité de tester un capteur ISFET modifié visant à accroître la stabilité et à réduire l'effet de la lumière du soleil. Comme lors de l'expérience REP14-MED, les mesures de pH de l'ISFET ont été corrigées pour tenir compte des effets de la dérive, de la température et de la pression. Le glider a mesuré la variabilité horizontale et verticale des paramètres physiques et biogéochimiques à l'approche d'un bloom printanier. La fugacité de CO_2 (fCO_2) mesurée par un capteur CARIOCA une bouée biogéochimique au site de la BOUSSOLE à 10 m de profondeur a décru très fortement entre le 19 mars et le 1er avril, suivant une période d'intense mélange. La fugacité du CO_2 et l'alcalinité totale à la bouée BOUSSOLE ont été utilisées pour calculer les concentrations de carbone inorganique dissous. Les concentrations d'oxygène á dissous, pH et rétrodiffusion optique observés par le glider á 10 m ont augmenté entre le 19 mars et le 1er avril, indiquant le démarrage du bloom phytoplanctonique. Les taux de production biologique communautaire nette moyenne (N) ont été estimés á partir des concentrations d'oxygéne dissous mesurées par glider et á partir de concentrations de carbon inorganique dissous déduites des mesures ISFET (glider) et mouillage. Aprés mi-mars durant le déploiment. Les estimations de N varient entre -82 ± 317 mmol m^{-2} d^{-1} and 460 ± 870 mmol m^{-2} d^{-1}.

Les échelles spatiales de variabilité mettent en évidence l'influence des processus océaniques sur les paramètres physiques et biogéochimiques, et sont utiles pour la conception de systèmes d'observation de l'océan. Les échelles spatiales de variabilité horizontales ont été estimées à partir de semi-variogrammes utilisant les mesures des déploiements REP14-MED et BOUSSOLE/DYFAMED. Dans l'ensemble, les échelles spatiales étaient plus petites aux profondeurs affectéés par la photosynthèse (par exemple, là où se forment des patchs de chlorophylle) et plus grandes aux profondeurs affectées par des processus à grande échelle, tels que le forçage atmosphérique. Les échelles longitudinales sont en général plus longues que les échelles zonales. Cette anisotropie peut être liée aux courants océaniques ou au peu de mesures par glider provenant de la zone Sud. Les modèles de semi variogramme utilisés pour extraire les caractéristiques n'ont pas obtenu les mêmes résultats que dans d'autres études (plus faible valeur r^2). Un ensemble plus large et plus complet de données de glider serait nécessaire dans le futur pour améliorer la performance des modèles semi-variogrammes.

Mots clés: pH sensor; underwater gliders; biogeochemistry; net community production; spatial scales; northwestern Mediterranean Sea

Contents

List of Figures

List of Tables

Publications

Research and collaborative activity completed during this PhD project has led to the following publications:

Onken, R., Fiekas, H., Beguery, L., Borrione, I., Funk, A., **Hemming, M. P.**, Heywood, K. J., Kaiser, J., Knoll, M., Poulain, P., Queste, B., Russo, A., Shitashima, K., Siderius, M., Thorp-Küsel, E.: 'High-Resolution Observations in the Western Mediterranean Sea: The REP14-MED Experiment', Ocean Science, 14, 321-335, (2018), doi:10.5194/os-14-321-2018.

Knoll, M., Borrione, I., Fiekas, H. V., Funk, A., **Hemming, M. P.**, Kaiser, J., Onken, R., Queste, B. and Russo, A.: 'Hydrography and Circulation West of Sardinia in June 2014', Ocean Science, 13, 889-904, (2017) doi:10.5194/os-13-889-2017.

Hemming, M. P., Kaiser, J., Heywood, K. J., Bakker, D. C. E., Boutin, J., Shitashima, K., Lee, G., Legge, O., Onken, R.: Measuring pH variability using an experimental sensor on an underwater glider', Ocean Science, 13, 427-442, (2017), doi:10.5194/os-13-427-2017

List of Acronyms

MAW	Modified Atlantic Water
LIW	Levantine Intermediate Water
WIW	Winter Intermediate Water
WMDW	Western Mediterranean Deep Water
EMDW	Eastern Mediterranean Deep Water
WMT	Western Mediterranean Transient
MOW	Modified Outflow Water
ISFET	Ion Sensitive Field Effect Transistor
CL-ISE	Chlorine Ion Sensitive Electrode
REP14 - MED	Recognised Environmental Picture 2014 Mediterranean experiment
CMRE	Centre for Maritime Research and Experimentation
VINDTA	Versatile Instrument for the Determination of Titration Alkalinity
SOP	Standard Operating Procedure
CRM	Certified Reference Material
DCM	Deep Chlorophyll Maximum
MLD	Mixed Layer Depth
BOUSSOLE	Boueé pour l'acquisition de Séries Optiques à Long Terme
DyFAMed	Dynamique des Flux Atmospheriques en Mediterraneé
SEDOO	SErvice de DOnnées de l'OMP

Acknowledgements

For supporting me throughout the PhD process, offering enthusiasm, encouragement, and research and writing support, I thank my PhD supervisors Jan Kaiser, Karen Heywood, Jacqueline Boutin, and Dorothee Bakker. Their guidance, experience, patience, and interest in this work has helped to shape the thesis, and has helped guide me through the world of academia. I am honoured to have had the chance to obtain a PhD in a subject that I find fascinating, and I am grateful for the many life-changing research experiences that were possible because of their constant support. I thank Liliane Merlivat for her enthusiasm and guidance concerning work at the BOUSSOLE mooring. She is an inspiration.

For providing the funding for this work, I thank the Defence Science and Technology Laboratory and Direction générale de l'armement. I particularly thank Tim Clarke and Carole Nahum for their support and guidance.

Much of the work in this thesis depended on the hard work of the crew, officers, and scientists on board the *RVPlanet*, *NRVAlliance*, and *RV Thetys II*, and those on land at the University of East Anglia, Centre for Maritime Research and Experimentation, Observatoire Océanologique de Villefranche sur Mer, and the Tokyo University of Marine Science. I thank the Boussole and DyFAMed teams led by D. Antoine and L. Coppola, respectively, at Laboratoire d'Océanographie de Villefranche / Observatoire Océanologique de Villefranche-sur-Mer for welcoming the glider experiment, sharing data, and providing logistical assistance for this project. A special thanks to Gareth and Marcos for teaching me about glider and sensor technology, to Kiminori for supplying the experimental pH-$p(\mathrm{CO_2})$ sensors and helping with glider deployments, and to Bastien and Gillian for teaching me about glider piloting, the glider toolbox, and general data processing.

For taking the time to read my thesis top to bottom, I thank Andrew Manning, Stephanie Henson, and Pierre Testor. Their suggestions have helped me improve this thesis.

A PhD is not just about research and writing. There were many people that I met along the way that made my time at the University of East Anglia, and Université Pierre et Marie Curie a truly memorable experience. For interesting chats over couch lunches, for sporadic

bursts of humorous drama and anecdotes, for lessons in unfamiliar Brazilian expressions, and for the extracurricular activities, be it sportive or beverage-based, I thank Office 3.16 and neighbours: Denis, Marina, Stuart, Dan, Peter, Helen, Ryan, Phil, Elise, Chata, Umberto, Dave, Richard, Louise, Tahmeena, Luca, *et al.* Thanks goes to David, Marina, Adriano, and meu amor coco-cinho Guri for making my last few years living in Norwich truly amazing. I will always remember the fun of our conversational misunderstandings. Pour les innombrables pauses-café, pour lier sur nourriture terrible de la cantine, pour les nuits mémorables dans les caves à vin froides et sombres, et pour de m'accueillir à Paris, je remercie le couloirs du 5^{eme} étage: Vio, Chris, Sébastian, Antoine, Laura, Alex, Emilie, Sally, Aïda, Victor, et Zoé.

Above all, I would like to thank my family and friends in Wales, England, and around the world for their encouragement and support over the last four years. This PhD required a lot of my time, yet you all stuck by me. I thank my grandad Harry Eccles and my grandmother Vera Hemming, whose lives inspired me to do a PhD.

A final dedication to Barbi Bejer who sadly lost her life whilst pursuing her PhD. For those reading this and who are struggling with the pressures of PhD life it is important to seek professional help, or seek help in your personal environment, even if you think it's probably a temporary thing.

1

Observing the Mediterranean Sea

1.1 Understanding a Changing World

Throughout history, the oceans have been relied on as a food source, for transportation, trade, and growth. One tenth of the global population lives within coastal areas less than 10 m above sea level (McGranahan et al., 2007). Global average air temperature is predicted to increase by around 2 °C (relative to 1986 to 2005 average temperature) by the year 2050 if global anthropogenic emissions continue to rise (Collins et al., 2013). To date, roughly a quarter of global anthropogenic emissions have been absorbed by the ocean (Le Quéré et al., 2018). Global oceanic temperatures have risen on average by 0.11 °C per decade in the upper 75 m of the water column, and between 0.02 °C and 0.04 °C per decade between 75 m and 500 m between 1971 and 2010 (Rhein et al., 2013b). The Mediterranean Sea is considered a 'laboratory basin', where global-scale processes occur on smaller spatial and temporal scales than in other oceans (Álvarez et al., 2014). This makes it easier to study long term processes over shorter time periods. Sea surface temperature in the northwestern Mediterranean Sea has increased on average by 1.27 °C between 1982 and 2016 (Pastor et al., 2017), and is projected to rise by a further 0.5 °C to 2.6 °C by the end of the twenty-first century (Shaltout and Omstedt, 2014). The world's oceans are becoming increasingly acidic (i.e. ocean pH is decreasing) as a result of absorbing atmospheric CO_2 in the ocean (Doney et al., 2009). Decreasing ocean pH has the potential to affect calcifying organisms, such as marine algae and reef-building corals, due to changes in seawater carbonate chemistry (Doney et al., 2009). Surface pH in the northwestern Mediterranean Sea, and at the Strait of Gibraltar has decreased by $0.0022\,\mathrm{a}^{-1}$ and $0.0044\,\mathrm{a}^{-1}$, respectively (Merlivat et al., 2018; Flecha et al., 2015). The Mediterranean

Sea comprises of just 0.8 % of the global oceanic surface, but for its size is regarded as an important sink for anthropogenic carbon due to its physical and biogeochemical characteristics (Álvarez et al., 2014). Between 1995 and 2012, surface dissolved inorganic carbon concentrations increased and surface pH decreased twice as much, and surface temperature increased six times more in the northwestern Mediterranean Sea, than surface waters in the North Atlantic (Bates et al., 2012; Yao et al., 2016). Understanding the ocean system, its link with the atmosphere and biosphere, and understanding how it will change in the future is challenging.

Essential ocean variables, such as temperature, salinity, oxygen, and pH, are needed to investigate complex physical and biogeochemical processes. The majority of ocean measurements are collected by ship, autonomous platforms (e.g. Argo floats and underwater gliders), by sensors attached to drifting or moored buoys, and by remote-sensing satellites (Williams and Follows, 2011). Studies that project future climate change impacts rely on simulation models, which are validated using *insitu* observations (Flato et al., 2013). The extent to which we understand future climate change impacts, particularly on ocean temperature and ocean pH, is still limited. Increasing the number of observations in our oceans will help to reduce uncertainties in future climate change projections by allowing the evaluation of model simulations. Exploring new ocean observing technology, such as experimental sensors on underwater gliders, in a region impacted by climate change, will go some way in improving our knowledge.

1.2 Ocean pH

Normally unreactive in the atmosphere, CO_2 dissolved in seawater (CO_2(aq)) takes part in a number of chemical reactions. In particular, carbonic acid (H_2CO_3) forms as a result of (CO_2(aq)) reacting with water, which dissociates into bicarbonate (HCO_3^-) and carbonate (CO_3^{2-}) (Eq. 1.1-1.3). These seawater carbonate species are referred to as dissolved inorganic carbon concentrations (c(DIC), with 'c' representing a concentration), with HCO_3^- accounting for 90 % of c(DIC). During the dissociation of carbonate species, hydrogen ions (H^+) are released. pH is calculated as the negative logarithm of the activity (commonly referred to as a concentration) of these H^+ ions. Thus pH in the ocean is directly related to the activity of H^+ ions in the water (Zeebe and Wolf-Gladrow, 2001).

$$CO_{2(aq)} + H_2O \leftrightarrow H_2CO_3 \tag{1.1}$$

$$H_2CO_3 \leftrightarrow HCO_3^- + H^+ \tag{1.2}$$

$$HCO_3^- \leftrightarrow CO_3^{2-} + H^+ \tag{1.3}$$

Ocean pH today is often considered spatially homogenous across the World, as discussions are often made in the context of pH across geological time scales (e.g. Caldeira and Wickett (2003)). However, this view is not consistent with *insitu* pH observations (Joint et al., 2011). pH varies on timescales spanning less than a day (Hofmann et al., 2011) to many years (Rhein et al., 2013a). Measurements of pH with higher temporal resolution, such as those measured by *in situ* sensors, can vary greatly depending on their location and depth.

On daily to annual time scales, pH variability is affected by a variety of processes. This includes photosynthesis, respiration, temperature, and physics (Johnson et al., 2016). For example, an increase in photosynthesis due to a phytoplankton bloom would reduce CO_2, therefore altering the activity of H^+ ions increasing ocean pH (Joint et al., 2011). Hofmann et al. (2011) described the results of 15 deployments using SeaFET *insitu* pH sensors close to the surface at a number of locations worldwide. They found pH in open ocean areas, such as in the temperate eastern Pacific Ocean, to vary by as little as 0.02 over a period of 30 days. pH in the open ocean is stable and generally conforms to the results of global models. Variations in pH here are mostly driven by temperature. In other types of environments, such as near-shore / estuarine, upwelling, and Kelp forest environments, Hofmann et al. (2011) found pH variability was forced by biological activity, and physical processes, such as currents, mixing, freshwater input, and the tides. Diel cycles in pH exist, with the most consistent variations found in coral reef locations. pH cycles here were at a maximum early evening and at a minimum in the morning, and had amplitudes of between 0.1 and 0.25, similar in range to other studies based in subtropical estuaries (Yates et al., 2007). The pH diel cycles found at the coral reef locations correlated with fluctuations in oxygen and total alkalinity (Hofmann et al., 2011). Hofmann et al. (2011) found pH could vary by as much as 1.1 in extreme environments, such as those obtained close to volcanic CO_2 vents off the coast of Italy over a time period of 30 days. The pH variability found here was largely due to the CO_2 output from the volcanic vents mixing with the nearby waters.

Since before the industrial revolution (year 1760), global surface ocean pH has fallen from 8.21 to 8.10 (corresponding to a 30 % increase in H^+ ion activity) as a result of the atmospheric CO_2 mole fraction increasing by more than $100\,\mu\mathrm{mol\,mol^{-1}}$(Doney et al., 2009; Fabry et al., 2008). Future projections of anthropogenic carbon dioxide emissions suggest that ocean uptake of CO_2 will continue for many decades, thus contributing to long term ocean acidification (Rhein et al., 2013a).

Ocean acidification may have a significant effect on marine organisms. A range of studies testing the effect of modified seawater chemistry (e.g. low pH, modified $p(CO_2)$) on biological calcification, growth, and metabolism, have shown a range of effects on organisms, such as calcifying phytoplankton (e.g. coccolithophores) and corals (e.g.

scleractinian) (Doney et al., 2009; Hofmann et al., 2011). Such tests are undertaken in laboratory conditions, and do not necessarily consider the dynamics of pH on local scales in the environment. It is uncommon for natural variability in pH to be considered in studies of ocean acidification, and an increase of *insitu* pH data would provide context to laboratory experiments. It is possible that extreme events could take place when combining short-term pH variations with the long-term decrease of pH, leading to large impacts on marine organisms (Hofmann et al., 2011; Joint et al., 2011).

1.3 The High-Resolution Revolution: Underwater Gliders and Developing Sensors

A new technology aimed to transform the ocean observation system was presented to the ocean sciences community in the late 1980s by Stommel (1989). The potential to use underwater gliders as ocean sensor platforms to obtain high-resolution data was put forward. Three widely-used underwater glider models were developed: the Scripps Institution of Oceanography's and Woods Hole Oceanographic Institution's Spray glider (Sherman et al., 2001), Webb Research's Slocum glider (Webb et al., 2001; Schofield et al.), and the University of Washington's Seaglider (Eriksen et al., 2001).

Underwater gliders are buoyancy-driven vehicles that profile the water column in high-resolution using an array of sensors. Glider buoyancy is controlled by changing the glider's volume, increasing or decreasing its density relative to the surrounding water, causing the glider to move vertically. The wings attached to either side of the glider create lift, causing the glider to move horizontally. A glider can reach a maximum depth of 1000 m within a single dive that can last up to 6 hrs. Gliders move slowly in the water column, and are energy efficient, allowing deployments to last several months (Rudnick, 2016).

Underwater gliders have been deployed at various sites in the Mediterranean Sea. There have been multiple glider deployments at the Nice - Calvi line to investigate physical and biogeochemical variability in the region (Bosse et al., 2015; Niewiadomska et al., 2008). In 2004, a glider was deployed in the Ionian Sea (east of Sicily) with an objective of assessing the impact of assimilating glider data into an operational forecasting model (Dobricic et al., 2010). More recently, underwater gliders have been useful platforms to test new sensors, such as a dissolved organic matter optical sensor in 2015 and 2016 (Cyr et al., 2017).

Gliders are typically supplied with a non-pumped Sea-Bird Scientific SBE conductivity-temperature-depth (CTD) sensor. However, it is common for underwater gliders to include additional sensors that measure oxygen (e.g. Aanderaa optical sensors), chlorophyll *a* and coloured dissolved organic matter (CDOM) fluorescence, optical backscatter at different wavelengths (e.g. WET Labs Eco Puck), and turbulence (e.g. Ocean Microstructure Gliders

- OMGs).

Obtaining measurements of ocean pH that are both accurate (i.e. small differences between the measured and true values of the sample pH) and precise (i.e. good agreement between multiple measurements of the sample pH), in the laboratory and in the field, is challenging due to the scale in which pH varies in space and time. For example, observed pH trends range between -0.0014 and -0.0024 per year at the surface (Rhein et al., 2013b). pH-measuring methodologies must be capable of detecting small changes in pH with a great degree of reliability.

Before 1988, the potentiometric method was most commonly used for measuring pH, which uses hydrogen ion sensitive glass electrodes coupled with a reference electrode. This method has had issues with measurement uncertainties related to temperature and *in situ* conversion, glass & reference electrode drift, and ionic strength calibration (Dickson, 1993). This method has an accuracy of ± 0.02.

Since 1989, it has been possible to measure pH to an accuracy of 10^{-3} using a spectrophotometric approach (Byrne and Breland, 1989). This approach uses spectrophotometry to determine the light absorbance values using sulphonephthalein indicator dyes corresponding to pH. Although there have been some advances in adapting this approach to measure pH autonomously *in situ* (Martz et al., 2003; Seidel et al., 2008; Aßmann et al., 2011), spectrophotometry is largely used for shipboard measurements as it requires the use of indicator dye, and a means to measure spectrophotometric blanks, which is challenging outside of a laboratory (Martz et al., 2010).

From the early 1990s onwards, improvements were made to the technique of measuring pH in response to many of the concerns flagged by the ocean carbon community. Effort was made by global ocean observational programmes to systematically regulate and distribute Reference Materials (RMs) and to provide Standard Operating Procedures (SOPs) to maintain a recommended level of quality in obtained measurements (e.g.Dickson et al. (2007)). Furthermore, a number of hydrographic surveys and stations offering long-term time series of pH (e.g. Flecha et al. (2015)) were established, improving temporal and spatial resolution.

More recently, ion sensitive field effect transistor (ISFET) sensors have been used to measure pH. ISFET sensors work by determining the activity of H^+ ions using the interface potential between the semiconducting ion sensing transistor coated with silicon dioxide (SiO_2) and silicon nitride (Si_3N_4), and a reference electrode. Johnson et al. (2016) described their progress on a pressure tolerant ISFET pH sensor: the DuraFET. They claimed a sensor accuracy of ± 0.01, and a multiyear precision of ± 0.005. As of February 2016, 86 biogeochemical profiling floats with DuraFET ISFET pH sensors have been deployed across the globe as part of the Southern Ocean Carbon and Climate Observations and Modeling (SOCCOM) program. When comparing float data over a period of 6 months with an independent data source, pH measured by the DuraFET ISFET sensor was accurate to within 0.005 ± 0.007 (Johnson et al., 2017). Although the DuraFET performs well, the sensor is large, and therefore requires some modification for glider applications.

This thesis describes the trials of an experimental ISFET pH-p(CO$_2$) sensor attached to a glider. Carbon-based variables, such as pH, are crucial to understanding the fundamental changes taking place in our oceans resulting from the increased uptake of atmospheric carbon dioxide, and changing temperatures (Takahashi et al., 2009; Chavez et al., 2017). However, measuring pH at high-resolution on a glider with good accuracy is challenging. In 2013, the Wendy Schmidt Ocean Health \$2 million XPrize competition was launched to find a cheap, easy-to-use, efficient, and accurate ocean pH sensor (Okazaki et al., 2017). Although this competition was successful in finding a pH sensor that matched these criteria (Sunburst sensors (http://www.sunburstsensors.com/) took the main prize of \$1.5 million), there are currently no commercially available pH sensors with good accuracy, small enough to be attached to underwater gliders. The Sunburst pH sensors are longer than 28 cm and require external batteries. The DuraFET sensor developing team won \$250,000 during the XPrize competition. Their sensor has recently been modified for testing on a Slocum underwater glider (Saba et al., 2018). They found issues with the sensor's time lag response, and at times disagreement between the spectrophotometric reference samples and glider measurements.

1.4 The Mediterranean Sea

The Mediterranean Sea is almost completely land-locked, with its sole connection to the rest of the world's oceans being the Strait of Gibraltar in the west. It is positioned in the middle of the European continent to the north, the African continent to the south, and the Asian continent to the east (Fig. 1.1). Evaporation is more prominent than precipitation and river runoff here. If the Strait of Gibraltar were to close in future, the Mediterranean Sea would decrease by up to $1\,\mathrm{m\,a^{-1}}$ (Millot and Taupier-Letage, 2005). It is this net evaporation that causes a difference in sea level height between the Mediterranean Sea and the Atlantic Ocean, leading to eastward surface Atlantic water flow into the Mediterranean Sea at the Strait of Gibraltar. This incoming water is continuously modified within the Mediterranean Sea, and is known as Modified Atlantic Water (MAW, Fig. 1.2). MAW continues to flow eastward along the northern coast of Africa, into the eastern Mediterranean basin, following the continental shelf edges off Turkey, Greece, and Italy, northward and eventually westward, back towards the Strait of Gibraltar along the southern coasts of France and Spain (Millot and Taupier-Letage, 2005). In the eastern basin of the Mediterranean Sea between Cyprus and Rhodes, Greece, MAW becomes saltier and more dense, producing Levantine Intermediate Water (LIW) at depths of between 100 m and 500 m (Fig. 1.2). LIW flows in a counter-clockwise fashion along the continental shelf margins surrounding the Mediteranean Sea, similarly to MAW (Millot, 1999). Western and Eastern Mediterranean Deep Water (WMDW and EMDW, respectively) can be found at depths greater than 500 m (Fig. 1.2). WMDW is formed in the northwestern corner of the western Mediterranean Sea during winter when deep convection mixes MAW and LIW (Knoll et al., 2017). EMDW is formed during winter mixing in the relatively shallow Aegean and Adriatic seas, situated east of Italy, and between Greece and Turkey, respectively (Millot and Taupier-Letage, 2005).

In 2005, the intermediate and deep water masses in the Western Mediterranean Sea started to change. Temperature and salinity has increased twice as much at these depths since 2005, than between 1961 and 2004 (Borghini et al., 2014; Schroeder et al., 2016). This recent change in temperature and salinity is known as the Western Mediterranean Transition (WMT) (Zunino et al., 2012). The WMT is caused by intermittent deep water formation events that produce warmer and saltier waters, and a steady salt flux downward from typical LIW depths to depths corresponding to WMDW. The WMT water mass is well-mixed, and continues to thicken as a result of processes accumulating salt and heat (Schroeder et al., 2016). Mediterranean Sea salinity at depths greater than 1000 m increased the most globally between 1950 and 2010 (Skliris et al., 2014). Recent studies have demonstrated the importance of Mediterranean Outflow Water (MOW) through the strait of Gibraltar on ocean circulation and global climate. MOW intermittently penetrates into the North Atlantic subpolar gyre, linked to variability of the North Atlantic Oscillation (NAO), affecting the global transport of heat, salt, and other properties (Lozier and Stewart, 2008; Curry et al., 2003).

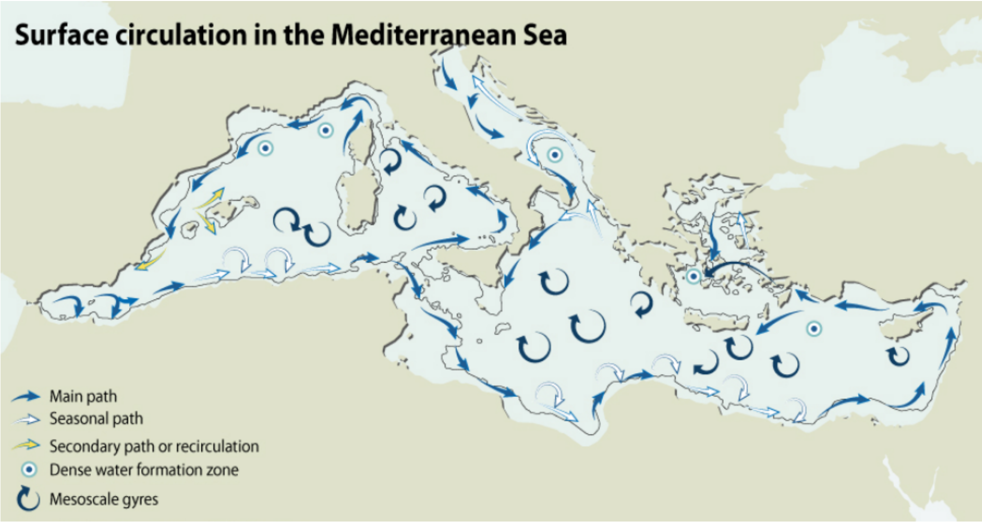

Figure 1.1: Surface circulation in the Mediterranean Sea. This plot was produced by GRID-Arendal, adapted from Millot and Taupier-Letage (2005)

The Mediterranean Sea is classed as one of the most oligotrophic seas in the world (Azov,

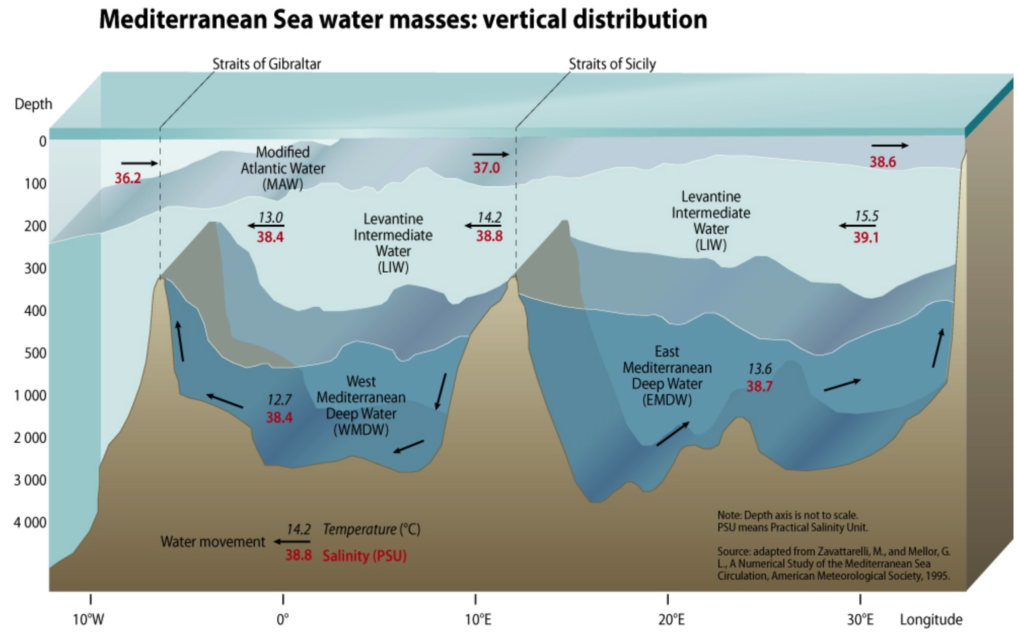

Note: Depth axis is not to scale.
PSU means Practical Salinity Unit.

Source: adapted from Zavattarelli, M., and Mellor, G. L., A Numerical Study of the Mediterranean Sea Circulation, American Meteorological Society, 1995.

Figure 1.2: Water masses in the Mediterranean Sea. Diagram produced by GRID-Arendal, adapted from Zavatarielli and Mellor (1995)

1991), although Spring blooms are common at some locations (e.g. the BOUSSOLE / DyFAMed sites, Merlivat et al. (2018)), and a deep chlorophyll maximum is often present during the summer (Estrada, 1996). The Mediterranean Sea is a sink for 1.1 % of global anthropogenic carbon dioxide emissions (Schneider et al., 2010). As the Mediterranean Sea represents just 0.8 % of the total area of oceans globally, and 0.3 % of total global water volume, the region can be classed as an important sink for its size (Schneider et al., 2010; Álvarez et al., 2014). The Mediterranean Sea has a low Revelle factor, due to relatively warm, salty, and high alkalinity waters (Álvarez et al., 2014). This encourages a net flux of carbon dioxide from the atmosphere to the ocean. pH on the total scale normalised to 25 °C in the Mediterranean Sea typically varies between 7.98 and 8.02 at the surface, and between 7.88 and 7.96 at greater depths (Álvarez et al., 2014).

The northwestern Mediterranean Sea displays strong seasonal variability. At the surface, temperatures remain at around 13 °C to 14 °C during the winter, increasing from spring to maxima of 26 °C to 28 °C during the summer. Wind-driven vertical mixing in the top 300 m is dominant during winter and autumn, whilst surface stratification is common during the summer as a result of solar heating (Copin-Montégut et al., 2004). At times when vertical mixing is the dominant process, nutrients can be transported from greater depths to otherwise nutrient-lacking surface waters (Marty and Chiavérini, 2002; de Fommervault et al., 2015). A combination of nutrient availability and increased stability driven by an increase in temperature by a few tenths of a degree Celsius can be enough for phytoplankton blooms to occur (Yao et al., 2016; Copin-Montégut et al., 2004).

The Mediterranean Sea is one of the largest nutrient-lacking oceans in the World (Ignatiades, 2005). However, an anomalously high Nitrogen to Phosphorus ratio is found in the Mediterranean Sea (Pujo-Pay et al., 2011). There is an oligotrophic gradient between the western and eastern basins. The western basin is ranked 'oligotrophic', whilst the eastern basin is ranked 'ultra-oligotrophic' (Siokou-Frangou et al., 2010). This oligotrophic gradient could be attributed to spatial variations in allochtonous nutrient quantities and quality, and the differences in hydrography between the two basins (Pujo-Pay et al., 2011; Álvarez et al., 2014). Primary productivity in the Mediterranean Sea is linked to wind-driven mixing, mesoscale currents and eddies, riverine input, and depositions (e.g. from the Sahara (Ridame and Guieu, 2002)) (Pujo-Pay et al., 2011). A phytoplankton bloom occurs in spring when the mixed layer is shallow (Mayot et al., 2017). This region is one of the most productive in the Mediterranean Sea, with an estimated annual primary production of between 86 and 232 $\mathrm{g\,m^{-2}\,a^{-1}}$ (using *insitu* measurements, Marty and Chiavérini (2002)), compared to estimates of between 20.3 and 99 $\mathrm{g\,m^{-2}\,a^{-1}}$ in the eastern Mediterranean Sea (using *insitu* measurements, Siokou-Frangou et al. (2010)).

1.5 Thesis Outline

This thesis comprises of four broad themes:

- The implementation of an experimental Ion Sensitive Field Effect Transistor (ISFET) pH-pCO$_2$ sensor on an underwater glider. This includes an assessment of the sensor's performance, and a description of its calibration.
- The characterisation of physical and biogeochemical parameters in the northwestern Mediterranean Sea using data collected by underwater glider, ship, and moored buoys.
- The calculation of net community production using concentrations of dissolved oxygen, and concentrations of dissolved inorganic carbon.
- The calculation of horizontal spatial scales of variability using statistical semivariograms and glider physical and biogeochemical measurements at two locations in the northwestern Mediterranean Sea.

In Chapter 2, the first trial of the experimental ISFET pH-pCO$_2$ sensor in the Sardinian Sea is presented, along with a description of its accuracy, validation, and required calibration. The corrected glider ISFET pH measurements are discussed and compared with other biogeochemical and physical parameters. In Chapter 3, the second trial of the

ISFET pH-$p\mathrm{CO}_2$ sensor at the BOUSSOLE site is presented. Net community production is estimated using measurements of dissolved oxygen concentrations and dissolved inorganic carbon concentrations. The spring bloom is identified using measured variables. In Chapter 4, spatial scales of variability in the northwestern Mediterranean Sea are estimated using glider biogeochemical and physical parameters. Horizontal spatial scales of variability are determined between the surface and 300 m depth using semivariograms. Chapter 5 concludes the findings presented in this thesis.

2

Measuring pH Variability Using an Experimental Sensor Attached to an Underwater Glider

Publication

This chapter has been previously published in *Ocean Science* under the title 'Measuring pH Variability Using an Experimental Sensor Attached to an Underwater Glider', with co-authors Jan Kaiser, Karen J. Heywood, Dorothee C.E. Bakker, Jacqueline Boutin, Kiminori Shitashima, Gareth Lee, Oliver Legge, and Reiner Onken. All scientific work and writing was undertaken by Michael Hemming, with improvements made using comments from co-authors. This chapter is as published.

Hemming, M. P., Kaiser, J., Heywood, K. J., Bakker, D. C. E., Boutin, J., Shitashima, K., Lee, G., Legge, O., and Onken, R.: Measuring pH variability using an experimental sensor on an underwater glider, Ocean Sci., 13, 427-442, https://doi.org/10.5194/os-13-427-2017, 2017.

2.1 Summary

Autonomous underwater gliders offer the capability of measuring oceanic parameters continuously at high resolution in both vertical and horizontal planes, with timescales that can extend to many months. An experimental ion sensitive field effect transistor (ISFET) sensor measuring pH on the total scale was attached to a glider during the REP14 - MED experiment in June 2014 in the Sardinian Sea, northwestern Mediterranean. During the deployment, pH was sampled at depths of up to 1000 m, along an 80 km transect over a period of 12 days. Water samples were collected from a nearby ship and analysed for dissolved inorganic carbon concentration and total alkalinity to derive pH for validating the ISFET sensor measurements. The vertical resolution of the pH sensor was good (1 to 2 m), but stability was poor, and the sensor drifted in a non-monotonous fashion. In order to remove the sensor drift, a depth-constant time-varying offset was applied throughout the water column for each dive, reducing the spread of the data by approximately two thirds. Furthermore, the ISFET sensor required temperature and pressure-based corrections, which were achieved using linear regression. Correcting for this decreased the apparent sensor pH variability by a further 13 to 31 %. Sunlight caused an apparent sensor pH decrease of up to 0.1 in surface waters around local noon, highlighting the importance of shielding the sensor away from light in future deployments. The corrected pH from the ISFET sensor is presented along with potential temperature, salinity, potential density anomalies (σ_θ), and dissolved oxygen concentrations ($c(O_2)$) measured by the glider, providing insights into physical and biogeochemical variability in the Sardinian Sea. pH maxima were identified close to the depth of the summer chlorophyll maximum, where high $c(O_2)$ were also found. Longitudinal pH variations at depth ($\sigma_\theta > 28.8\,\mathrm{kg\,m^{-3}}$) highlighted variability of water masses in the Sardinian Sea. Higher pH was observed where salinity was > 38.65, and lower pH was found where salinity ranged between 38.3 and 38.65. The higher pH was associated with saltier Levantine Intermediate Water, and it is possible the lower pH was related to the remineralisation of organic matter. Furthermore, shoaling isopycnals closer to shore coinciding with low pH and $c(O_2)$, high salinity, alkalinity, dissolved inorganic carbon concentrations and chlorophyll fluorescence waters may be indicative of upwelling.

2.2 Introduction

It is estimated that a third of anthropogenic CO_2 emitted between 2004 to 2013 was absorbed by the oceans (Le Quéré et al., 2015). Normally unreactive in the atmosphere, CO_2 dissolved in seawater (CO_2(aq)) takes part in a number of chemical reactions. In particular, carbonic acid (H_2CO_3) forms as a result of (CO_2(aq)) reacting with water, which dissociates into bicarbonate (HCO_3^-) and carbonate (CO_3^{2-}) ions. These seawater carbonate species are referred to as dissolved inorganic carbon concentrations (c(DIC), with 'c' representing a concentration), with HCO_3^- accounting for 90 % of c(DIC). During the dissociation of carbonate species, hydrogen ions (H^+) are released. pH is calculated as the negative decadic logarithm of the activity (commonly referred to as a concentration) of these H^+ ions. Thus pH in the ocean is directly related to the activity of H^+ ions in the water (Zeebe and Wolf-Gladrow, 2001).

pH varies on timescales spanning less than a day (Hofmann et al., 2011) to many years (Rhein et al., 2013a). Since before the industrial revolution (year 1760), global surface ocean pH has fallen from 8.21 to 8.10 (corresponding to a 30 % increase in H^+ ion activity) as a result of the atmospheric CO_2 mole fraction increasing by more than $100\,\mu mol\,mol^{-1}$(Doney et al., 2009; Fabry et al., 2008). Future projections of anthropogenic CO_2 emissions suggest that ocean uptake of CO_2 will continue for many decades, thus contributing to long term ocean acidification (Rhein et al., 2013a). This may have a significant effect on marine organisms, such as calcifying phytoplankton (e.g. coccolithophores) and corals (e.g. scleractinian), dependent on the solubility state of calcium carbonate (Doney et al., 2009).

Since 1989, it has been possible to measure pH to an accuracy of $\pm 10^{-3}$ using a spectrophotometric approach (Byrne and Breland, 1989). Although there have been some advances in adapting this approach to measure pH autonomously *in situ* (Martz et al., 2003; Aßmann et al., 2011), spectrophotometry is largely used for shipboard measurements as it requires the use of indicator dye, and a means to measure spectrophotometric blanks, which is challenging outside of a laboratory (Martz et al., 2010).

A limited number of hydrographic surveys have been undertaken, and stations offering long term time series of pH are available (Rhein et al., 2013a), but there is a drive to improve spatial and temporal data coverage via autonomous means, similar to what was experienced for temperature and salinity with Argo floats 16 years ago (Roemmich et al., 2003). There is demand to develop a reliable autonomous sensor with precision and accuracy of 10^{-3}, whilst being affordable to the scientific community (Johnson et al., 2016).

The Mediterranean Sea comprises just 0.8 % of the global oceanic surface, but is regarded as an important sink for anthropogenic CO_2 due to its physical and biogeochemical characteristics (Álvarez et al., 2014). Between 1995 and 2012, surface c(DIC) increased by 3 $\mu mol\,kg^{-1}\,a^{-1}$ in the northwest Mediterranean Sea, consistent with a rise in temperature of $0.06\,°C\,a^{-1}$, and a decrease in pH of $0.003\,a^{-1}$ (Yao et al., 2016). In contrast, pH in the neighbouring North Atlantic Ocean decreased by just $0.0017\,a^{-1}$ associated with an increase in c(DIC) of around 1.4 $\mu mol\,kg^{-1}\,a^{-1}$, and a temperature rise of $0.01\,°C\,a^{-1}$ (Bates et al., 2012). The greater potential of the Mediterranean Sea to store anthropogenic carbon can be explained by its higher alkalinity, warmer temperatures, and thus lower Revelle factor (Álvarez et al., 2014; Touratier and Goyet, 2011), when compared with other oceans, such as the North Atlantic.

pH in the Mediterranean Sea is typically higher than most other oceanic regions (Álvarez et al., 2014). pH on the total scale normalised to 25°C ($pH_{T,25}$) collected by ship between 1998 and 1999 within the northwestern Mediterranean Sea varied between 7.92 and 8.04 at the surface, and between 7.9 and 7.93 at depths greater than 100 m (Copin-Montégut and

Bégovic, 2002). When considering the Mediterranean Sea as a whole, $pH_{T,25}$ obtained by ship in April 2011 varied between 7.98 and 8.02 at the surface, and between 7.88 and 7.96 at greater depths (Álvarez et al., 2014). The peak-to-peak amplitude of the pH annual cycle in the northwest Mediterranean Sea is typically 0.1, with maxima and minima found in spring and summer, respectively (Yao et al., 2016).

Measurements of pH with higher temporal resolution, such as those measured by *in situ* sensors, can vary greatly depending on their location and depth. Hofmann et al. (2011) presented results of 15 deployments using SeaFET pH sensors close to the surface at a number of locations worldwide. They found pH could vary by as much as 1.1 in extreme environments, such as those obtained close to volcanic CO_2 vents off the coast of Italy, but as little as 0.02 in open ocean areas, such as in the temperate eastern Pacific Ocean, over a time period of 30 days. Hofmann et al. (2011) were able to capture diel cycles in pH, with the most consistent variations found in coral reef locations. pH was at a maximum early evening and at a minimum in the morning, and had amplitudes of between 0.1 and 0.25, similar in range to other studies based in subtropical estuaries (Yates et al., 2007). pH diel cycles found at coral reef locations correlate with fluctuations in oxygen and total alkalinity (Hofmann et al., 2011).

Autonomous underwater gliders offer the possibility to observe the oceanic system with a greater level of detail on both temporal and spatial scales when compared with ship measurements (Eriksen et al., 2001). A low consumption of battery power and a great degree of manoeuvrability enable such vehicles to cover large areas and profile depths of up to 1000 m during missions that can last from weeks to months at a time. They are suitable platforms for a range of sensors, measuring both physical and biogeochemical parameters (Piterbarg et al., 2014; Queste et al., 2012).

The main goal of this chapter is to describe the trial of a novel ion sensitive field effect transistor (ISFET) pH sensor which was attached to an autonomous underwater glider in the northwest Mediterranean Sea during the REP14 - MED sea experiment. The secondary objective is to provide a method of correcting pH measured by this sensor, and to discuss the spatial and temporal variability observed. The experiment, the glider sensors, including the ISFET sensor, and the method of validation, are described in Sect. 2.3. The ship based data are presented in Sect. 2.4.1, and a comparison between ship and glider measurements is made in Sect. 2.4.2. The initial pH results and validation, the method of further correcting pH, and an artifactual light-induced effect are also described in Sect. 2.4.2. Corrected pH measurements are analysed alongside other collected parameters later in Sect. 2.4.2, and the chapter's conclusions are provided in Sect. 2.5.

2.3 Methodology

2.3.1 REP14 - MED Sea Trial

This trial took place between 6th and 25th June 2014 in the northwest Mediterranean Sea off the coast of Sardinia, Italy (Fig. 2.1). This was part of the Environmental Knowledge and Operational Effectiveness (EKOE) research program led by the North Atlantic Treaty Organisation (NATO) Centre for Maritime Research and Experimentation (CMRE), based in La Spezia, Italy. This was the 5th Recognised Environmental Picture (REP) trial, which was jointly conducted by two research vessels; the NRV *Alliance* and the RV *Planet*.

Eleven gliders with varying pressure tolerances were deployed during the trial, each making repeated west-east transects separated roughly 0.13° latitudinally from one another within the REP14 - MED observational domain. One of these gliders was operated by the University of East Anglia (UEA); an iRobot Seaglider model 1KA (SN 537) with an ogive fairing. All gliders were deployed to meet the objectives of the trial, such as to improve ocean forecasting techniques (e.g. model validation, evaluation of forecasting skill), to conduct a cost/benefit analysis of autonomous gliders, to analyse mesoscale and sub-mesoscale features, and to test new glider payloads. The latter objective was perhaps most relevant to the deployment of the UEA glider. A more in-depth overview of the REP14 - MED trial, its objectives, and the collected observational data, is described by Onken et al. (2018).

The UEA glider completed a total of 126 dives between 11th and 23rd June 2014. The first

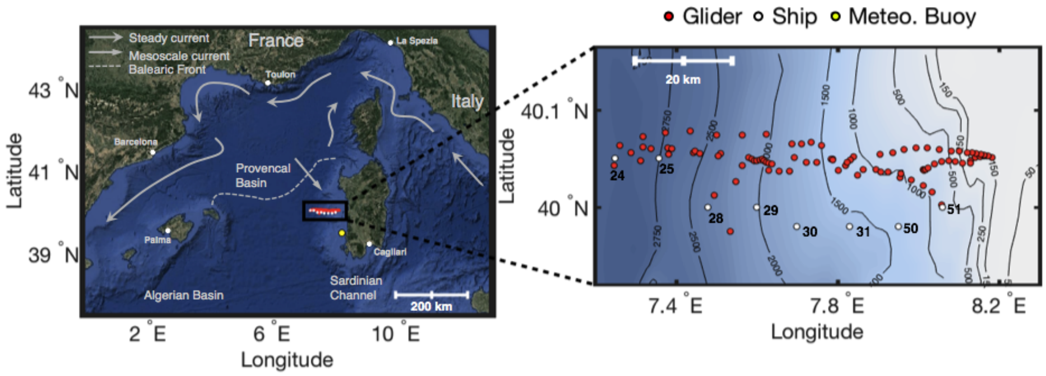

Figure 2.1: The locations of the 93 dives undertaken by the Seaglider (red markers), the 8 numbered ship CTD casts in which water samples were obtained (white markers), and Meteorological buoy M1 (yellow marker) within the REP14 - MED observational domain off the coast of Sardinia, Italy between 11th and 23rd June 2014. GEBCO 1 minute resolution bathymetry data (metres) were used (http://www.bodc.ac.uk/projects/international/gebco/), and surface circulation patterns were adapted from figures presented by Millot (1999).

24 dives did not record pH and the last 9 dives were very shallow, leaving 93 usable dives. Successive dives were approximately 2 to 4 km apart, descending to depths of up to 1000 m.

2.3.2 Glider Sensors

Conductivity, pressure and *in situ* temperature measurements were obtained by the glider using a Seabird Scientific glider payload CTD sensor (Fig. 2.2). These measurements were then used to obtain potential temperature (θ) and practical salinity.

Dissolved oxygen concentrations ($c(O_2)$, where 'c' refers to a concentration) were measured using an Aanderaa 4330 oxygen optode sensor positioned towards the rear of the glider fairing (Fig. 2.2). The method of calibrating $c(O_2)$ closely followed that described by Binetti (2016), using the oxygen sensor-related engineering parameters TCPhase and CalPhase, which will be summarised here. The first step involved correcting $c(O_2)$ to account for the response time (τ) of the sensor, as the diffusion of O_2 across the silicon foil of the sensor is not an instantaneous process. Each oxygen sensor has a different τ, which depends on the structure, thickness, age, and usage of the foil (McNeil and D'Asaro, 2014), and external environmental conditions such as temperature. An average τ of 17 seconds was obtained using the method outlined by Binetti (2016). After correcting TCPhase for τ, glider TCPhase profiles were matched in time and space with pseudo-CalPhase profiles back-calculated from measurements of $c(O_2)$ obtained by the ship Seabird Scientific SBE 43 sensor (CTD package) using the manufacturer's set of optode calibration equations. The relationship between the glider TCPhase and the ship pseudo CalPhase was established, and the calculated slope and offset coefficients were used to correct glider CalPhase, required for calibrating $c(O_2)$ measurements. A comparison between the ship $c(O_2)$ measurements and calibrated glider $c(O_2)$ measurements is made in Sect. 2.4.2.

Glider variables have been processed using an open-source MATLAB based toolbox (https://bitbucket.org/bastienqueste/uea-seaglider-toolbox/) in order to correct for differing timestamp allocations, sensor lags (Garau et al., 2011; Bittig et al., 2014), and to tune the hydrodynamical flight model (Frajka-Williams et al., 2011). Outliers outside of a specified range (e.g. 6 standard deviations) were flagged and not used for analysis, and glider profiles were smoothed using a Lowess low-pass filter with a span of 5 data points (<4 m range), which implements a local regression using weighted linear least squares and a 1st order polynomial linear model. Individual profiles were inspected afterwards to ensure that potentially correct data points were not removed.

The ISFET pH sensor used in this study (Fig. 2.2) was custom-built by a working group led by Kiminori Shitashima at the Tokyo University of Marine Science and Technology (previously the University of Kyushu), and is not commercially available. The ISFET unit

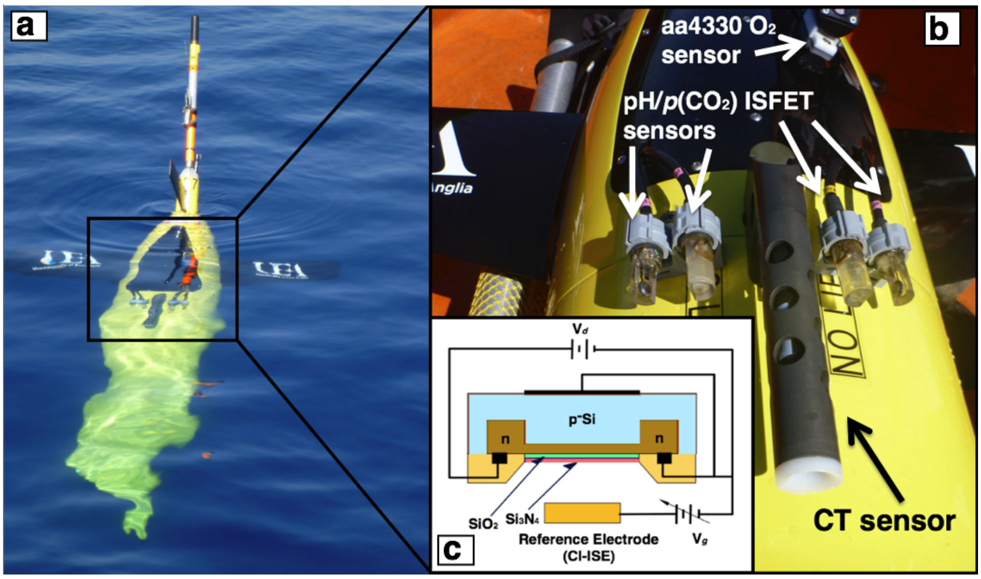

Figure 2.2: (**a**) Seaglider SN 537 during the deployment, (**b**) a close up of the sensors, and (**c**) a schematic diagram of the ISFET sensor adapted from Shitashima (2010).

was housed in acrylic resin material. The ISFET unit and the reference chlorine ion selective electrode (Cl-ISE) were moulded with epoxy resin in the custom-built housing. The ISFET pH unit was stand-alone, meaning that the sensor was not integrated into any of the onboard glider electronics. The power source of the sensor was 10.5 V, supplied by three 3.5 V Li-ion batteries.

The glider also carried another ISFET pH sensor that was integrated into the glider electronics (Fig. 2.2), as well as two $p(\mathrm{CO_2})$ sensors (Shitashima, 2010), one stand-alone and one integrated. The data retrieved from the integrated pH sensor, and the $p(\mathrm{CO_2})$ sensors could not be used due to quality issues. We think the regular on/off cycling of power to the integrated dual pH-$p(\mathrm{CO_2})$ sensor between sampling did not allow it to function properly. In future, we would suggest the addition of backup batteries to supply power to the sensor between sampling. The cause of the problem with the stand-alone $p(\mathrm{CO_2})$ unit is unclear.

To measure pH, the activity of $\mathrm{H^+}$ ions is determined using the interface potential between the semiconducting ion sensing transistor coated with silicon dioxide ($\mathrm{SiO_2}$) and silicon nitride ($\mathrm{Si_3N_4}$), and the Cl-ISE. The ISFET pH sensor was previously found to have a response time of a few seconds with an accuracy of ± 0.005 pH, with suitable temperature and pressure sensitivities (Shitashima et al., 2002; Shitashima, 2010; Shitashima et al., 2013). Before deploying the sensor, the ISFET and Cl-ISE were conditioned (as recommended by Bresnahan et al. (2014) and Takeshita et al. (2014)) in a bucket of local sea surface water with a salinity of 38.05. However, due to time constraints, conditioning took place over just one hour, rather than weeks as specified by Bresnahan et al. (2014) and Takeshita et al. (2014). During the deployment, pH measurements were obtained every

1 to 2 m vertically.

Measurements obtained by the ISFET pH sensor were converted from raw output counts to pH on a total scale using a two-point calibration with 2-aminopyridine (AMP) and 2-amino-2-hydroxymethil-1, 3-propanediol (TRIS) buffer solutions before and after the deployment of the glider. The same buffer solutions (Wako Pure Chemical Industries Ltd.) created in synthetic seawater (S = 35, ionic strength of around 0.7 M) were used before and after deployment. These buffer solutions had a pH of 6.79 ± 0.03 (AMP) and 8.09 ± 0.03 (TRIS). The pH uncertainty of the buffer solutions takes into account the effect of changing air temperature, ranging between 30.5 and 33.3 °C during pre-calibration, and between 27.5 and 28 °C during post-calibration. A linear fit using the raw output measured from these buffer solutions was used to convert the raw counts to pH (Shitashima et al., 2002). A drift was observed between the pH of these buffer solutions before and after the deployment, which was corrected for. As the ISFET sensor was previously described to have pressure-resistant performance and good temperature characteristics for oceanographic use (Shitashima et al., 2002; Shitashima, 2010), no compensations for temperature and pressure were performed on ISFET measurements at this stage. The ISFET pH sensor has a salinity sensitivity $\partial \mathrm{pH} / \partial \mathrm{S} = 0.011$ which was taken into account. The effect of biofouling on ISFET pH measurements, as well as on all other glider measurements, was ruled out after a post deployment inspection of sensors indicated no problems.

2.3.3 Ship Based Measurements

As the *in situ* ISFET pH sensor was under trial, some form of validation of the results was required. In total, 124 water samples were collected from Niskin bottles sampled at 12 depths (down to 1000 m) using a CTD rosette platform at eight locations (eight casts, numbered 24 - 51) close to the path of the glider (Fig. 2.1). Water samples were collected between 05:19 Local Time (LT, UTC+2) on the 9th June and 16:58 LT on the 11th June. The glider ISFET pH sensor started operating at 16:36 LT on 11th June. Overall, measurements obtained by the glider and the CTD overlapped better in space than in time (Fig. 2.3).

When collecting carbon samples, water was drawn into 250 mL borosilicate glass bottles from Niskin bottles on the CTD rosette using tygon tubing. Bottles were rinsed twice before filling and were overflowed for 20 seconds, allowing the bottle volume to be flushed twice. Each sample was poisoned with 50 µL of saturated mercuric chloride and then sealed using greased stoppers, secured with elastic bands and stored in the dark (Dickson et al., 2007). The total alkalinity (A_T) and the c(DIC) of each water sample was measured in the laboratory using a Marianda Versatile INstrument for the Determination of Titration Alkalinity (VINDTA 3C, www.marianda.com). c(DIC) was measured by coulometry (Johnson et al., 1985) following standard operating procedure SOP 2, and A_T was

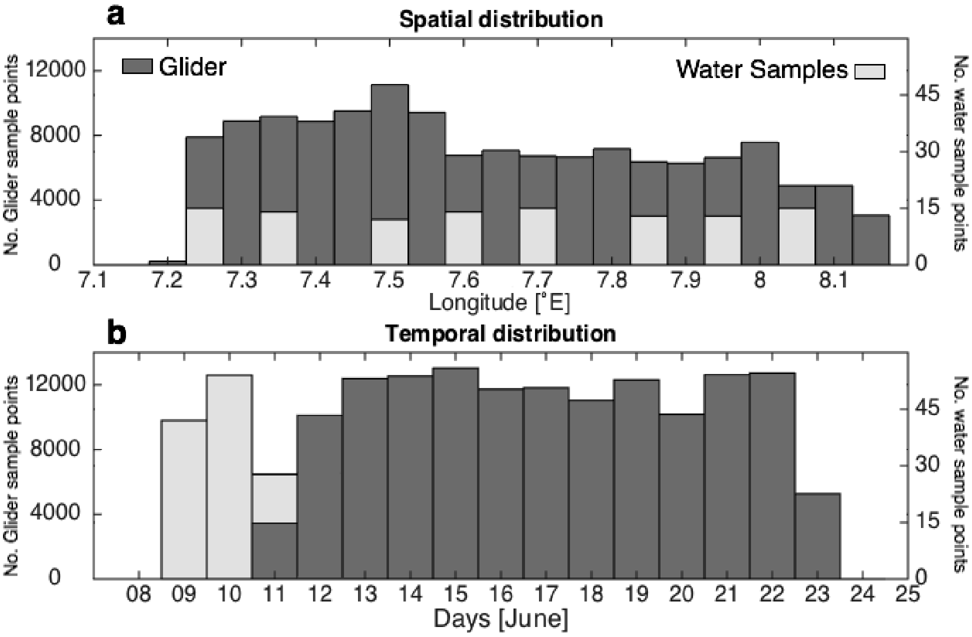

Figure 2.3: Histograms showing the (**a**) spatial and (**b**) temporal distribution of samples collected by the glider (dark grey) and by CTD water bottle sampling (light grey). The y-axis on the left is for the sum of glider samples, whilst the y-axis on the right is for the sum of water samples.

measured by potentiometric titration (Mintrop et al., 2000) following SOP 3b, both described by Dickson et al. (2007). During the analytical process, 21 bottles of certified reference material (CRM, batch 107) supplied by the Scripps Institution of Oceanography, USA were run through the instrument to keep a track of stability and to calibrate the instrument. For each day in the lab, 1 CRM was used before and after the samples were processed. A total of 19 concurrent replicate depth water samples were collected, with around 2 to 3 replicates per CTD cast. Calculating the mean standard deviation of these replicate samples enabled a measure of the instrument precision. The mean standard deviation of the c(DIC) and A_T replicates was $1.7\,\mu\mathrm{mol\,kg^{-1}}$ and $1.4\,\mu\mathrm{mol\,kg^{-1}}$, respectively. This corresponds to a pH uncertainty of ± 0.003 for c(DIC) and $\mathrm{A_T}$, respectively, resulting in a combined uncertainty of ± 0.009.

Once A_T and c(DIC) were known, pH could be derived using the CO2SYS program (Van Heuven et al., 2011). This calculation has an estimated pH probable error of around ± 0.006 due to uncertainty in the dissociation constants pK_1 and pK_2 (Millero, 1995). Temperature and salinity were obtained from the Seabird CTD sensor on the ship rosette sampler, and the seawater equilibrium constants presented by Mehrbach et al. (1973) were used as refitted by Dickson and Millero (1987), which has been recommended by previous studies (e.g. CARINA Data Synthesis Project) for the Mediterranean Sea (Álvarez et al., 2014; Key et al., 2010). The sulphate constant described by Dickson (1990), and the parameterisation of total borate presented by Uppström (1974), was used. More information on the equilibrium constants used in CO2SYS and other available carbonate system packages is described by Orr et al. (2015). pH derived from water samples collected by ship and glider retrieved ISFET pH are both on the total pH scale (as described by Dickson (1984)) at *in situ* temperature, and will from now on be referred to as $\mathrm{pH_s}$ and $\mathrm{pH_g}$, respectively.

Standard deviation ranges will, from this point on, be listed in this chapter when referring to variability in measurements, such as $\mathrm{pH_s}$ and $\mathrm{pH_g}$. To obtain these standard deviation ranges, data points for a given variable were sorted into 10 m depth bins down to a maximum depth of 1000 m. The standard deviation was then calculated for each bin.

2.4 Results and Discussion

2.4.1 Ship Based Data

Measurements obtained by the ship CTD package provide an overview of the temporal and spatial variability at the time when water samples used to derive $\mathrm{pH_s}$ were collected (Fig. 2.4). The potential temperature (θ) gradient was strong in the top 100 m of the water column due to limited vertical mixing, with a maximum of between 19 and 23 °C found in the upper 10 m of the water column, decreasing to between 13 and 14 °C at depths greater than 100 m. The salinity was low in the top 100 m, increasing to a maximum at around 400 to 600 m. These fresher waters in the top 100 m are likely modified Atlantic water (MAW), typically having a salinity of between 38 and 38.3 in the northwest Mediterranean Sea (Millot, 1999). These waters enter from the Atlantic Ocean through the Strait of Gibraltar, flowing along the North African coast. Some water makes its way northwards and follows the shelf back west towards the Atlantic Ocean (Rivaro et al., 2010; Millot, 1999). At deeper depths, warmer saltier waters were found east of 7.5° E, which is likely to be Levantine Intermediate Water (LIW), identified in the western Mediterranean Sea by a salinity range of 38.45 and 38.65, and θ of between 13.07 and 13.88 °C (Rivaro et al., 2010), typically found at depths of between 200 and 800 m close to the shelf slope (Millot, 1999). $c(\mathrm{O_2})$ maxima were found at depths of between 20 and 90 m. The Mediterranean Sea on the whole is considered to be oligotrophic (Álvarez et al., 2014). However, a Deep Chlorophyll Maximum (DCM) is common at these depths when waters are thermally stratified (Estrada, 1996). There is a build-up of actively growing biomass with greater cell pigment content as a result of photoacclimation, due to increased concentrations of nitrate, phosphate, and silicate, as well as sufficient levels of light at these depths (Estrada, 1996). It is likely this high $c(\mathrm{O_2})$ was related to the DCM, further evidenced by the high chlorophyll fluorescence layer observed at 60 to 100 m depth, particularly in the east.

The objective of deriving pH_s using A_T and c(DIC) was to make a comparison with pH_g measured by the ISFET sensor. c(DIC) and A_T were greatest at depths below 250 m, with lower values seen closer to the surface (Fig. 2.5a-b), which is typical of the northwest Mediterranean Sea (Copin-Montégut and Bégovic, 2002; Álvarez et al., 2014). The higher values of A_T and c(DIC) at depth and in the east support the notion that this is LIW, as this water mass has previously been identified as having an A_T of around 2590 µmol kg^{-1} and c(DIC) of roughly 2330 µmol kg^{-1} (Álvarez et al., 2014), coinciding with the warmer, saltier waters. Mean c(DIC) and A_T (averages over eight casts) have standard deviations of 6.1 to 11.9 µmol kg^{-1} and 5.9 to 10.6 µmol kg^{-1}, respectively, for the top 150 m of the water column, and 1.7 to 3.9 µmol kg^{-1} and 3.7 to 7.6 µmol kg^{-1} for deeper waters, respectively. pH_s had a maximum of 8.14 between 50 and 70 m depth (Fig. 2.5c). Mean pH_s have standard deviations of 0.004 to 0.011 within the top 150 m and 0.006 to 0.017 deeper than this. A proportion of these standard deviations can be explained by the instrumental error associated with the analysis of c(DIC) and A_T discussed in Sect. 2.3.3.

2.4.2 Glider Data

Temperature, salinity, and oxygen validation

Since the sensors were calibrated before deployment, it was expected that the measurements from the glider would match those from the CTD, because any discrepancies between data sets would indicate possible instrumental or methodological issues with the glider measurements. Mean profiles of θ, salinity, and $c(O_2)$ collected by the glider and by ship (Fig. 2.6) agreed well. Values obtained by both ship and glider were mostly within one standard deviation of one another. Mean θ and salinity retrieved during the eight ship pH_s casts differed from the binned mean calculated using all available REP14 - MED ship casts at depths between 100 and 500 m. However, this is likely related to temporal or spatial variability as mean θ and salinity were within the range of all available glider measurements. Furthermore, differences of roughly 0.1 °C, 0.02, and 1.5 µmol kg^{-1} can be seen for θ, salinity, and $c(O_2)$, respectively, between the binned mean profile of CTD measurements and the binned mean profile of glider measurements at depths greater than 500 m. These differences in θ, salinity, and $c(O_2)$ are related to the different spatial distribution of the two datasets, as the glider measured predominantly at 40° N where deep cooler, fresher, waters were observed in the west (Fig. 2.4a-b), uncommon in other areas of the observational domain (Knoll et al., 2015b).

ISFET pH Validation

Mean pH_g and pH_s agreed best between 60 and 250 m (Fig. 2.7), although pH_g variability was a lot higher than for pH_s. Larger differences between these profiles can be seen above and below this depth range, with pH_g 0.1 higher at the surface and roughly 0.07 lower between 950 and 1000 m when compared with pH_s. The pH_s maximum at approximately 50 to 70 m depth was not apparent in the pH_g profile, with highest pH_g seen at the surface. The standard deviations for pH_g were large, between 0.044 and 0.114 in the top 150 m of the water column and between 0.027 and 0.053 at other points in the water column. Comparing all pH_g dive profiles obtained during the mission suggests a great degree of temporal and spatial variability, with pH ranging from 8.02 to 8.28 at the surface, and between 7.97 and

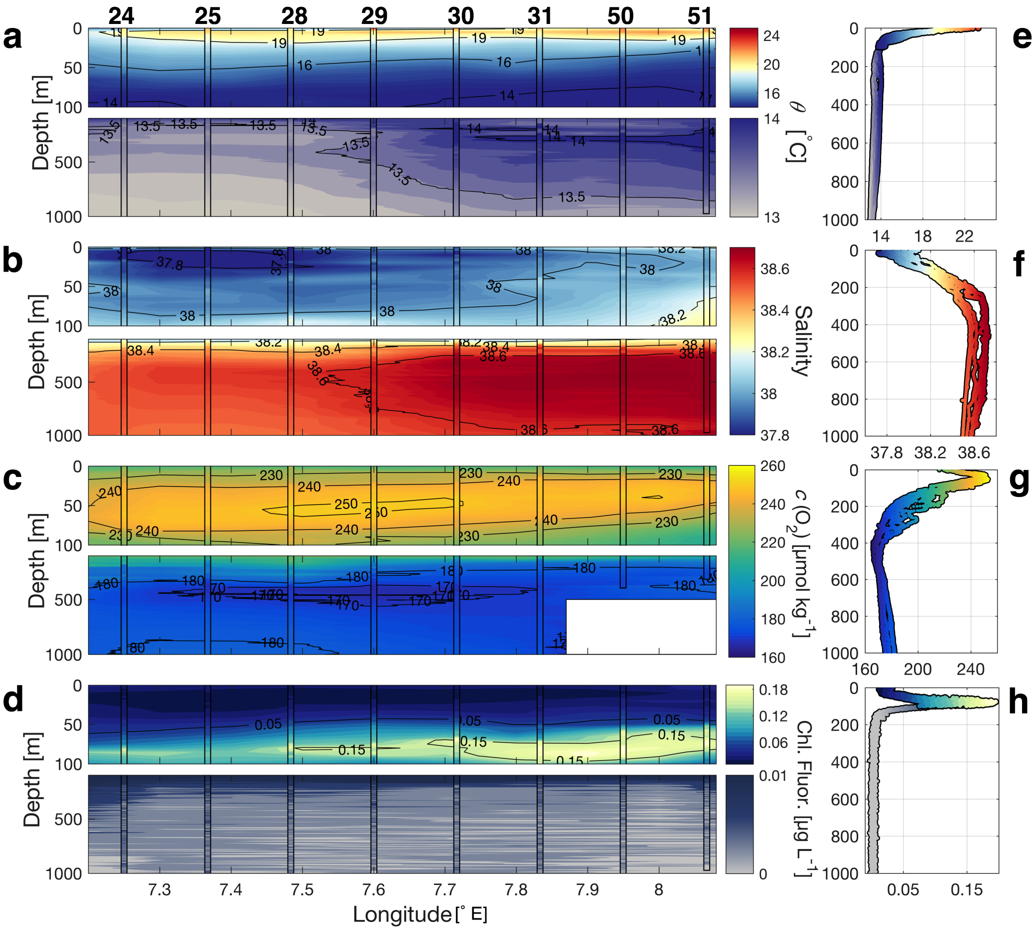

Figure 2.4: Transects of optimally interpolated (**a**) potential temperature (θ), (**b**) salinity, (**c**) dissolved oxygen concentrations ($c(O_2)$), and (**d**) chlorophyll fluorescence, along with their depth profiles (**e-h**), obtained by ship. These parameters were sorted into 0.1° longitude x 5 m bins, and the radius of influence used for optimal interpolation was 0.2° longitude x 20 m. The data retrieved during the eight CTD casts (displayed in Fig. 2.1) used for optimal interpolation are superimposed on top of the interpolated fields. The individual cast numbers for each ship profile are shown above panel a.

8.13 at 800 m depth. This large range of variability was seen for pH_g measured over just a few days relatively close in time and space to pH_s (Fig. A.1).

A diel cycle in pH_g anomalies (calculated by subtracting the all time mean from the hourly means within a given depth interval) was found predominantly at depths shallower than 20 m (Fig. 2.8b). Lower pH was found between 09:00 and 18:00 LT, decreasing by >0.1 between 12:00 and 14:00 LT. Contrastingly, potential temperature, salinity, and $c(O_2)$ anomalies (calculated in the same way as pH_g anomalies) did not have strong diel cycles (Fig. 2.8c-e), suggesting that the decrease in pH was not caused by changing environmental conditions. Particularly, one might expect $c(O_2)$ to have a similar pattern to pH if it were related to photosynthesis / respiration due to variations in $p(CO_2)$ (Cornwall et al., 2013; Copin-Montégut and Bégovic, 2002). However, $c(O_2)$ remained relatively

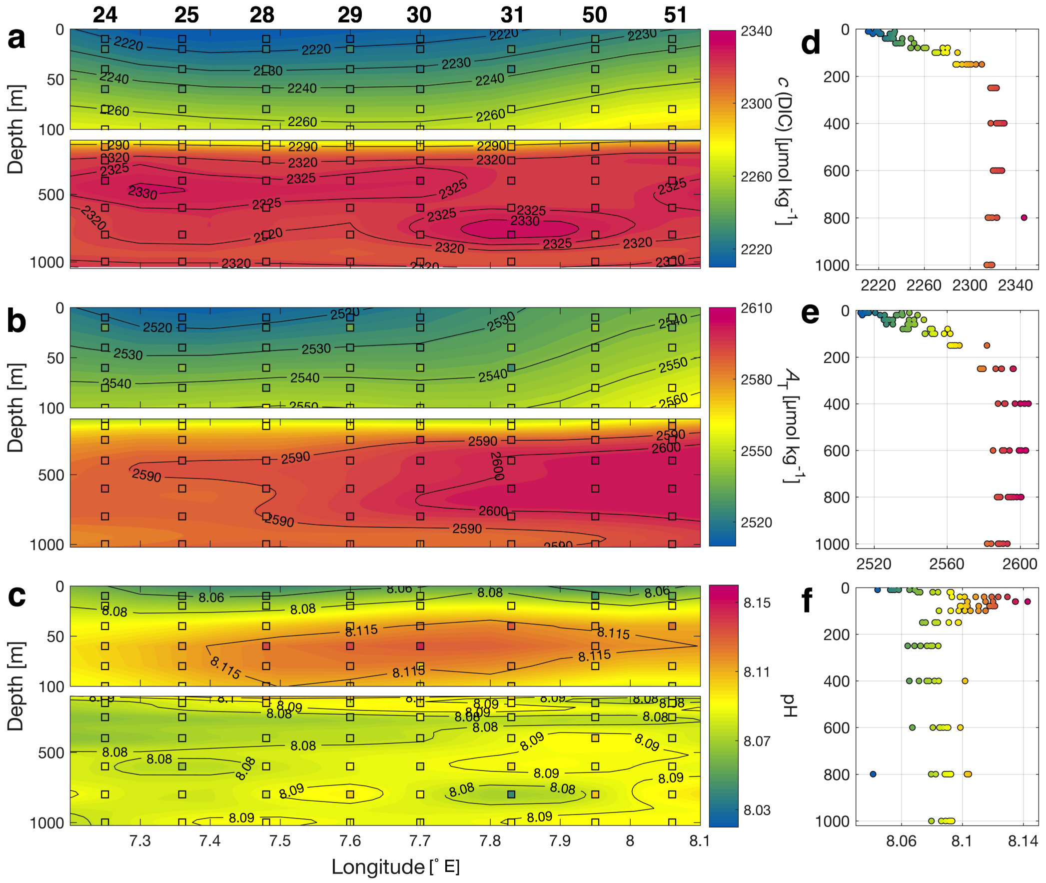

Figure 2.5: Optimally interpolated fields of (**a**) dissolved inorganic carbon (c(DIC)), (**b**) total alkalinity (A_T), and (**c**) pH derived using c(DIC) and A_T, are displayed, along with their depth profiles (**d-f**). These parameters were sorted into 0.1° longitude x 20 m bins, and the radius of influence used for optimal interpolation was 0.3° longitude x 200 m for c(DIC) and (A_T), and 0.3° longitude x 80 m for pH. The water sample values retrieved during the eight CTD casts (displayed in Fig. 2.1) used for optimal interpolation are superimposed on top of the interpolated fields as squares. The individual cast numbers for each ship profile are shown above panel a.

constant throughout the day at all depth ranges implying that the level of biological activity in the Sardinian Sea did not change on average throughout the day and hence would not have caused this reduction in pH_g.

The decrease in pH_g coincided with increased levels of solar irradiance (Fig. 2.8a) recorded at meteorological buoy M1 (Fig. 2.1) during the day at the surface, hence it was likely a light-induced instrumental artefact. The effect of light on the voltage output of FET-based sensors using SiO_2 and Si_3N_4 sensitive layers is known (Wlodarski et al., 1986), as the presence of photons can excite electrons in the valence band of the semiconductor material, creating holes and allowing the flow of electrons to the conduction band. This increases the voltage threshold, falsely measuring higher hydrogen ion activity, leading to lower apparent pH (Liao et al., 1999).

The effect of light on our sensor was investigated further by exposing two ISFET pH sensors to artificial light whilst placed in reference buffer solutions (TRIS and AMP) under laboratory conditions. The results (not shown here) confirmed that our ISFET sensor is affected by light. The light-induced offset depended on the strength and type of the light

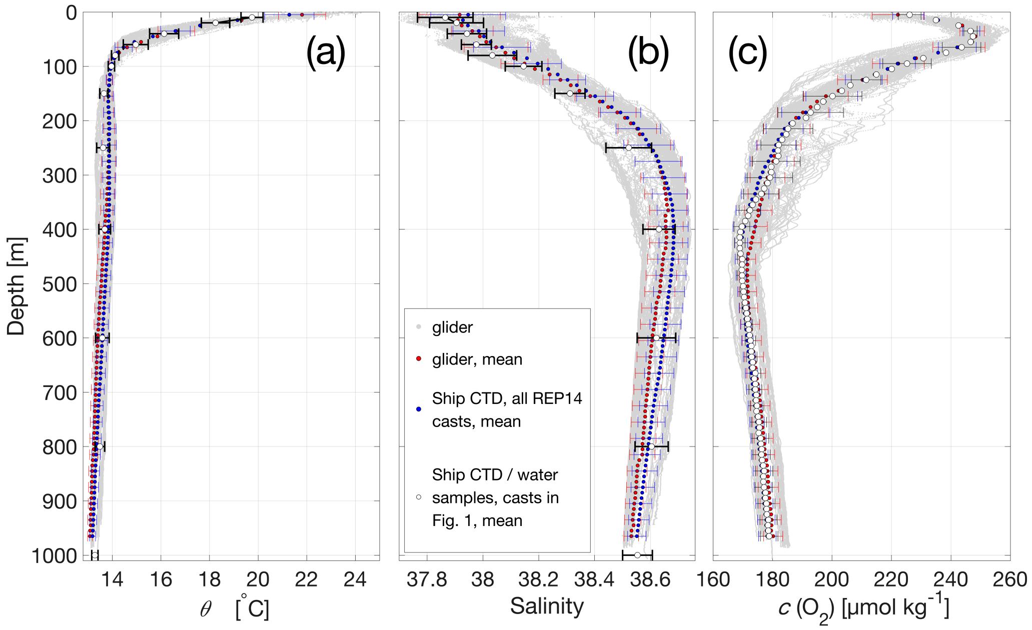

Figure 2.6: A comparison between measurements retrieved by the glider and those obtained by the ship CTD package. The binned mean (red) calculated using glider measurements (grey) are compared with the binned mean of CTD casts obtained from the entire REP14 - MED observational domain (blue), and the binned mean values obtained from water samples (SBE oxygen optode sensor for dissolved oxygen concentrations ($c(O_2)$)) during the eight CTD casts in Fig. 2.1 (white), for (**a**) potential temperature (θ), (**b**) salinity, and (**c**) $c(O_2)$. Standard deviations (calculated for every 10 m bin) are displayed as error bars in this figure every 30 m for glider and CTD measurements, but at every sampled depth for water samples.

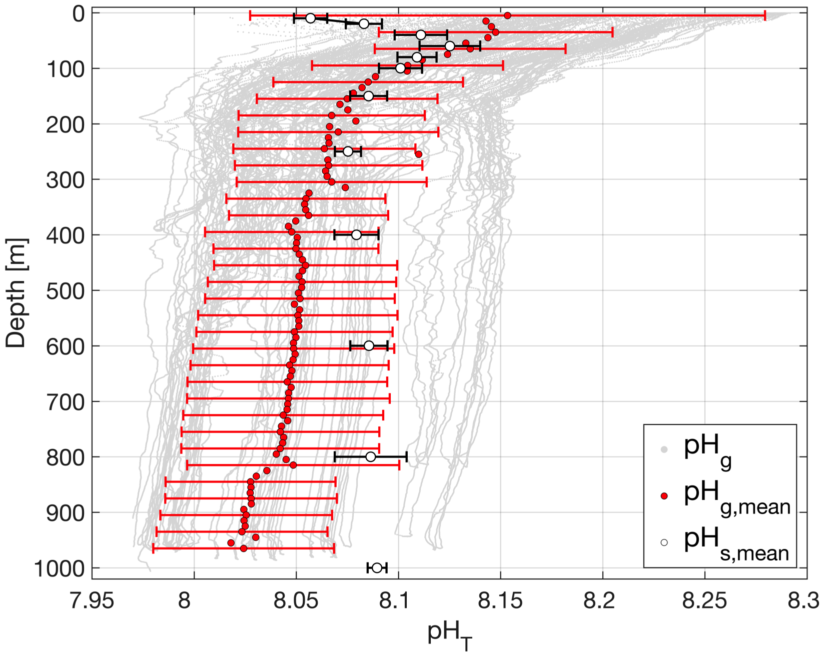

Figure 2.7: pH obtained by the glider ISFET sensor (pH_g, grey) is compared with the depth binned mean of these profiles (red), along with the corresponding standard deviation error bars (using 10 m bins) displayed in this figure every 30 m. Mean pH obtained by the ship (pH_s) during the eight CTD casts displayed in Fig. 2.1 are shown (white), with their relevant standard deviations displayed as error bars. Mean pH_g and their corresponding standard deviations were calculated using 10 m depth bins, whereas mean pH_s and standard deviations were calculated at each sampled depth.

source, and which sensor was being used. The offset remained relatively constant whilst the light was turned on. A maximum pH offset of -0.7 (-6 x 10^6 counts) and -0.15 (-3 x 10^6 counts) was found when the LED and halogen lights were used, respectively.

There were not enough dives for a robust light correction, and an irradiance measuring sensor was not attached to the glider, hence data collected within the top 50 m between 05:00 and 21:00 LT, representing roughly 5 % of all pH_g measurements, were not used in later analysis. In order to reduce this light effect on pH measurements in future, ISFET sensors will have to be placed on the underside of the glider or equipped with a light shield.

Comparing pH_g to pH_s indicated that the range observed by the ISFET sensor was much larger. It could be argued that this difference in range is due to the differing temporal and spatial resolution between the glider and the ship measurements. However, comparing pH_g further with pH measurements in the literature on a similar time and spatial scale (Álvarez et al., 2014) suggests that this is not an issue with resolution. $pH_{T,25}$ collected in the western Mediterranean Sea over a period of around 2 weeks (Álvarez et al., 2014), comparable in length to this trial, varied by roughly 0.02 at the surface and by around 0.08 at depths greater than 100 m. The range observed by the glider ISFET sensor was therefore thirteen times

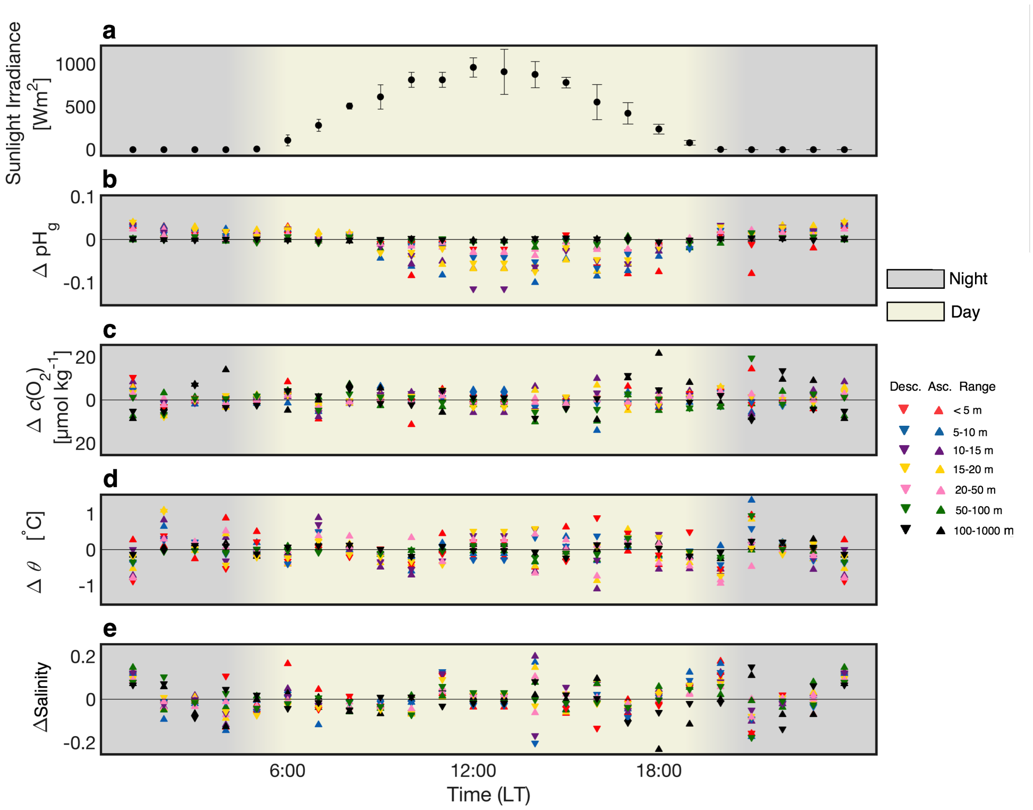

Figure 2.8: (**a**) Solar irradiance measured using a pyranometer on Meteorological buoy M1 (Fig. 2.1), (**b**) glider retrieved pH (pH$_g$), (**c**) dissolved oxygen concentrations ($c(O_2)$), (**d**) potential temperature (θ), and (**e**) salinity average anomalies (calculated by subtracting the all time mean from the hourly means within a given depth interval) for each hour of the day local time (LT) for five near-surface depth ranges; < 5 m, 5 - 10 m, 10 - 15 m, 15 - 20 m, and 20 - 50 m, and 2 deeper depth ranges; 50 - 100 m, and 100 - 1000 m, for both ascending (upward triangle) and descending (downward triangle) dive profiles. The grey shaded area represents the nighttime, whilst the lightly shaded area represents the daytime.

larger at the surface, and roughly 3 times larger at depths below 100 m. This difference in range cannot be explained by the high sampling frequency of the glider. Furthermore, the larger variations in pH$_g$ were not a result of changing environmental conditions, as evidenced by the relatively stable $c(O_2)$, θ, and salinity measured by the glider, discussed in Sect. 2.4.2.

It is likely that the ISFET pH measurements were not only related to the amount of hydrogen ion activity in the water, but also to the temperature and pressure that the sensor experienced, which was unexpected considering the sensor has previously shown good temperature and pressure characteristics (Shitashima et al., 2002; Shitashima, 2010; Shitashima et al., 2013). Furthermore, comparing ISFET measurements with pH$_s$ and pH presented by Álvarez et al. (2014) suggests that the accuracy of the sensor was not as good as that previously claimed (Shitashima et al., 2002). Therefore, it was necessary to correct pH$_g$ measurements for instrumental drift, temperature, and pressure.

The response of the ISFET sensor can be described by the Nernst equation (Eq. (2.1)), which relates sensor voltage to hydrogen ion activity:

$$E = E^{*} - m_N \; \lg(\, a(\mathrm{H}^{+})\, a(\mathrm{Cl}^{-})\,) \tag{2.1}$$

which incorporates the Nernst slope (Eq. (2.2)):

$$m_N = RT\ln(10)/F \tag{2.2}$$

where T is temperature (k), R is the gas constant ($8.3145\,\mathrm{J\,K^{-1}\ mol^{-1}}$), F is the Faraday constant ($96485\,\mathrm{C\,mol^{-1}}$), $a(\mathrm{H}^{+})$ and $a(\mathrm{Cl}^{-})$ are the proton and chloride ion activities, E is the measured voltage by the sensor (i.e. electromotive force), and E^{*} is representative of the two half-cells in the ISFET sensor forming a circuit (i.e. interface potential) (Martz et al., 2010). It is known that temperature and pressure have an effect on E^{*} (strong linear relationship), and that the Nernst slope is a function of temperature. Also studies have shown that it is possible for ISFET sensors to experience some form of hysteresis as a result of changing temperature and pressure (Martz et al., 2010; Bresnahan et al., 2014; Johnson et al., 2016).

The first step in correcting $\mathrm{pH_g}$ aimed to reduce the measured extent of variability to within the measured limits of $\mathrm{pH_s}$. This in-part removed the non-monotonous instrumental drift experienced by the sensor, which we think was likely due to the $E*$ between the two n type silicon parts of the semiconductor being affected. A depth-constant time-varying offset correction (i.e. one offset value determined for each dive, applied to the entire profile) was applied (Eq. (2.3)) using the difference between mean $\mathrm{pH_s}$ and each $\mathrm{pH_g}$ dive measurement where *in situ* temperature was 14.0 °C, as water with this temperature was situated at a depth below the thermocline for most dives, where the density gradient was weak.

$$\mathrm{pH_{Offset}} = \mathrm{pH_s(T),_{mean}} \;-\; \mathrm{pH_g(T)} \quad \text{for} \;\; \mathrm{T} = 14 \pm 0.1\,^{\circ}\mathrm{C} \tag{2.3}$$

The calculated offset values as a function of time were compared with salinity and $c(\mathrm{O_2})$ where *in situ* temperature was constant at 14 °C (Fig. 2.9). Variability in salinity and $\mathrm{c(O_2)}$ with time were strongly related ($\mathrm{r^2} = 0.97$), whereas the relationship between pH offset values and salinity, and $\mathrm{c(O_2)}$, were not ($\mathrm{r^2}$ of around 0.2). Furthermore, the majority of offset values were calculated below 100 m (Fig. 2.12d-f), where the density and pH gradients were weak. This indicated that our depth-constant time-varying offset correction decreased the apparent range of pH variability by an amount that was mostly associated with instrumental drift, rather than physical and biogeochemical variability. Applying these offsets to the data decreased the range of pH measured by the ISFET sensor by

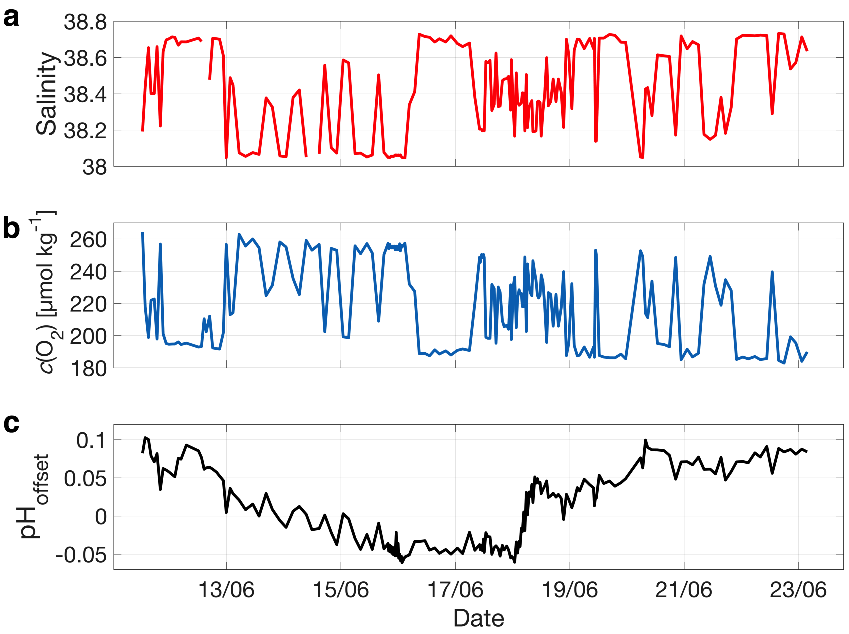

Figure 2.9: Salinity (**a**), dissolved oxygen concentrations ($c(O_2)$) (**b**), and the calculated pH offset values (**c**) as a function of time at the depth where *in situ* temperature was 14 ± 0.1 °C.

approximately two thirds (Fig. 2.10), with new pH_g standard deviations ranging between 0.009 and 0.048 within the top 150 m, and between 0.008 and 0.017 at greater depths.

After applying this offset correction, pH_g was further corrected for *in situ* temperature and pressure using linear regression models. The method is outlined below:

1. Calculate ΔpH (Eq. (2.4)) as the difference between mean pH_s and pH_g.

$$\Delta pH = pH_{s,mean} - pH_g \tag{2.4}$$

2. Determine the line of best fit between ΔpH and *in situ* temperature in the top 100 m of the water column where the temperature gradient was strongest using linear regression.

3. Correct pH_g for *in situ* temperature for the entire water column using the slope (m) and intercept (c) coefficients of the best fit line in step 2. to obtain $pH_{g,tc}$, where 'tc' stands for 'temperature corrected' values.

4. Calculate the difference between $pH_{g,tc}$ profiles and mean pH_s, producing ΔpH_{tc}, using an equation similar to Eq. (2.4).

5. Determine the line of best fit between ΔpH_{tc} and pressure for the lower 900 m of the water column using linear regression.

6. Correct $pH_{g,tc}$ for pressure for the entire water column using coefficients *m* and *c* in a similar way to step 3. to obtain $pH_{g,tpc}$, where 'tpc' stands for 'Temperature and Pressure corrected' values.

The derived equation used for correcting pH_g is shown below:

$$pH_{g,tpc} = pH_g - 0.021\,t/^{\circ}C + 4.5x10^{-5}\,P/dbar + 0.261 \tag{2.5}$$

where t is *in situ* temperature and P is pressure. A good fit was found between pH_g and *in situ* temperature, and a reasonable fit was found with pressure (Fig. 2.11). The standard deviations of $pH_{g,tpc}$ ranged between 0.008 and 0.039 in the top 150 m of the water column and between 0.007 and 0.013 at greater depth, a further decrease in apparent variability of 13% to 23 % and 14% to 31 % respectively (Fig. 2.10).

Johnson et al. (2016) ran a series of temperature and pressure cycling experiments when testing an ISFET pH sensor based on the Honeywell Durafet ISFET die. They found a temperature sensitivity of around $\partial pH / \partial t = -0.018$, similar to our calculated slope, and a pressure hysteresis of 0.5 mV (pH of around 0.01) at maximum compression (2000 dbar). This is equivalent to a pressure sensitivity of roughly $\partial pH / \partial P = 5x10^{-6}$, which is an order of magnitude smaller than in this study. This difference in pressure sensitivity could be related to the different housing materials used, as Johnson et al. (2016) used polyether ether ketone (PEEK), whereas acrylic resin was used for our sensor.

Salinity covaries with temperature and pressure, and some of the salinity dependence of the offset between pH_s and pH_g might have been mis-attributed to the regression coefficients associated with temperature and pressure. The sensor characteristics should therefore be studied in detail under controlled laboratory conditions. However, for the purposes of calibrating the high-resolution, but poor-accuracy measurements (relative to pH_s) obtained from the ISFET pH sensor, the present empirical correction based on temperature and pressure appears to be sufficient to achieve a match to within the pH repeatability of the discrete samples of between 0.004 and 0.017.

Coast To Open Ocean High Resolution Hydrographic and Biogeochemical Variability

Spatial and temporal variability can be seen in $pH_{g,tpc}$ for three individual east-west transects using measurements obtained within different time periods (Fig. 2.12a-c). This pH variability is likely related to air-sea exchange of CO_2 (weak), changes in temperature (indirectly), and biological activity (Yao et al., 2016). In the top 100 m, pH higher than 8.12 was found at depths ranging from 20 to 95 m, whereas lower pH ranging from 8.06 to 8.09 were present closer to the surface at some locations (e.g. between 7.5 and 7.7° E, and

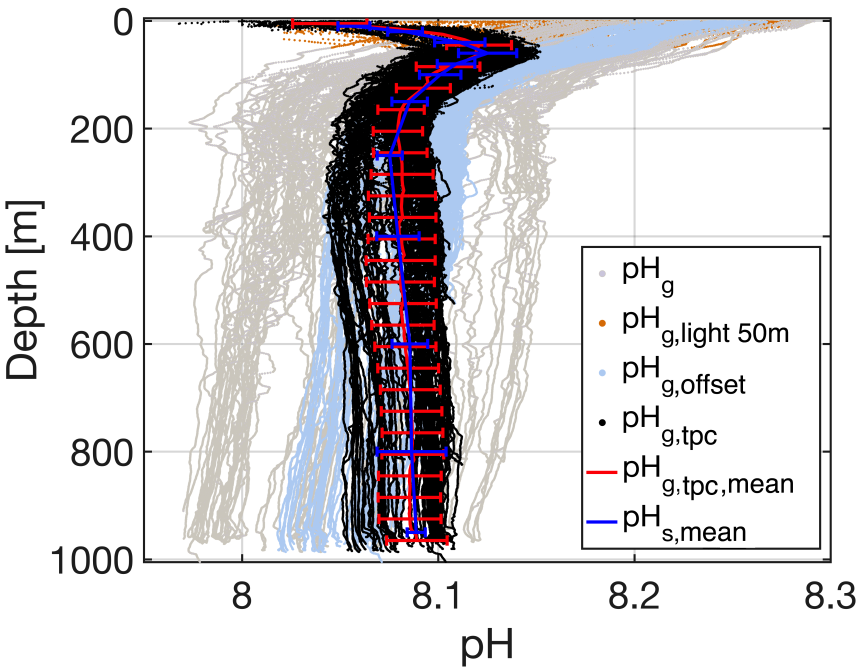

Figure 2.10: Profiles of glider retrieved pH (pH_g) pre-correction (grey), with a depth-constant time-varying offset correction applied (light blue), and further corrected for *in situ* temperature and pressure (black), are displayed. pH_g measurements affected by light in the top 50 m of the water column (orange) and not used for the drift, temperature and pressure corrections are also shown. The depth binned mean profile of drift, temperature and pressure corrected (tpc) pH_g (using 10 m bins) is shown in the foreground (red) along with the standard deviation ranges displayed every 40 m in this figure. The depth binned mean profile of pH measurements retrieved by ship (pH_s) is plotted for comparison (dark blue) with standard deviation ranges displayed at each sampled depth.

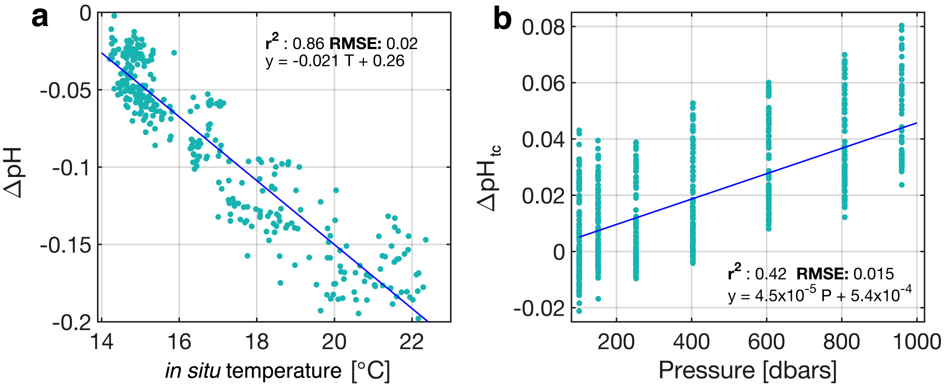

Figure 2.11: Linear regression fits are displayed for (**a**) ΔpH (difference between mean pH_s and pH_g corrected for drift) vs. *in Situ* temperature in the top 100 m of the water column, and (**b**) ΔpH corrected for *in Situ* temperature (ΔpH_{tc}) vs. pressure between 100 and 1000 m using all available dives. The r^2, the root mean square error (RMSE), and the equation of the line are displayed for each linear fit.

east of 8° E). pH maxima were found at depths between 40 and 70 m, where θ was around 15 °C (Fig. 2.12d-f), within the pycnocline (Fig. 2.12j-l). This band of high pH situated at 20 to 95 m depth corresponded with a thick layer of $c(O_2)$ rich water at similar depths (Fig. 2.12m-o). pH and $c(O_2)$ in the top 200 m of the water column more or less followed isopycnal surfaces at a range of points in time and space. For example, the slanted isopycnals closer to the coast (east of 7.95° E), associated with geostrophic shear, corresponded with horizontal gradients in pH and $c(O_2)$. Below 100 m, $c(O_2)$ decreased to a minimum of $< 170\,\mu\mathrm{mol\,kg^{-1}}$, which, although not spatially homogeneous, corresponded with generally colder, saltier, lower pH waters.

All three east-west transects can be separated into two parts roughly either side of 7.7° E for depths greater than 100 m. Lower pH of between 8.05 and 8.1 was found in the western part, whereas higher pH ranging from 8.07 to 8.12 was found in the eastern part, which was partially seen in the $\mathrm{pH_s}$ measurements (Fig. 2.5). The spatial variability of these east and west parts differed for each of the three time periods (times labelled in Fig. 12), with both the eastern high and western low pH patches changing in size vertically and horizontally, corresponding to spatial changes in θ and salinity. Furthermore, salinity, θ, and $c(O_2)$ were lower in the western section, compared with values found at similar depths in the eastern section (Fig. 2.12d-i, 2.12m-o).

In the top 100 m of the water column, variability in pH and $c(O_2)$ are likely related to biological activity and air-sea gas exchange. As discussed in Sect. 2.4.1, a DCM within this depth range is common in the Mediterranean Sea when waters are thermally stratified, and sufficient nutrients and light are available below the mixed layer (Estrada, 1996). High chlorophyll fluorescence was observed by the ship's sensor here (Fig. 2.4d). Enhanced $c(O_2)$ at these depths are likely the by-product of photosynthesis, and the higher pH were likely the result of changes in the carbon equilibrium due to the consumption of CO_2 (Cornwall et al., 2013; Rivaro et al., 2010; Copin-Montégut and Bégovic, 2002). A similar relationship between pH and primary production was described by Álvarez et al. (2014) in the western Mediterranean Sea. As discussed in Sect 2.4.1, the fresher waters found in the top 100 m are likely MAW.

The difference in pH between the eastern and western parts at depths greater than 100 m depth highlighted the variability of water masses in this region. In particular, the higher pH found in the eastern part of the transect (east of 7.7° E), coinciding with high A_T and $c(\mathrm{DIC})$ (Fig. 2.5), was likely related to the flow of LIW, as described in Sect. 2.4.1. The LIW flows from the eastern Mediterranean basin (east of the strait of Sicily), where pH is higher than in the western Mediterranean basin (Álvarez et al., 2014), towards the west along the continental shelf edge (Millot, 1999). This high pH found in the eastern section of the glider transect may therefore be remnants of these eastern Mediterranean waters. The low pH, low $c(O_2)$ waters found deeper than 100 m results from increased respiration and remineralisation of organic matter (Lefèvre and Merlivat, 2012), coinciding with higher

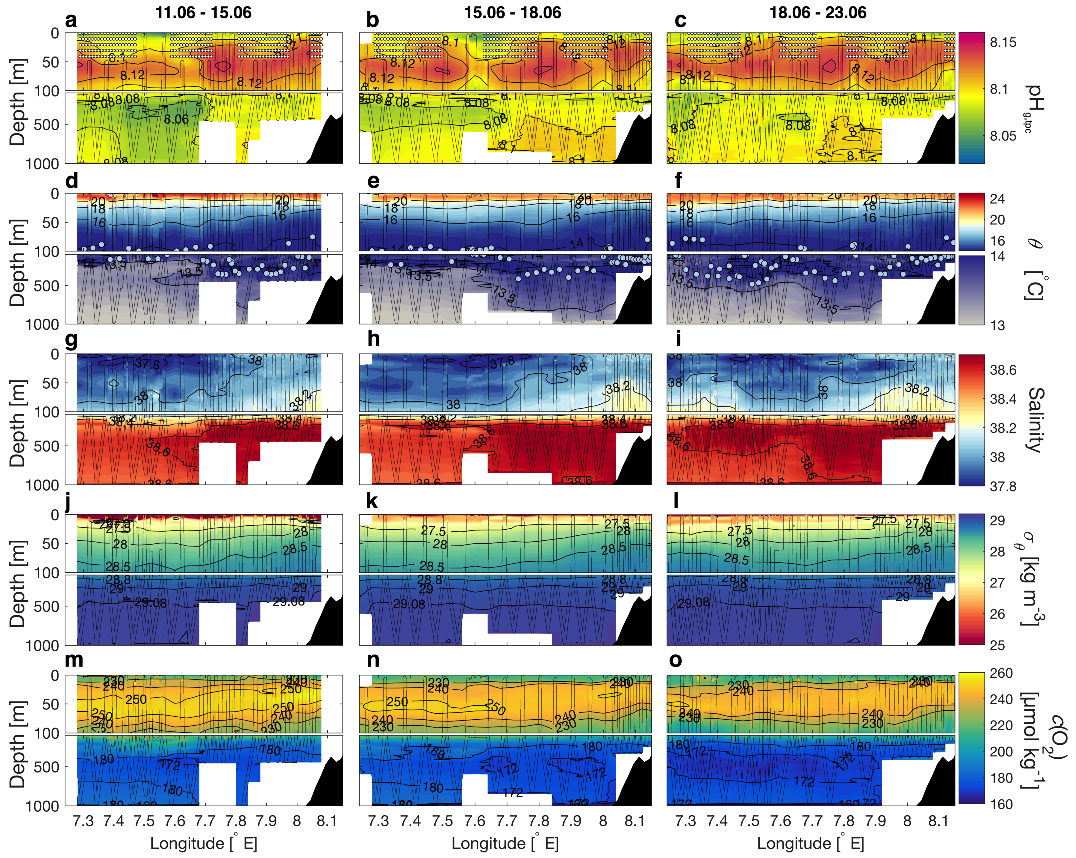

Figure 2.12: Objectively mapped transects of glider retrieved (**a-c**) pH corrected for drift, temperature, and pressure ($pH_{g,tpc}$), (**d-f**) potential temperature (θ), (**g-i**) salinity, (**j-l**) potential density anomalies (σ_θ), and (**m-o**) dissolved oxygen concentrations ($c(O_2)$), for three different time periods between 11th and 15th, 15th and 18th, and 18th and 23rd June, 2014. The spatial ranges of pH measurements affected by light and removed prior to corrections are represented by small white points in a-c. The depth-longitude points in which pH offsets were calculated at a temperature of 14 °C are indicated by pale blue points in d-f. Glider measurements were sorted into 0.04° longitude x 2 m bins, and the radius of influence used for optimal interpolation was 0.1° longitude x 10 m. Glider measurements used for optimal interpolation are superimposed on top of the interpolated fields for reference.

levels of c(DIC) deeper than 200 m (Merlivat et al., 2014), and which may have been more prominent in the western part of the transect (west of 7.7° E) leading to decreased levels of pH.

The pycnocline shallowed east of 7.7° E in the top 100 m of the water column during all three time periods (times labelled at the top of Fig. 2.12), which corresponded with shoaling high salinity, low pH, low $c(O_2)$ waters, and high c(DIC) , A_T, and chlorophyll fluorescence obtained by ship (Fig. 2.4 and Fig. 2.5). These features may be related to upwelling. Meteorological buoy M1 located south of the glider transect recorded an average surface wind direction of 198° towards the south-southwest which would be favourable for coastal upwelling. However, the mean wind speed was only 2 m s^{-1} which is weak. On the other hand, salinity maxima seen at depths of 200 to 700 m seem to suggest an intrusion of LIW westward. An intrusion of water away from the coast towards the open ocean has been shown to increase divergence in regions close to shore with strong alongshore currents (Roughan et al., 2005). Upwelling signatures at this longitudinal range along the Sardinian coast have been simulated, particularly in the summer, by Olita et al. (2013) using a hydrodynamic 3D mesoscale resolving numerical model. They suggest that a mixture of both current flow and wind preconditioned and enhanced upwelling in this region, which may have also been the case during our deployment. Furthermore, chlorophyll fluorescence (Fig. 2.4) obtained by ship was higher closer to shore, indicative of a greater abundance of biomass in the top 100 m perhaps fuelled by upwelled nutrients (Porter et al., 2016; El Sayed et al., 1994).

2.5 Conclusions

Our trials of an experimental pH sensor in the Mediterranean Sea uncovered instrumental problems that were unexpected and will need to be addressed in future usage. These are summarised here:

1. The data retrieved from the dual pH-$p(CO_2)$ integrated sensor, and from the $p(CO_2)$ unit of the stand-alone dual sensor could not be used due to quality issues. It is unclear why there was a problem with measurements obtained by the stand-alone $p(CO_2)$ unit, however we think the regular on/off cycling of power to the integrated dual pH-$p(CO_2)$ sensor in between sampling did not allow it to function properly. In future, we would suggest the addition of backup batteries to supply electricity to the sensor in between sampling.
2. The stand-alone pH sensor was subject to drift. This could be reduced by subtracting a depth-constant time-varying offset from each dive using the difference between pH_g and pH_s at a more dynamically stable depth, but such an approach is not generally recommended or valid. We think that a change in E* between the two n type silicon parts of the semiconductor might be the cause of the drift. To elucidate this drift further, in future two ISFET sensors should be tested in laboratory conditions within a bridge circuit to attempt to isolate possible factors contributing to drift. Focussing on the root cause of the sensor drift, rather than correcting the pH data for drift after the deployment, would be more beneficial to the longterm study of ISFET pH-$p(CO_2)$ sensors.
3. The sensor was apparently affected by temperature and pressure, but it is unclear to what extent the empirical relationship between *in situ* temperature and ΔpH in the thermocline (top 100 m) and between pressure and ΔpH_{tc} in the deeper water (100 - 900 m) can be generalised.

4. The effect of light caused the sensor to measure lower levels of pH_g in surface waters. This effect is expected to be ubiquitous wherever the sensor nears the surface during daytime. In future, the sensor will have to be positioned on the underside of the glider or equipped with a light shield to limit the effect of the sun when close to the surface.

Despite the overall disappointing performance, we were able to demonstrate the potential use of the corrected glider pH measurements for uncovering biogeochemical variability associated with biological and physical mesoscale features. pH_g corrected for drift, temperature, and pressure, was compared temporally and spatially with other physical and biogeochemical parameters obtained by the glider. These comparisons indicated that pH in the top 100 m of the water column was mostly related to biological activity, where $c(O_2)$ was high. Below 100 m, low pH west of of 7.7° E was likely linked to the remineralisation of organic matter, whilst east of this point, higher pH may have been transported from the eastern Mediterranean basin via LIW. Shoaling isopycnals east of 7.7° E closer to shore may have been indicative of upwelling, and possible upwelling signatures at the same location could be seen in salinity, θ, pH, $c(O_2)$, $c(\mathrm{DIC})$, A_T, and chlorophyll fluorescence.

3

Net Community Production and pH During Spring in the Northwestern Mediterranean Sea Using Glider and Buoy measurements

Publication

This chapter is in preparation for submission to the *Journal of Geophysical Research: Oceans* under the title ‘Net Community Production and pH During Spring in the Northwestern Mediterranean Sea Using Glider and Buoy measurements’, with co-authors Jan Kaiser, Karen J. Heywood, Jacqueline Boutin, Liliane Merlivat, Dorothee C.E. Bakker, *et al.* All scientific work and writing was undertaken by Michael Hemming, with improvements made using comments from co-authors.

3.1 Summary

The Mediterranean Sea comprises just 0.8 % of the global oceanic surface, yet for its size is regarded as an important sink for anthropogenic carbon due to its physical and biogeochemical characteristics. A unique dataset of high-resolution biogeochemical and physical measurements was obtained by an underwater glider close to the location of the BOUSSOLE and DyFAMed biogeochemical buoys in the northwestern Mediterranean Sea in March 2016. The glider deployment offered an opportunity to test an experimental

ion-sensitive field-effect transistor (ISFET) pH sensor attached to a glider. The pH measurements obtained by the ISFET sensor were corrected for drift, temperature and pressure effects. The timing of the phytoplankton bloom in the northwestern Mediterranean Sea varies year-on-year. Measurements of the fugacity of CO_2 obtained by the BOUSSOLE biogeochemical buoy at 10 m decreased between March 19 and April 1, following a period of intense mixing. The fugacity of CO_2 and total alkalinity at BOUSSOLE were used to derive dissolved inorganic carbon concentrations. Dissolved oxygen concentrations, pH, and optical backscatter observed by the glider at 10 m depth increased between March 19 and April 1. These changes indicated the start of a phytoplankton bloom. Mean net community production (*N*) rates were estimated from the glider dissolved oxygen concentrations, as well as dissolved inorganic carbon concentrations. *N* calculated using dissolved inorganic carbon concentrations derived at the BOUSSOLE biogeochemical buoy were compared with *N* calculated using glider dissolved inorganic carbon concentrations. Data collected by gliders allow the calculation of advection. The advection terms were large, indicating that advection should not be ignored. Mean daily *N* at the DyFAMed / BOUSSOLE site using glider and buoy estimates ranged between $-82 \pm 317\,\mathrm{mmol\,m^{-2}\,d^{-1}}$ and $460 \pm 870\,\mathrm{mmol\,m^{-2}\,d^{-1}}$ during the deployment. The large range in *N* estimates, and the negative *N* estimates during the time of the Spring bloom were unexpected when considering that the range of *N* estimated by Coppola et al. (2018) and Copin-Montégut (2000) was smaller (although a direct Spring bloom comparison was not possible), and positive *N* is associated with an increase in primary productivity. The *N* uncertainties are high largely due to errors associated with the inventory change and advection fluxes.

3.2 Introduction

Around a quarter of anthropogenic carbon dioxide emitted between 2007 and 2016 was absorbed by the oceans (Le Quéré et al., 2018). On timescales of less than a day to many months, carbon dioxide in the ocean is influenced by biological processes, such as primary production and respiration, and physical processes, such as air-sea gas exchange, mixing, and advection (Hood and Merlivat, 2001; Takahashi et al., 2002; Copin-Montégut et al., 2004; Hall et al., 2004; Alkire et al., 2014). Understanding the biological and physical processes affecting export of carbon from the surface to the interior ocean is vital for quantifying the effects of a future warmer climate.

Although the surface area of the Mediterranean Sea ($2.5\times10^{12}\,\mathrm{m^2}$) represents just 0.8 % of oceans globally, for its size is regarded as an important sink for anthropogenic carbon dioxide emissions due to higher water column levels of anthropogenic carbon compared with the Atlantic or Pacific Oceans (Lee et al., 2011; Schneider et al., 2010). This is due to a low Revelle factor related to relatively warm, salty, and high alkalinity waters, encouraging a net flux of carbon dioxide from the atmosphere to the ocean. Carbon dioxide dissolves in water as CO_2(aq) and carbonic acid (H_2CO_3), and dissociates to carbonate species bicarbonate (HCO_3^-), and carbonate (CO_3^{2-}), releasing H^+ ions (Zeebe and Wolf-Gladrow, 2001). H_2CO_3, CO_3^{2-}, HCO_3^-, and CO_2 are termed dissolved inorganic carbon (c(DIC); 'c' refers to a concentration), with HCO_3^- accounting for 90 % of c(DIC). Carbon dioxide absorbed by the ocean is thought to reach the interior via deep water formation and biological processes (Álvarez et al., 2014; Arrigo et al., 2008). The role of biological processes within the euphotic zone in the Mediterranean Sea is important in understanding the uptake of carbon, as oceanic carbon dioxide can be utilised by primary producers for photosynthesis, or produced by respiration.

Whether a location is predominantly autotrophic or dominated by respiration determines the sign of net community production (N), which is defined as total respiration (by phytoplankton, zooplankton, and bacteria) minus autotrophic gross primary production (by phytoplankton) (Alkire et al., 2012). The timing of the bloom in the northwestern Mediterranean Sea varies year-on-year; sometimes it begins in March, and sometimes it begins in April. This has been observed at the BOUSSOLE (Bouée pour l'acquisition de Séries Optiques à Long Terme) buoy close to the DyFAMed (Dynamique des Flux Atmospheriques en Mediterraneé) site located in the Ligurian-Provençal basin (7.90° E, 43.36° N) between 2013 and 2015 (Merlivat et al., 2018). Significant increases of particulate and dissolved organic carbon concentrations have been observed after bloom events, which is an important component of the 'biological pump', leading to export in some ocean regions (Carlson et al., 1998; Van Der Loeff et al., 1997; Alkire et al., 2014).

The DyFAMed site is considered an open ocean location as it is roughly 52 km from the coastline with a bottom depth > 2000 m. Few studies have estimated N at the DyFAMed site. A recent study estimated an annual mean oxygen net community production (N_{O_2}) of 9.2 mol m^{-2} a^{-1} (equivalent to 25.2 mmol m^{-2} d^{-1}), and monthly mean O_2 production estimates of between 11 mmol m^{-2} d^{-1} and 19 mmol m^{-2} d^{-1} in March-April, using excess O_2 above 100 % saturation over a period of 20 years (Coppola et al., 2018). Marty and Chiavérini (2002) estimated carbon phytoplankton new production (which does not account for heterotrophic carbon consumption) at between 19 g m^{-2} a^{-1} and 71 g m^{-2} a^{-1} (N_{O_2} of up to 17.6 mmol m^{-2} d^{-1} when applying an O_2:C stoichiometric ratio of -1.45 (Hedges et al., 2002; Anderson, 1995)) using monthly measured primary production at DyFAMed between 1993 and 1999 calculated using the ^{14}C method. Furthermore, Copin-Montégut (2000) estimated carbon-based N (N_C) at between 0.4 mol m^{-2} a^{-1} and 1.5 mol m^{-2} a^{-1} (N_{O_2} of between 1.6 mmol m^{-2} d^{-1} and 6 mmol m^{-2} d^{-1}) in the top 40 m over four days in May 1995 using O_2 concentrations and a vertical diffusion model. The particulate and dissolved carbon export fluxes at DyFAMed have been estimated as roughly 0.1 to 0.16 mmol m^{-2} d^{-1} (between 1988 and 2005) (Miquel et al., 2011) and 2.7 to 4.2 mmol m^{-2} d^{-1} (in 1991 and 1992) (Avril, 2002; Lefevre et al., 1996; Copin-Montégut and Avril, 1993).

These *N* estimates are local to the DyFAMed site, therefore representing a very small area. There are currently no *N* estimates incorporating the wider area surrounding the DyFAMed site.

The northwestern Mediterranean Sea displays strong seasonal variability. At the surface, temperatures remain at around 13 °C to 14 °C during the winter, increasing from spring to maxima of 26 °C to 28 °C during the summer. Wind-driven vertical mixing in the top 300 m is dominant during winter and autumn, whilst surface stratification is common during the summer as a result of solar heating (Copin-Montégut et al., 2004). At times when vertical mixing is the dominant process, nutrients can be transported from greater depths to otherwise nutrient-lacking surface waters (Marty and Chiavérini, 2002; de Fommervault et al., 2015). A combination of nutrient availability and increased stability driven by an increase in temperature by a few tenths of a degree Celsius can be enough for phytoplankton blooms to occur (Yao et al., 2016; Copin-Montégut et al., 2004).

Understanding physical and biological processes in the northwestern Mediterranean Sea requires sufficient data coverage. Historically, few carbon time series have been maintained continuously at moored buoys. One example is the DyFAMed site, which is complemented by monthly ship hydrocasts (Copin-Montégut et al., 2004; Antoine et al., 2008). This biogeochemical buoy is useful for studying processes occurring at specific depth levels at one location (Merlivat et al., 2018; Copin-Montégut et al., 2004; Hood and Merlivat, 2001), but a lack of vertical and horizontal spatial information is a limiting factor when studying the wider area in more detail. Autonomous underwater gliders have been used to survey the northwestern Mediterranean Sea since 2005 (Niewiadomska et al., 2008; Cyr et al., 2017). Underwater gliders are useful platforms for a range of physical and biogeochemical sensors. Gliders can survey depths of up to 1000 m using battery power, allowing autonomous manoeuvrability, while lasting for months in the field (Eriksen et al., 2001; Piterbarg et al., 2014; Queste et al., 2012). The deployment of autonomous platforms, such as underwater gliders, complements fixed-depth time series by enabling observations of biogeochemical and physical horizontal and vertical gradients in high-resolution.

Quantifying *N* at the DyFAMed site (and globally) help us to understand the role of biological production and consumption on carbon export from the surface to deep waters. If the rate of carbon export is known, the rate of atmospheric CO_2 drawdown into the ocean can be better quantified, and the accuracy of future climate projections might improve. Using underwater gliders as tools to observe the water column on timescales of less than a month over a wider area allow us to estimate physical processes (e.g. mixing, advection) that affect biological activity, and therefore *N*.

This Chapter aims to estimate *N* at the DyFAMed site in the northwestern Mediterranean Sea using *in situ* continuous measurements from a moored buoy and an underwater glider deployed in March-April 2016. Experimental methods used for measurements obtained by ship, buoys, and glider are described in Section 3.3. Environmental conditions leading up to, and during the spring bloom are discussed in Section 3.4. The method of estimating N using dissolved oxygen concentrations ($c(O_2)$) and c(DIC) budget approaches, along with results and discussions, are presented in Sections 3.5 and 3.6. Finally, N estimated in this study is compared with the literature in Section 3.7, and the chapter's conclusions can be found in Section 3.8.

3.3 Data Collection and Quality

3.3.1 Ship-Based Observations

Water samples were collected by the *RV Thetys II* within the framework of BOUSSOLE and DyFAMed on March 7 and April 16 2016 at DyFAMed roughly 52 km southeast from Nice, France in the northwestern Mediterranean Sea (Fig. 3.1). Sensor measurements of *in situ* temperature, salinity, and $c(O_2)$, were supplemented by discrete water samples of $c(O_2)$, c(DIC), total alkalinity (A_T), and nutrient concentrations (combined nitrite (NO_2^-) and nitrate (NO_3^-), silicate ($Si(OH)_4$), and phosphate (PO_4^{3-})) on March 7 and April 16.

Ship sensor measurements of *in situ* temperature and salinity were obtained using a Sea-Bird Scientific SBE 9 CTD instrument package. Ship CTD temperature and salinity measurements were binned vertically every 1 m. The $c(O_2)$ were measured using a Sea-Bird Scientific SBE 43 sensor. Data were visually inspected for erroneous values (e.g. abnormally high or low values) and using statistics, with $< 1\,\%$ of values considered to be outliers and flagged.

Water samples used to measure $c(O_2)$ were obtained on March 7 and April 16 using 12 L Niskin bottles (General Oceanics 1010X) attached to a carousel water sampler. The bottles were closed at ten depths during the March 7 upcast and at eight depths during the April 16 upcast within the top 1000 m of the water column; four of these depths were within the top 100 m (Fig. 3.2b). Reagents needed for the fixation of oxygen were added to the samples at the time of water sample collection onboard the ship. An automated Winkler titration method with endpoint detection was used after each cruise in the laboratory at the Observatoire Océanologique de Villefranche sur Mer to determine $c(O_2)$. Replicates were obtained to determine instrument precision. $c(O_2)$ measured by the rosette-mounted SBE43 sensor within the top 150 m were at points $15\,\mathrm{mmol\,m^{-3}}$ higher than the Winkler measurements (Fig. 3.2b). A trend was present in the depth-dependent ratio between Winkler measurements and $c(O_2)$ Sea-Bird Scientific SBE43 sensor bottle measurements collected between February 5 and April 16 2016 in the top 100 m. This trend may be related to the methods used to measure Winkler $c(O_2)$ measurements (e.g. the storage of the bottles). Ship Winkler 10 m depth O_2 saturation on March 7 was 95.3 %, while ship SBE43 sensor O_2 10 m depth saturation on March 7 was 98.2 % which is closer to the longterm average of 98.7 % close to the BOUSSOLE region (8° E to 9° E, 43° N to 44° N) in March using the World Ocean Atlas (WOA) 2013 climatology (https://www.nodc.noaa.gov/ cgi-bin/OC5/woa13/woa13oxnu.pl).

Seawater collected at ten depth levels at DyFAMed was also used to measure c(DIC) and

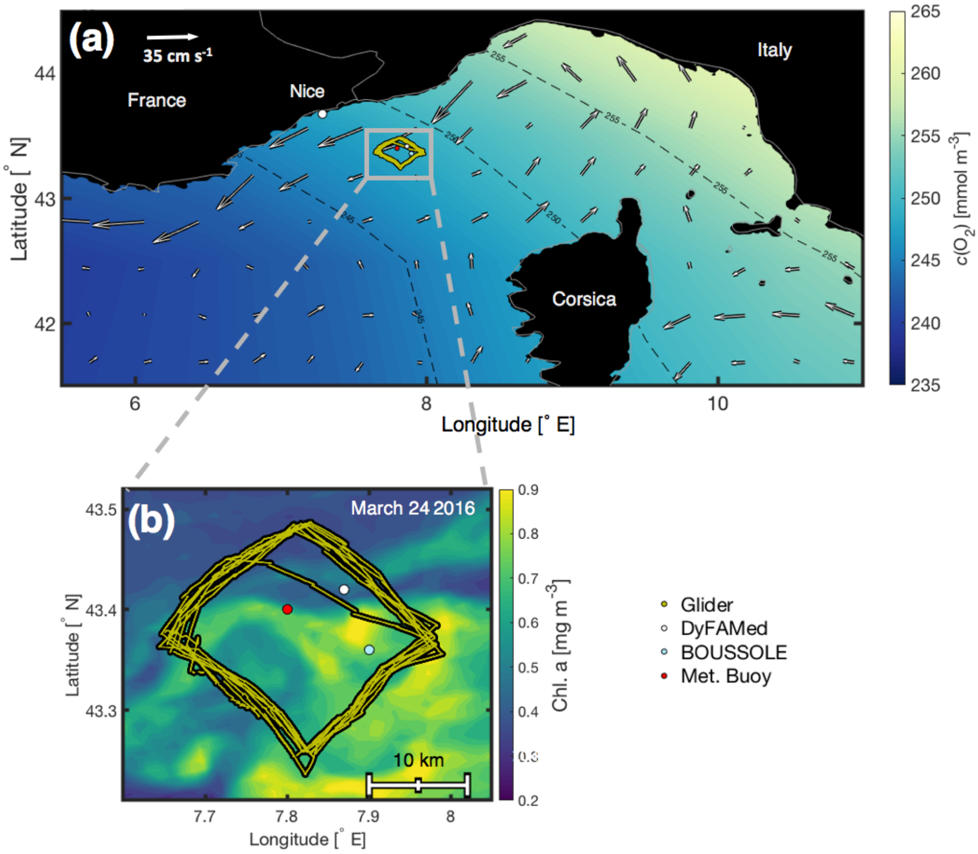

Figure 3.1: (a) The northwestern Mediterranean Sea and glider deployment area (small grey box) superimposed on top of the World Ocean Atlas (WOA) 2013 dissolved oxygen concentration ($c(O_2)$) March climatology, with accompanying AVISO satellite absolute mean surface currents (cm s^{-1}, white arrows) for the period of March 6 to April 6, 2016. WOA 2013 climatolgical data were downloaded from the National Oceanography Data Centre (https://www.nodc.noaa.gov/OC5/woa13/woa13data.html), and AVISO satellite absolute mean surface currents were downloaded from the Copernicus Marine Environment Monitoring Service (http://marine.copernicus.eu/services-portfolio/access-to-products). (b) A close-up of the deployment area at the DyFAMed / BOUSSOLE site. The position of each glider data point (yellow), the location of the DyFAMed mooring and the approximate location of ship measurements (white), the BOUSSOLE buoy (light blue), and the meteorological buoy (red), are superimposed on top of surface chlorophyll *a* concentrations (https://oceancolor.gsfc.nasa.gov/products/) on March 24 2016 derived using satellite algorithms described by Hu et al. (2012). As the deployment region is offshelf, the bathymetry in this area is flat and greater than 2000 m depth.

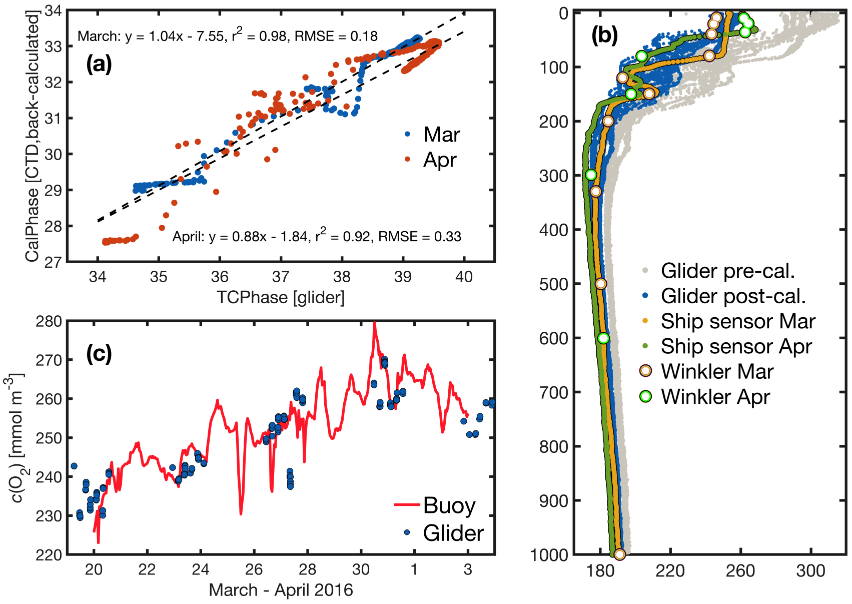

Figure 3.2: Calibration of the glider dissolved oxygen concentration ($c(\mathrm{O_2})$) sensor. (a) The linear regression fit using back-calculated ship pseudo-CalPhase and glider TCPhase for March 7 (orange) and April 16 (blue), along with the corresponding linear equations, r^2 and root mean squared errors (RMSE). (b) Glider $c(\mathrm{O_2})$ measured on March 8-9 and on April 3-4 before (grey), and after (blue) calibration, the ship sensor $c(\mathrm{O_2})$ on March 7 (yellow) and on April 16 (green), and the $c(\mathrm{O_2})$ Winkler samples on March 7 (white with red border) and on April 16 (white with green border). (c) Glider sensor $c(\mathrm{O_2})$ at 10 m depth < 10 km away from the BOUSSOLE buoy (blue spots) are compared with the BOUSSOLE buoy sensor $c(\mathrm{O_2})$ measurements (red line) at 10 m depth.

A_T. Seawater was transferred into 200 mL borosilicate glass bottles from the Niskin bottles using tygon tubing. Bottles were rinsed twice, and were allowed to overflow for roughly 20 seconds to ensure the bottle volume was flushed twice. Seawater samples were poisoned, and sealed within glass bottles using greased stoppers. These stoppers were kept in place with elastic bands, and the samples were stored in a dark place (Dickson et al., 2007). A Marianda Versatile INstrument for the Determination of Titration Alkalinity (VINDTA 3C; www.marianda.com) was used to measure c(DIC) and A_T. During this process, 19 bottles of certified reference material (CRM) supplied by the Scripps Institution of Oceanography (San Diego, CA, USA) were run to calibrate the instrument. Coulometry following standard operating procedure (SOP) 2 was used to measure c(DIC) (Johnson et al., 1985), and potentiometric titration following SOP 3b was used to measure A_T (Mintrop et al., 2000). Both SOPs are described in detail by Dickson et al. (2007). The CO2SYS programme (Van Heuven et al., 2011) was used to derive $\mathrm{pH_T}$ from c(DIC) and A_T measurements at DyFAMed for calibrating glider ISFET $\mathrm{pH_T}$. The method of using CO2SYS is explained in more detail in Sect. 3.3.4.

Nutrients at DyFAMed were measured using water collected in the same Niskin bottles as those used for $c(O_2)$, c(DIC), and A_T. Seawater samples were poisoned with saturated $HgCl_2$ solution, and were stored in 60 mL polyethylene flasks in a freezer. At the Observatoire Océanologique de Villefranche sur Mer laboratory, nutrient samples were analysed via a standard automated colourimetry system, using a Seal Analytical continuous flow AutoAnalyser III (AA3). Nitrogen-based nutrients NO_3^- and NO_2^- were analysed following the procedure described by Bendschneider and Robinson (1952), $Si(OH)_4$ was analysed following the procedure of Murphy and Riley (1962), and PO_4^{3-} was analysed according to the procedure by Strickland and Parsons (1972). The detection limits of NO_3^- and NO_2^-, $Si(OH)_4$, and PO_4^{3-}, were 0.01 mmol m^{-3}, 0.02 mmol m^{-3}, and 0.02 mmol m^{-3}, respectively (de Fommervault et al., 2015).

3.3.2 Fixed-Location Time Series Observations

Measurements of the fugacity of carbon dioxide ($f(CO_2)$), which is similar to the partial pressure of carbon dioxide but accounts for the non-ideality of CO_2 (Weiss, 1974; Wanninkhof and Thoning, 1993), were obtained at a depth of 10 m from the BOUSSOLE buoy (7.87° E 43.42° N, Fig. 3.1) in March - April 2016. The measurements of $f(CO_2)$ were made using spectrophotometry based on the optical absorbance of thymol blue pH indicator in seawater (Hood and Merlivat, 2001). Inside an exchanger cell, CO_2 in the seawater surrounding the instrument equilibrates with the pH indicator across a silicon membrane. The change in the optical absorbance of the indicator due to changing pH is measured spectrophotometrically (Hood and Merlivat, 2001; Copin-Montégut et al., 2004). The CARIOCA sensor at the BOUSSOLE site monitored $f(CO_2)$ on an hourly basis using three wavelengths, and was replaced roughly every 6 months with a newly calibrated instrument (Merlivat et al., 2018). The accuracy of the CARIOCA $f(CO_2)$ sensor is 3 μatm (Hood and Merlivat, 2001; Copin-Montégut et al., 2004). Seawater samples at 10 m depth are collected monthly by ship to perform *in situ* calibrations of A_T, c(DIC), and derived $f(CO_2)$ (Merlivat et al., 2018). Temperature and salinity were measured hourly using two Sea-Bird Scientific SBE 37-SM MicroCat sensors at the BOUSSOLE buoy at 10 m depth, and $c(O_2)$ were obtained using a Seabird SBE 43 sensor at 10 m depth. Samples for $c(O_2)$ Winkler titration were collected by ship monthly to correct for $c(O_2)$ sensor drift at the BOUSSOLE biogechemical buoy (Coppola et al., 2018). Salinity measurements obtained by one of the BOUSSOLE sensors were not available after March 15 due to instrumental problems, and recorded values before this date were on average 0.068 lower than recorded values from the other BOUSSOLE salinity sensor, and the salinity sensor measurements and water samples collected by ship on March 7 at the same depth. The root mean square difference between both BOUSSOLE salinity sensors after correcting the low salinity sensor using this offset of 0.068 was 3.6×10^{-3}. Data obtained by the BOUSSOLE buoy and the monthly ship cruises are available from http://www.obs-vlfr.fr/Boussole/. Measurements of $f(CO_2)$ obtained by the CARIOCA sensor were normalised to a temperature of 13 °C ($f_{13}(CO_2)$) following the method described by Takahashi et al. (1993) in order to remove temperature effects. $f_{13}(CO_2)$ is used for discussion or display purposes only.

The meteorological buoy 'Côte D'Azur' maintained by Météo-France is located close to the BOUSSOLE buoy (7.83° E 43.38° N, Fig. 3.1). This meteorological buoy measures near-surface (3.8 m) wind speed (extrapolated to 10 m by adding10 %) and direction, air temperature, relative humidity, sea surface salinity, precipitation, and other meteorological parameters. Data can be retrieved using the SErvice de DOnnées de l'OMP (SEDOO) Mistrals database (http://mistrals.sedoo.fr/Data-Download/), or can be viewed online (http://www.obs-vlfr.fr/data/view/dyfamed/meteo/). Wind speed and sea level pressure were used in this study.

3.3.3 Glider Observations

An iRobot Seaglider model 1KA (SG537) with an ogive fairing operated by the University of East Anglia (UEA) was deployed close to the DyFAMed mooring site. A total of 147 dives (294 profiles) were completed by the glider between March 7 and April 5 2016 covering a diamond-shaped observational domain between 7.65° and 8.00° E, and 43.25° and 43.50° N (Fig. 3.1). The glider was equipped with a non-pumped SBE model CTD sensor, an Aanderaa model 4330 oxygen optode sensor, a WET Labs Eco Puck sensor measuring optical backscatter at two wavelengths (470 nm and 700 nm), and two paired experimental ion-sensitive field-effect transistor (ISFET) pH and $p(CO_2)$ sensors (Shitashima et al., 2013; Hemming et al., 2017).

Conductivity, *in situ* temperature, and pressure were measured by the glider CTD sensor. Potential temperature (θ) and practical salinity were calculated using these parameters. All physical and biogeochemical data retrieved by the glider were checked for inconsistencies, and outliers identified outside depth specified standard deviation ranges (e.g. 3.5 x standard deviation for depths > 400 m or 10 x standard deviation for depths < 400 m) were flagged and discarded from further analysis. Fewer than 1 % of glider measurements were flagged in this way.

Glider $c(O_2)$ were calibrated to take into account the response time (τ) of the sensor, which is dependent on the thickness, and usage of the sensor foil (McNeil and D'Asaro, 2014), as well as temperature, and to account for the difference between the glider measurements and $c(O_2)$ obtained by the ship (Fig. 3.2b). This oxygen calibration closely followed the method outlined by Binetti (2016), and used by Hemming et al. (2017). It is briefly described here and illustrated as a schematic (Fig. 3.3). To correct $c(O_2)$ measured by the glider sensor, the sensor-related oxygen engineering parameters TCPhase and CalPhase were used. A mean τ of 10 seconds was applied to correct measurements for the sensor

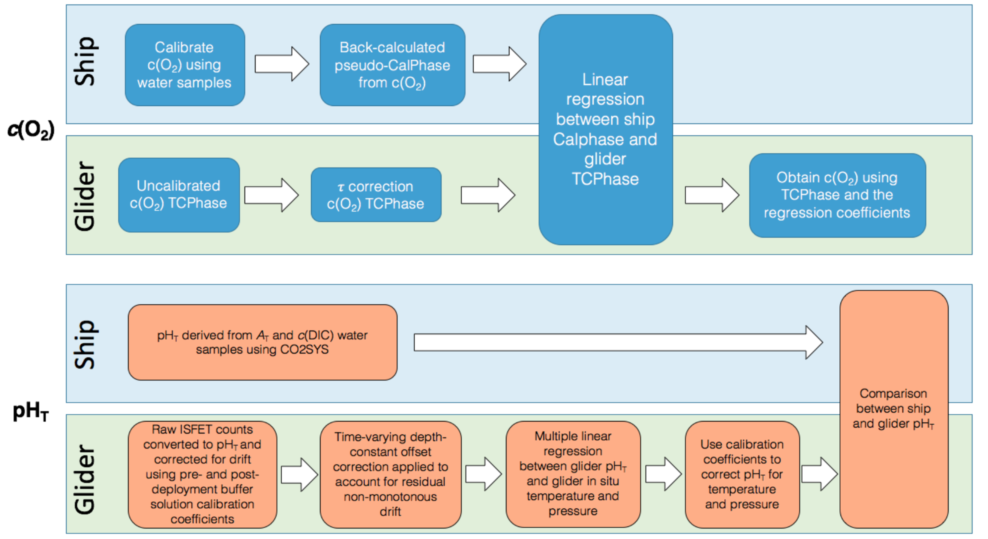

Figure 3.3: A schematic diagram showing the stages of calibrating glider dissolved oxygen concentrations ($c(\mathrm{O_2})$), and $\mathrm{pH_T}$, using ship water samples and sensor measurements.

time lag. This mean τ value was determined from the lowest root mean square difference between descending and ascending TCPhase profiles shifted in time by values of τ ranging from 0 to 50 seconds. After correcting the glider TCPhase for mean τ, the relationship between the ship sensor pseudo-CalPhase measured on March 7 and on April 16, and the glider TCPhase measured between March 8 and March 9, and between April 3 and April 4 was determined (Fig. 3.2a). The ship sensor pseudo-CalPhase was calculated using the manufacturer's set of equations normally used to obtain $c(\mathrm{O_2})$ from TCPhase and CalPhase. The slope and offset coefficients obtained from the relationship between the glider TCPhase over the entire deployment time period and ship sensor pseudo-CalPhase on March 7 and April 16 (Fig. 3.2a) were linearly interpolated over the duration of the deployment. The interpolated coefficients were matched with glider measurements in time, and used to correct all glider CalPhase profiles obtained during the deployment, allowing a calibration of glider $c(\mathrm{O_2})$ (Fig. 3.4b). Glider $c(\mathrm{O_2})$ obtained below 800 m where temperature and salinity were relatively constant in time (standard deviations of 0.05 °C and 0.01, respectively) decreased on average by $0.100 \pm 0.005\,\mathrm{mmol\,m^{-3}\,d^{-1}}$, with a total average decrease of $2.80 \pm 0.15\,\mathrm{mmol\,m^{-3}}$ over the deployment time period. As the nominal accuracy of the glider $c(\mathrm{O_2})$ sensor is around $8\,\mathrm{mmol\,m^{-3}}$ (Aanderaa, 2016), $c(\mathrm{O_2})$ were not corrected for drift.

The deployment offered a second opportunity to trial two experimental ion-sensitive field-effect transistor (ISFET) pH-$p(\mathrm{CO_2})$ sensors, previously tested on an underwater glider in the Sardinian Sea during the REP14 - MED experiment (Hemming et al., 2017; Onken et al., 2018). The ISFET pH-$p(\mathrm{CO_2})$ sensors are non-commercial custom-built sensors developed by a working group led by Kiminori Shitashima at the Tokyo University of Marine Science and Technology, Japan. They measure ocean pH, which is a function of

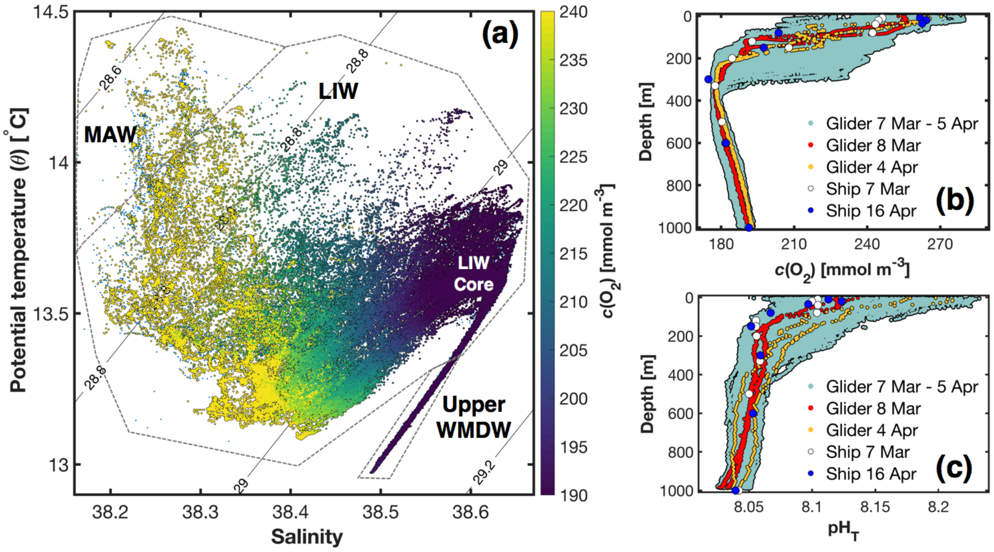

Figure 3.4: (a) Potential temperature versus salinity superimposed onto potential density contours using glider measurements between March 7 and April 5. Modified Atlantic Water (MAW), Levantine Intermediate Water (LIW), and upper Western Mediterranean Deep Water (WMDW) are labelled following Knoll et al. (2017). (b) Glider calibrated dissolved oxygen concentrations ($c(\mathrm{O_2})$) obtained during the whole campaign (grey), on March 8 (red), on April 16 (yellow), and the ship Winkler samples collected on March 7 (white), and on April 16 (blue). (c) Glider ISFET $\mathrm{pH_T}$ with drift, offset, temperature and pressure corrections applied for the whole campaign (grey), on March 8 (red), on April 4 (yellow), and the ship $\mathrm{pH_T}$ samples collected on March 7 (white) and on April 16 (blue).

hydrogen ($\mathrm{H^+}$) ion activity in the water, using the interface potential between a reference chlorine electrode (Cl-ISE) and a semiconducting ion sensing transistor. The sensor design, mechanism, performance, and previous calibrations, are described by Hemming et al. (2017).

One ISFET pH-$p(\mathrm{CO_2})$ sensor was stand-alone, meaning measurements were logged and stored by the sensor and retrieved after the deployment, and one sensor was integrated into the glider electronics allowing measurements to be sent remotely by satellite in near-realtime. Both the stand-alone and integrated sensors were positioned on the underside of the glider to limit the effect of sunlight on measurements, and backup batteries were provided to supply power in between sampling, as recommended by Hemming et al. (2017).

The ISFET pH-$p(\mathrm{CO_2})$ sensors were placed in a bucket of locally-collected northwestern Mediterranean surface seawater for a period of 9 to 10 hours before deployment. Pre-deployment conditioning is recommended for some weeks (Bresnahan et al., 2014; Takeshita et al., 2014), but this was not possible due to the time constraints of the deployment. Sensor output counts were converted to pH on the total scale ($\mathrm{pH_T}$) using 2-aminopyridine (AMP) and 2-amino-2-hydroxymethy-1, 3-propanediol (TRIS) buffer solutions, with a pre-determined $\mathrm{pH_T}$ of 6.79 and 8.09, respectively, when temperature is

25° C (see SOP 6a by Dickson et al. (2007)). The two-point calibration using counts from the integrated sensor and the corresponding buffer solution pH_T at ambient temperature was undertaken before and after the deployment. Unfortunately the stand-alone sensor ceased operating at approximately 07:00 CET on March 10 because of an issue with its power supply. For this reason, pH_T obtained by the stand-alone sensor was not used.

Comparing pH_T measurements obtained by the ISFET sensor with pH_T calculated from ship measurements both during the deployment and between 1998 and 2013 at the DyFAMed site (data available from http://mistrals.sedoo.fr/), indicated problems in accuracy and stability (Fig. 3.5b). The pH_T of the integrated sensor drifted within a range of 0.8 over the course of the 29 day deployment, with a depth-dependent minimum-maximum range in pH_T of around 1.14. pH_T from the integrated sensor were corrected for drift using the ISFET raw counts against buffer solution calibration coefficients obtained before and after the deployment. After correcting the integrated sensor measurements for drift, the range of pH_T was reduced to about 0.3 (Fig. 3.5b). However, this pH_T range of 0.3 is 5 to 6 times greater than the range of historical values of pH_T derived from discrete water samples of $c(\mathrm{DIC})$ and A_T collected in March intermittently between 1998 and 2013 at the DyFAMed site (Fig. 3.5b). This difference in range cannot be explained by the resolution of the ISFET sensor, even if some *in situ* pH sensors at specific locations can observe large variability (Hofmann et al., 2011), because the spread of the historical values between 1998 and 2013 is much smaller. Furthermore, potential temperature, salinity, and $c(O_2)$ did not co-vary with pH_T at depths greater than 400 m (typical $r^2 < 0.1$) indicating that the range in pH_T was not related to physical or biological variability. This comparison indicated that pH_T measured by the ISFET sensor required further correcting. The methods used for correcting pH_T obtained by the integrated ISFET sensor followed those implemented by Hemming et al. (2017), which is displayed schematically in Fig. 3.3. Multi-directional residual drift (i.e. non-linear, depth-independent drift) remained after correcting ISFET pH_T for linear drift using pH buffer solutions before and after deployment (Fig. 3.5a). This multi-directional residual drift was similar in time at depths between 500 m and 1000 m. It is not known exactly why this multi-directional drift remained after first correcting the pH_T for linear drift, although it is possible that the sensor's poor performance was related to the limited pre-deployment conditioning. Pre-conditioning an ISFET pH sensor prior to deployment in local seawater limits the effect of bromide on sensor performance (Takeshita et al., 2014). pH sensor voltages relative to reference electrodes can exhibit an asymptotic drift when first in contact with seawater, although, such drifts typically last just a few days (Bresnahan et al., 2014). pH_T obtained by the integrated sensor was corrected for multi-directional residual drift using Eq. (3.1), calculating the difference in pH_T between measurements obtained by the glider, and measurements obtained by ship at a depth of 500 m where the vertical density gradient was weak.

$$\mathrm{pH}_{\mathrm{T,offset}} = \mathrm{pH}_{\mathrm{T,ship}}(500\,\mathrm{m}) - \mathrm{pH}_{\mathrm{T,glider}}(500\,\mathrm{m}) \tag{3.1}$$

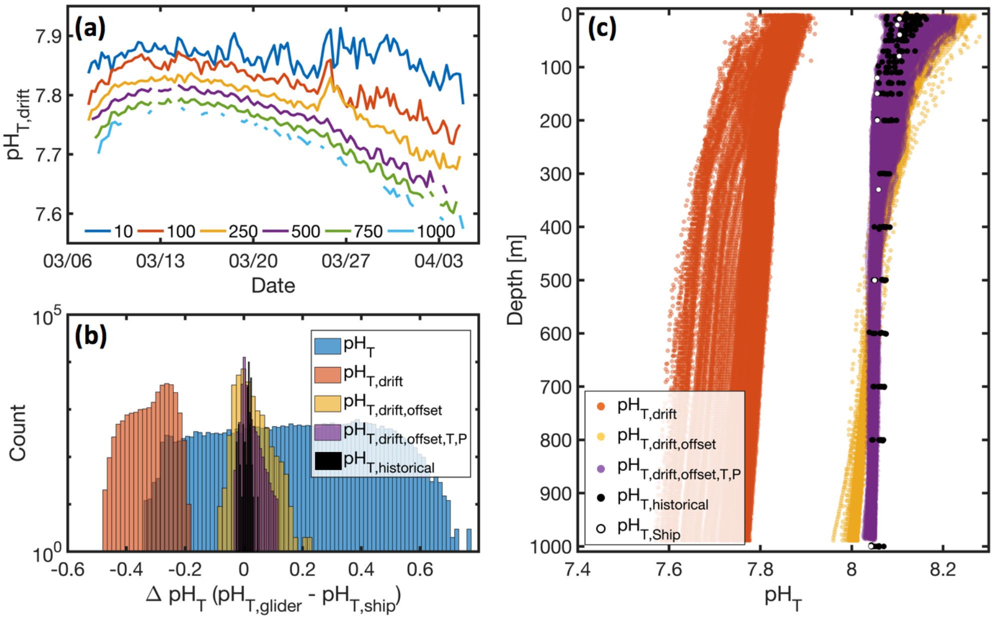

Figure 3.5: (a) Glider pH_T corrected for linear drift as a function of time at six different depths (metres). (b) Histograms of $\Delta\mathrm{pH}_\mathrm{T}$ (difference between ship pH_T and glider pH_T) at all depths after different stages of calibration: no corrections (‘pH_T’, blue), linear drift correction only using pH buffer solutions before and after deployment (‘$\mathrm{pH}_{\mathrm{T,drift}}$’, orange), after the linear drift and 500 m offset correction (‘$\mathrm{pH}_{\mathrm{T,drift,offset}}$’, yellow), and with all corrections including for temperature and pressure (‘$\mathrm{pH}_{\mathrm{T,drift,offset,T,P}}$’, purple). Historical $\Delta\mathrm{pH}_\mathrm{T}$ (black) collected in March from six years between 1998 and 2013 is shown for comparison. Historical $\Delta\mathrm{pH}_\mathrm{T}$ counts are scaled by 500 to be visualised on the same axis as glider $\Delta\mathrm{pH}_\mathrm{T}$. (c) Glider pH_T at the same correctional stages described in the caption for panel (b), historical pH_T collected in March from six years between 1998 and 2013, and pH_T collected by ship in March 2016.

This method assumes that the ship pH_T at 500 m is always the same throughout the 29 day deployment. The offsets were added to the full-depth glider pH_T profiles. This offset correction shifted pH_T by 0.23 to 0.43 (depending on the timing of the dive) closer to the expected range of pH_T defined using ship measurements (Fig. 3.5b,c). The calculated offsets varied non-linearly with time, and were unrelated to variations in *in situ* temperature, salinity, and $c(\mathrm{O}_2)$. After correcting pH_T for linear and multi-direction depth-independent drift, pH_T was corrected for *in situ* temperature and pressure using linear regression, as ISFET sensors are sensitive to changes in temperature and pressure (Hemming et al., 2017; Johnson et al., 2016). The differences between glider pH_T collected during the deployment and ship pH_T collected on March 7 and on April 16 were regressed separately against glider temperature and pressure. The regression coefficients using the ship pH_T on March 7 and on April 16 were interpolated over the 29 day deployment, and were matched in time with glider measurements. The range of glider pH_T

after correcting for linear and multi-directional depth-independent drift, temperature, and pressure was closer to pH_T derived from ship samples during the deployment, and close to the range of historical observations (Fig. 3.5b,c). The calibration equations using ship pH_T on March 7 and on April 16 in this study were similar to that used by Hemming et al. (2017), with temperature and pressure slopes of similar magnitude, and a root mean square error of less than 0.02 (Table 3.1). Calibrated glider pH_T obtained on March 8 agreed relatively well (mostly within 0.01) with ship pH_T obtained on March 7 (Fig. 3.4c). This is also true when comparing glider pH_T on April 4 and ship pH_T on April 16, but only for depths greater than 300 m. At depths shallower than 300 m, a difference of up to 0.12 can be seen in places. These differences relate to glider profiles collected on or after March 25, corresponding with increased temperature and $c(O_2)$, particularly in the euphotic layer (Fig. 3.6). Using a stoichiometric O_2:C ratio of -1.45, relating C to pH using CO2SYS, and experimenting with temperature, indicated that a pH_T change of < 0.02 could be expected at the surface as a result of biological activity and physical changes. As this pH_T change is roughly 6 times lower than that observed by the glider, it seemed the large differences between glider pH_T and ship pH_T within the top 300 m on or after March 25 are erroneous. Although the empirical corrections based on temperature and pressure appear to be sufficient for the majority of measurements, it is possible that the pH_T after March 25 suffered from artefacts due to the correction procedure, or that the underlying raw measurements were poor.

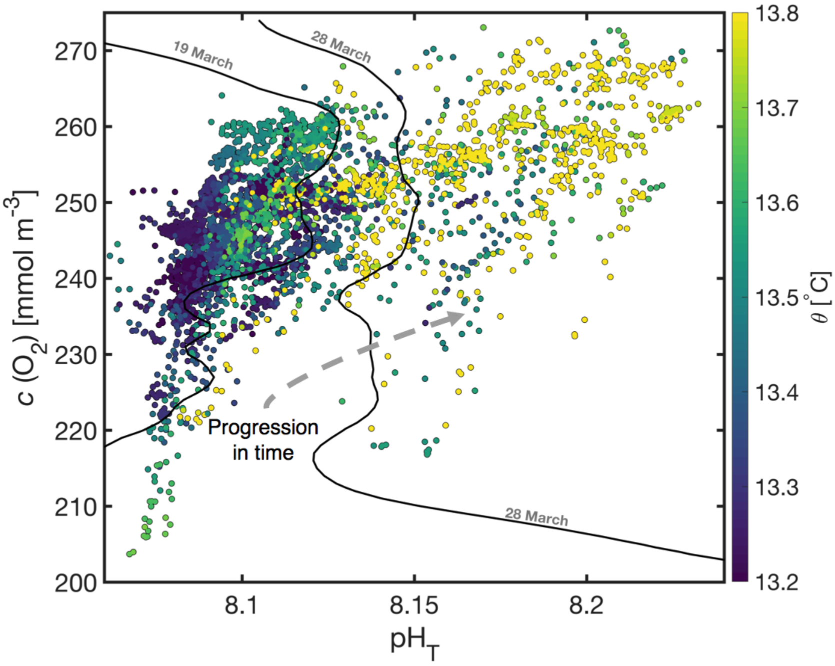

Figure 3.6: pH_T against dissolved oxygen concentrations ($c(O_2)$), coloured by potential temperature (θ) for all points within the mean euphotic layer (46 m) between March 7 and April 5. Approximate date contours are superimposed.

3.3.4 Deriving Parameters Using CO2SYS

The CO2SYS programme (Van Heuven et al., 2011) was used to derive $\mathrm{pH_T}$ for validating glider ISFET $\mathrm{pH_T}$, using ship measurements of $c(\mathrm{DIC})$, A_T, *in situ* temperature, salinity, pressure, and nutrients $\mathrm{Si(OH)_4^-}$ and $\mathrm{PO_4^{3-}}$. Equilibrium constants published by Mehrbach et al. (1973) and refitted by Dickson and Millero (1987) were used, as recommended by previous Mediterranean-based studies (Álvarez et al., 2014; Key et al., 2010). $c(\mathrm{DIC})$ and A_T had an error of 3.5 $\mu\mathrm{mol\,kg^{-1}}$ and 3.2 $\mu\mathrm{mol\,kg^{-1}}$, respectively, determined from CRM measurements, representing a combined mean error in derived $\mathrm{pH_T}$ of 0.008. This mean error was calculated as the mean of the absolute differences in $\mathrm{pH_T}$ derived using single values of $c(\mathrm{DIC})$ and A_T with their margins of error (e.g. for $c(\mathrm{DIC})$, $2320 \pm 3.5\ \mu\mathrm{mol\,kg^{-1}}$). The sulphate acid dissociation constant and total borate concentration described by Dickson (1990) and Uppström (1974), respectively, were used for the calculation.

The A_T - S relationship was determined using 56 ship measurements of A_T and salinity obtained close to BOUSSOLE at 5 m and 10 m depth between 2013 and 2015, and had a predicted standard deviation of 4.4 $\mu\mathrm{mol\,kg^{-1}}$, and an r^2 of 0.89 (Merlivat et al., 2018). Calibrated glider ISFET $\mathrm{pH_T}$, and A_T derived using Eq. (3.2) were used to derive glider $f(\mathrm{CO_2})$ and $c(\mathrm{DIC})$.

$$A_{\mathrm{T,glider}}\ /\ \mu\mathrm{mol\,kg^{-1}} = \mathrm{S_{glider}}\ 87.647 - 785.5 \tag{3.2}$$

The equilibrium constants, the sulphate acid dissociation constant, and the total borate concentration used for ship measurements were also used for the calculation of $f(\mathrm{CO_2})$ and $c(\mathrm{DIC})$ using glider measurements to 1000 m depth. The mean errors of derived $f(\mathrm{CO_2})$ and $c(\mathrm{DIC})$ were 23.5 µatm and 9.2 $\mu\mathrm{mol\,kg^{-1}}$, respectively, calculated as the mean of the absolute differences of $f(\mathrm{CO_2})$, and $c(\mathrm{DIC})$ derived using single values of A_T and pH (including the margin of error associated with the A_T - S relationship, and $\mathrm{pH_T}$ temperature and pressure corrections, respectively). The absolute mean difference between ship and glider $c(\mathrm{DIC})$ and A_T was 2.2 $\mu\mathrm{mol\,kg^{-1}}$ and 0.7 $\mu\mathrm{mol\,kg^{-1}}$, respectively, when taking into account measurements obtained between the surface and 1000 m depth. CO2SYS and the constants used in these calculations are described in more detail by Orr et al. (2015). Similarly to the BOUSSOLE buoy measurements, $f(\mathrm{CO_2})$ derived using ship and glider measurements were normalised to 13°C ($f_{13}(\mathrm{CO_2})$) to remove thermal effects using glider *in situ* temperature and the expression described by Takahashi et al. (1993). $f_{13}(\mathrm{CO_2})$ is used for discussion or display purposes only.

To obtain $c(\mathrm{DIC})$ at the BOUSSOLE biogeochemical buoy using CO2SYS, observed $f(\mathrm{CO_2})$ at 3 m was used alongside derived A_T calculated using salinity at 10 m and Eq. (3.2). The mean error of derived $c(\mathrm{DIC})$ was 5.5 $\mu\mathrm{mol\,kg^{-1}}$, calculated as the mean of the

Table 3.1: A comparison of derived calibration equations used for correcting glider pH_T obtained by the integrated ISFET sensor for *in situ* temperature (t) and pressure (p), with the corresponding r^2 of the fit using the difference between ship and glider pH_T and t, and p, the root mean square errors (RSME), and the 95 % confidence boundaries for the temperature coefficient (c_t), pressure coefficient (c_p), and y-axis offset (c_{offset}).

Deployment	**Equation**	**r^2**	**RMSE**	**95 % coef.**
DyFAMed (Mar 7 2016)	$pH_{T,tpc} = pH_T - 0.017\ t/°C + 5.2 \times 10^{-5}\ p/dbar + 0.21$	0.65	0.009	$-0.019 < c_t < -0.016$ $5.1 \times 10^{-5} < c_p < 5.4 \times 10^{-5}$ $0.19 < c_{offset} < 0.24$
DyFAMed (Apr 16 2016)	$pH_{T,tpc} = pH_T - 0.012\ t/°C + 8.6 \times 10^{-5}\ p/dbar + 0.11$	0.69	0.018	$-0.012 < c_t < -0.011$ $8.6 \times 10^{-5} < c_p < 8.7 \times 10^{-5}$ $0.10 < c_{offset} < 0.12$
REP14 - MED 2014 (Hemming et al., 2017)	$pH_{T,tpc} = pH_T - 0.021\ t/°C + 4.5 \times 10^{-5}\ p/dbar + 0.26$	$t = 0.66$, $p = 0.42$	$t = 0.02$, $p = 0.015$	$-0.022 < c_t < -0.020$ $4.2 \times 10^{-5} < c_p < 4.9 \times 10^{-5}$ $0.25 < c_{offset} < 0.28$

absolute differences in derived c(DIC), using a single value of A_T including the margin of error associated with the A_T - S relationship (4.4 µmol kg^{-1}), and constant f(CO_2). The absolute difference between the ship c(DIC) on March 7 at 10 m depth and average c(DIC) measured by the buoy on the same day at 10 m depth was 6.6 µmol kg^{-1}.

3.4 Capturing the Spring Bloom

The spring bloom is characterised by a decrease of surface f_{13}(CO_2) due to photosynthesis. Its initiation varies inter-annually at the DyFAMed site (e.g. in April 2013, in March 2014), and usually occurs after a period of deep mixing (Merlivat et al., 2018). Deploying the glider in March-April 2016 complemented measurements obtained by the buoy sensors at the surface at a time when the spring bloom was expected to occur.

SST measured by the buoy remained relatively stable between March 7 and March 19 whilst surface f_{13}(CO_2) increased by 40 µatm (Fig. 3.7a), and surface salinity increased by 0.13 (Fig.7b). The higher f_{13}(CO_2), higher salinity waters were likely transported upwards via wind-induced (Fig. 3.7a) deep mixing and increased convection. These waters originate from 50 to 150 m depth where high salinity, high f_{13}(CO_2) Levantine Intermediate Water (LIW) exists (Fig. 3.4a). SST increased by up to 0.6 °C between

March 19 and March 20, and continued to increase intermittently to a maximum of 14.3 °C on April 5 (total increase of 1 °C over the deployment period). Whilst SST increased between March 19 and April 1, $f_{13}(CO_2)$ decreased by 85 μatm. This was the start of the spring bloom, corresponding with increased surface $c(O_2)$, pH_T, and optical backscatter (Fig. 3.7b). $c(O_2)$ is a by-product of photosynthesis, and the pH_T increase results from changes in the consumption of CO_2 altering the carbonate equilibria (Cornwall et al., 2013; Copin-Montégut and Bégovic, 2002), and changes in temperature. Optical backscatter measurements are related to variations in particulate organic matter, mineral particles, and gas bubbles (Stramski et al., 2004). Therefore an increase in $c(O_2)$, pH_T, and backscatter suggests an increase in primary productivity between March 19 and April 1. A clear relationship between potential temperature (θ), $c(O_2)$, and pH_T existed within the euphotic layer (z_{eu}) (Fig. 3.6, Fig. 3.8), with higher potential temperature associated with higher pH_T and $c(O_2)$. The increase in potential temperature here represents a shift from deep mixing to surface stratification resulting from calmer meteorological conditions, (e.g. after March 25, Fig. 3.7a), enhancing light supply and stability, causing productivity to increase (Sverdrup, 1953; Pingree et al., 1977). This productivity increased $c(O_2)$ and optical backscatter, and indirectly pH_T (Fig. 3.7b, Fig. 3.8c,d,e). As a result of increased photosynthesis, surface waters became super-saturated in $c(O_2)$ by March 27 (Fig. 3.7b).

Nutrient concentrations obtained by ship for depths of 10 m to 90 m on March 7 were generally highest at 90 m where there is increased remineralisation, and lowest at the surface where there is increased utilisation by phytoplankton (Fig. 3.9a). Clear differences can be seen in nutrient samples obtained before and after the spring bloom (Fig. 3.9b). Combined NO_3^- and NO_2^- decreased by roughly 7 mmol m^{-3}, $Si(OH)_4$ by roughly 2.5 mmol m^{-3}, and PO_4^{3-} by roughly 0.22 mmol m^{-3} at 30 m depth, associated with biological production during the spring bloom period. A deep chlorophyll maximum is often found around this depth, where reduced light availability is compromised for gains in nutrient supply (Estrada, 1996). At 70 m and 90 m depth, nutrients did not vary much between March and April, while there was a significant decrease in $c(O_2)$ and a small change in potential temperature (Fig. 3.9c). This corresponded to increased stratification with a stronger potential temperature gradient within the top 70 m (Fig. 3.9c). The minimum depth of the oxicline, defined as the depth range where oxygen decreases the most as a function of depth, shoaled by 45 m, changing from 80 m in March to 35 m in April, caused by calmer meteorological conditions. This provided the sharp decrease of $c(O_2)$ at 70 m depth. As photosynthesis was confined to more stratified waters above, and light did not penetrate this far down, nutrients at 70 m were not utilised, and $c(O_2)$ decreased likely due to respiration.

3.5 Estimating N Using $c(\mathrm{O_2})$

3.5.1 $c(\mathrm{O_2})$ budget

Changes in $c(\mathrm{O_2})$ are related to biological processes, such as photosynthesis, and respiration, and physical processes, such as air-sea exchange, mixing, and advection. N quantified using net biologically produced $c(\mathrm{O_2})$ ($N_{\mathrm{O_2}}$), can be estimated by removing the portion of $c(\mathrm{O_2})$ related to physical processes from the overall changes in $c(\mathrm{O_2})$. The method described by Alkire et al. (2014) was used to estimate $N_{\mathrm{O_2}}$ using mass budgets of glider $c(\mathrm{O_2})$:

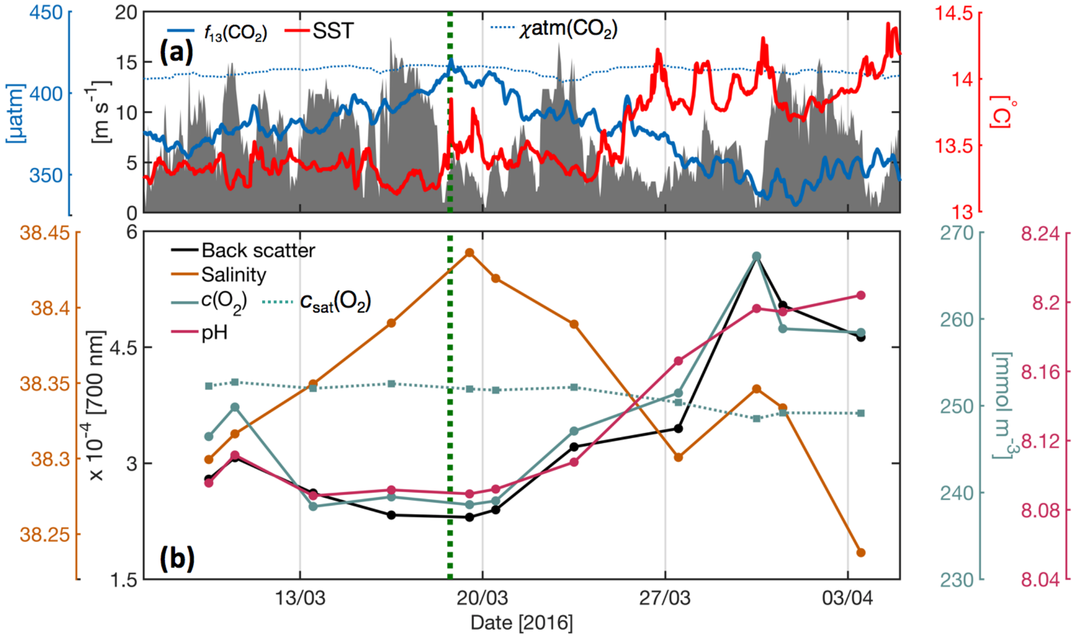

Figure 3.7: (a) Wind speed at 10 m above sea level at the meteorological buoy (dark grey shading), sea surface temperature (red), and the fugacity of $\mathrm{CO_2}$ normalised to 13 °C (blue) obtained at 10 m depth at the BOUSSOLE buoy between March 7 and April 5. The partial pressure of atmospheric $\mathrm{CO_2}$ in March 2016 (dotted blue, µatm) taken from Lampedusa, Italy is shown (https://www.esrl.noaa.gov/gmd/dv/data/index.php, converted from $\mu\mathrm{mol\,mol^{-1}}$ using sea level pressure measured by the meteorological buoy). The timing of the approximate start of the spring bloom (dashed green), determined using buoy $f(\mathrm{CO_2})$ measurements, is plotted for comparison.(b) Glider measurements of salinity (orange), optical backscatter at 700 nm (black), dissolved oxygen concentrations ($c(\mathrm{O_2})$) (turquoise), and calibrated $\mathrm{pH_T}$ (pink) binned at 10 m for the same time period as in (a). The oxygen concentration at saturation (dashed turquoise) calculated using the algorithms described by Garcia and Gordon (1992), and the timing of the approximate start of the spring bloom (dashed green), determined using buoy $f(\mathrm{CO_2})$ measurements, are plotted for comparison.

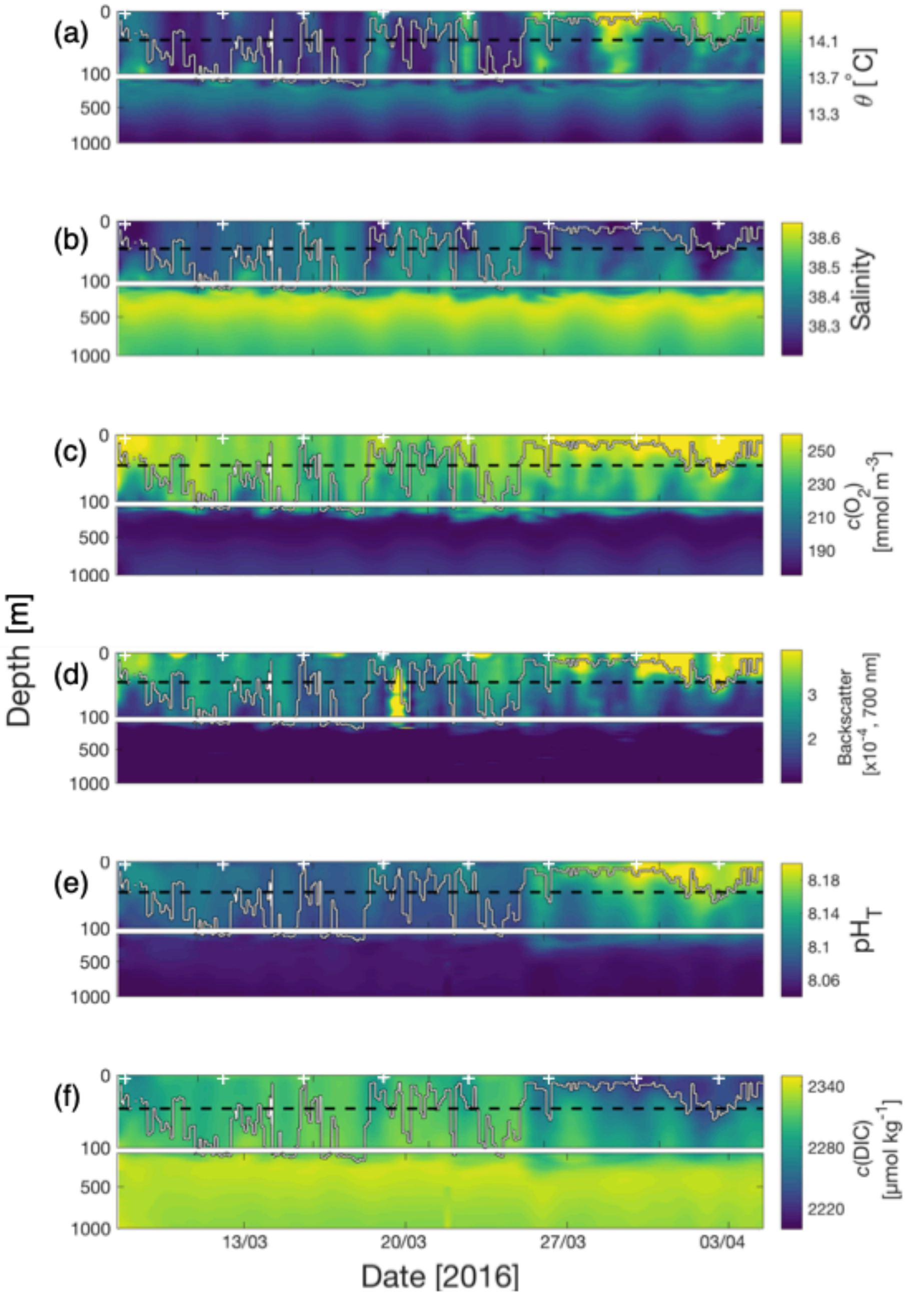

Figure 3.8: Glider (a) potential temperature (θ), (b) salinity, (c) dissolved oxygen concentrations ($c(\mathrm{O_2})$), (d) optical backscatter, (e) $\mathrm{pH_T}$, and (f) dissolved inorganic carbon concentrations ($c(\mathrm{DIC})$) retrieved between March 7 and April 5. To produce these fields, optimal interpolation was used with a radius of influence of 1 day x 10 m depth. The mean euphotic depth used for net community production (N) estimates (black dashed line) and mixed layer depths (white line) estimated using the algorithm described by Holte and Talley (2009) are superimposed on top of the optimally interpolated fields. White crosses displayed at 5 m in each panel represent the most northernly point along the glider path.

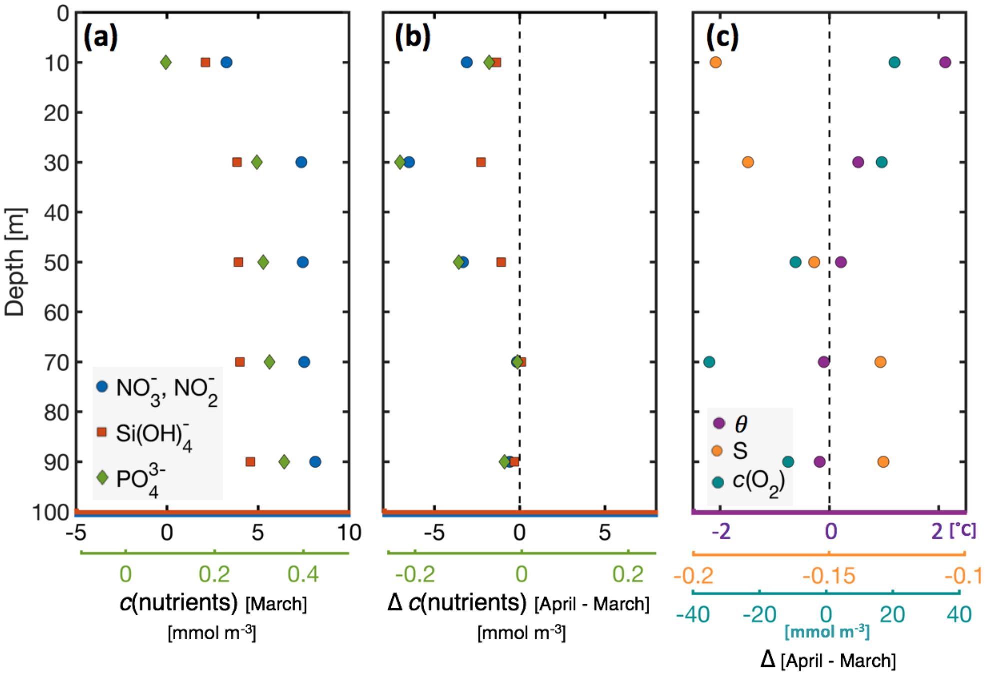

Figure 3.9: (a) Combined nutrients NO_3^- and NO_2^- (blue circle), $Si(OH)_4$ (red square), and PO_4^{3-} (green diamond) obtained by ship on March 7. (b) The calculated difference (Δ) between these three nutrients before (March 7) and after (April 16) the start of the spring bloom. In both (a) and (b), the same x-axis limits are used for NO_3^- and NO_2^-, and $Si(OH)_4$, and the green x-axis corresponds to PO_4^{3-}. (c) The calculated difference (Δ) of potential temperature (θ) (purple circle, °C), salinity (S) (orange circle), and dissolved oxygen concentrations ($c(O_2)$) (turquoise circle, mmol m^{-3}) measured by the ship sensor between March 7 and April 16.

$$\int_{Z_{\mathrm{eu}}}^{0} \left(\frac{\partial\, c(\mathrm{O_2})}{\partial t} + u\frac{\partial\, c(\mathrm{O_2})}{\partial x} + v\frac{\partial\, c(\mathrm{O_2})}{\partial y}\right)\mathrm{d}z = -F_{\mathrm{ASE}} + N_{\mathrm{O_2}} + F_{\mathrm{ENT}} \tag{3.3}$$

$$N_{\mathrm{O_2}} = \frac{\partial I}{\partial t} + F_{\mathrm{ADV}} + F_{\mathrm{ASE}} - F_{\mathrm{ENT}} \tag{3.4}$$

where z_{eu} is the mean depth of the euphotic layer (46 ± 7 m) estimated using all the glider profiles and the method described by Lee et al. (2007), which was well-mixed on average, u and v are zonal and meridional velocities, respectively, $\frac{\partial I}{\partial t}$ is O_2 inventory change over time, F_{ADV} is horizontal advection, F_{ASE} is the air-sea flux of O_2, and F_{ENT} is entrained $c(O_2)$ due to mixed layer deepening.

The glider measured $c(O_2)$ within an Eulerian framework, consistently sampling geographic locations over time, measuring the (not necessarily instantaneous) local time rate of change of $c(O_2)$. Contrary to a Lagrangian framework, estimates of F_{ADV} are needed to complete the budget. However, because the glider surveyed the domain at relatively slow speed (35 ± 11 cm $\mathrm{s^{-1}}$), it was possible that specific patterns in $c(\mathrm{O_2})$ transiting at different speeds to the glider (e.g. moving fronts, internal tides) were repeatedly sampled in time and space along the glider path. This would complicate the F_{ADV} estimate, as plane-fits were used to obtain horizontal $c(\mathrm{O_2})$ gradients across the entire domain (explained in Sect. 3.5.4) (Alkire et al., 2014). To include the entire domain, measurements obtained over ≥ 4 days were required, as this was the time that it took the glider to complete a diamond pattern (Fig. 3.1). It was therefore important to determine whether the glider resolved spatial and temporal variability on this timescale within the survey region.

3.5.2 Variability in Time and Space

Twelve-hour-binned mean $c(\mathrm{O_2})$ values were calculated throughout the deployment period (Fig. 3.10), using measurements within z_{eu} at the outer most points of the glider survey domain: west (7.63 - 7.70° E, 43.35 - 43.40° N), east (7.95 - 8.00° E, 43.35 - 43.40° N), south (7.80 - 7.85° E, 43.23 - 43.30° N), and north (7.80 - 7.85° E, 43.45 - 43.50° N). Although some spatial contrasts in mean $c(\mathrm{O_2})$ can be seen at similar times at different locations, such as between the southern most point and the three remaining outer points around March 17, a consistent temporal pattern can be seen over the glider survey domain. For example, a decrease in $c(\mathrm{O_2})$ was observed between March 7 and March 17, followed by an increase in $c(\mathrm{O_2})$ between March 17 and April 1 across the domain. These consistent temporal patterns using mean $c(\mathrm{O_2})$ from across the domain suggest relative spatial homogeneity.

The glider completed a diamond circuit in roughly 4 days, with each of the four sides forming the diamond survey pattern taking around 24 h to complete. Twelve-hour-binned mean $c(\mathrm{O_2})$ at the four outer points of the diamond followed the observed 4 day trend relatively well (Fig. 3.10), suggesting that the glider captured domain-wide spatial variability well on this timescale. Therefore calculating $N_{\mathrm{O_2}}$ over the entire glider survey domain using a moving time window of 4 days (i.e. using measurements within day n ± 2 days) was deemed appropriate. Changes in $N_{\mathrm{O_2}}$ on this 4 day timescale, and the fluxes required to estimate $N_{\mathrm{O_2}}$, were assumed to represent changes over the entire glider survey domain.

3.5.3 $\mathrm{O_2}$ Inventory Change

Daily mean $c(\mathrm{O_2})$ values were calculated using all glider measurements obtained in the top 46 m (z_{eu}) and within the moving 4 day window. $\frac{\partial I}{\partial t}$ was calculated by multiplying the differences in daily mean $c(\mathrm{O_2})$ within z_{eu} by z_{eu}:

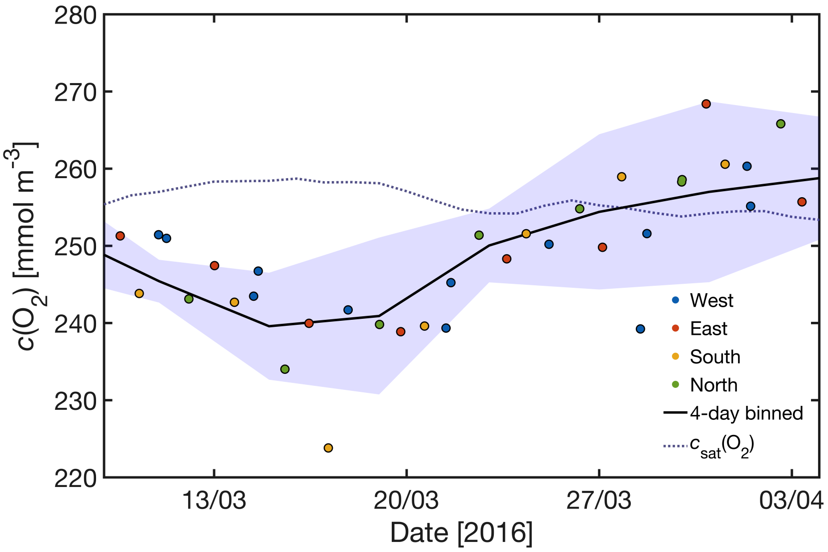

Figure 3.10: Mean dissolved oxygen concentration ($c(O_2)$) within the mean euphotic layer from the glider at the most western (blue circle, 7.63 - 7.70° E, 43.35 - 43.40° N), eastern (red circle, 7.95 - 80° E, 43.35 - 43.40° N), southern (yellow circle, 7.80 - 7.85° E, 43.23 - 43.30° N), and northern (green circle, 7.80 - 7.85° E, 43.45 - 43.50° N) points of the survey domain. The 4 day binned $c(O_2)$ mean with standard deviation range calculated using all $c(O_2)$ within the BOUSSOLE domain for the top 46 m is also shown (black line and light blue area). Daily oxygen saturation at the surface ($c_{sat}(O_2)$, dashed blue line) calculated using all temperature and salinity measurements (Garcia and Gordon, 1992) within the BOUSSOLE domain for the top 46 m smoothed using an n ± 2 day window is displayed for reference.

$$\frac{\partial I}{\partial t} = \int_{Z_{eu}}^{0} \frac{\partial c(O_2)}{\partial t} \partial z \tag{3.5}$$

The time period chosen spanned 25 days between March 10 and April 4, and included 121 individual dives (upcasts and downcasts) spanning the entire survey domain. The mean daily $c(O_2)$ inventory change throughout the domain was (13 ± 264) mmol m^{-2} d^{-1}. The mean error was calculated using the spatial standard deviations of $c(O_2)$ within z_{eu} at the beginning and at the end of the 25 day period.

3.5.4 Advection

Advection was calculated following the method used by Alkire et al. (2014) using zonal and meridional mean horizontal gradients of $c(O_2)$ and current velocity within z_{eu} using a moving time window of 4 days. For this method, the mean horizontal $c(O_2)$ gradients across the domain are assumed mostly related to physics, however it is possible that biological processes may have affected the gradients at some times. Mean horizontal $c(O_2)$ gradients were calculated using plane-fits:

$$c(\mathrm{O_2}, z_{\mathrm{eu}}, x, y) = \frac{\partial\, c(\mathrm{O_2})}{\partial x} + \frac{\partial\, c(\mathrm{O_2})}{\partial y} = ax + by + c \tag{3.6}$$

where a and b are the slopes in the zonal and meridional directions respectively, c is the offset, and x and y are cartesian coordinates calculated using the relative distance between the longitude and latitude, respectively, of each individual $c(\mathrm{O_2})$ data point within z_{eu} and a constant geographic location southwest of the survey domain within the 4 day time window. As an example, the plane-fit used to obtain $c(\mathrm{O_2}, z_{\mathrm{eu}}, x, y)$ within a 4 day time window centred on March 25 is shown in Fig. 3.11b.

To check that the method of fitting planes to obtain $c(\mathrm{O_2}, z_{\mathrm{eu}}, x, y)$ was working correctly, horizontal gradients were estimated using median $c(\mathrm{O_2})$ at the four outer corners of the diamond survey pattern. These across-domain gradients were determined using measurements outside four geographic thresholds: north (> 43.43° N), south (< 43.3° N), east (> 7.93° E), and west (< 7.73° E) within the 4 day time windows. The general pattern in time of $c(\mathrm{O_2}, z_{\mathrm{eu}}, x)$ and $c(\mathrm{O_2}, z_{\mathrm{eu}}, y)$ determined using the across-domain and plane-fit methods were similar (Fig. 3.12a,b), although differences of up to $0.5\,\mathrm{mmol\,m^{-3}\,km^{-1}}$ were seen between plane-fit and across-domain gradients at certain times (e.g. March 29).

Estimating absolute geostrophic currents within the survey domain involved four steps. First, the dynamic height anomaly (Ψ) was calculated relative to the surface for 121 dive profiles using 10 m depth binned profiles (max. depth of 1000 m) of glider absolute salinity, conservative temperature, and pressure (Roquet et al., 2015). Second, the horizontal Ψ gradients were estimated daily with a 4 day moving time window for each individual 10 m depth bin using the plane-fit method:

$$\Psi(\mathrm{bin}, x, y) = \frac{\partial \Psi}{\partial x} + \frac{\partial \Psi}{\partial y} = ax + by + c \tag{3.7}$$

A visual example of fitting planes to Ψ within a 4 day time window centred on March 25 can be seen in Fig. 3.11a. Two binned mean Ψ profiles for the chosen time period; one profile including the meridional gradients as a function of depth, and the other including the zonal gradients as a function of depth, were calculated using the depth-varying daily plane-fits. Third, two binned mean relative geostrophic velocity profiles (zonal and meridional) were calculated using the two binned mean Ψ profiles by vertically integrating the thermal wind equation, and using the Coriolis parameter f. Last, the calculated mean geostrophic shear was referenced to the 4 day window glider dive averaged currents (DACs) to obtain absolute geostrophic shear. The glider DACs (Fig. 3.13) represent the mean current velocity throughout the water column (typically 0 - 1000 m) surveyed by the glider over the course of a dive, which is estimated using the glider actual location and the modelled dead-reckoned location at the end of a dive relative to the dive starting location (Eriksen et al., 2001). Mean profiles of u_{DAC} and v_{DAC} calculated using the 4 day moving time window were used. This is to ensure that current velocities are estimated on the same time scale as $c(\text{O}_2)$ horizontal gradients. The process of referencing relative geostrophic velocity profiles to DACs is visualised in Fig. 3.11c. u_{abs} and v_{abs} profiles were averaged for z_{eu} to obtain 4 day mean velocities for the layer of interest. Surface absolute u and v velocities, and current speed (averaged for the top 10 m) calculated using glider measurements agreed relatively well at some points with surface absolute velocities, and speed derived using AVISO sea level anomalies (Fig. 3.12c-e). This was particularly true between March 10 and March 14, and between March 25 and March 29. However, differences of up to 15 cm s^{-1} can be seen at certain time periods (e.g. March 16). Differences in velocities partially result from the difference in resolution, and the differences in location between the glider measurements and the AVISO product.

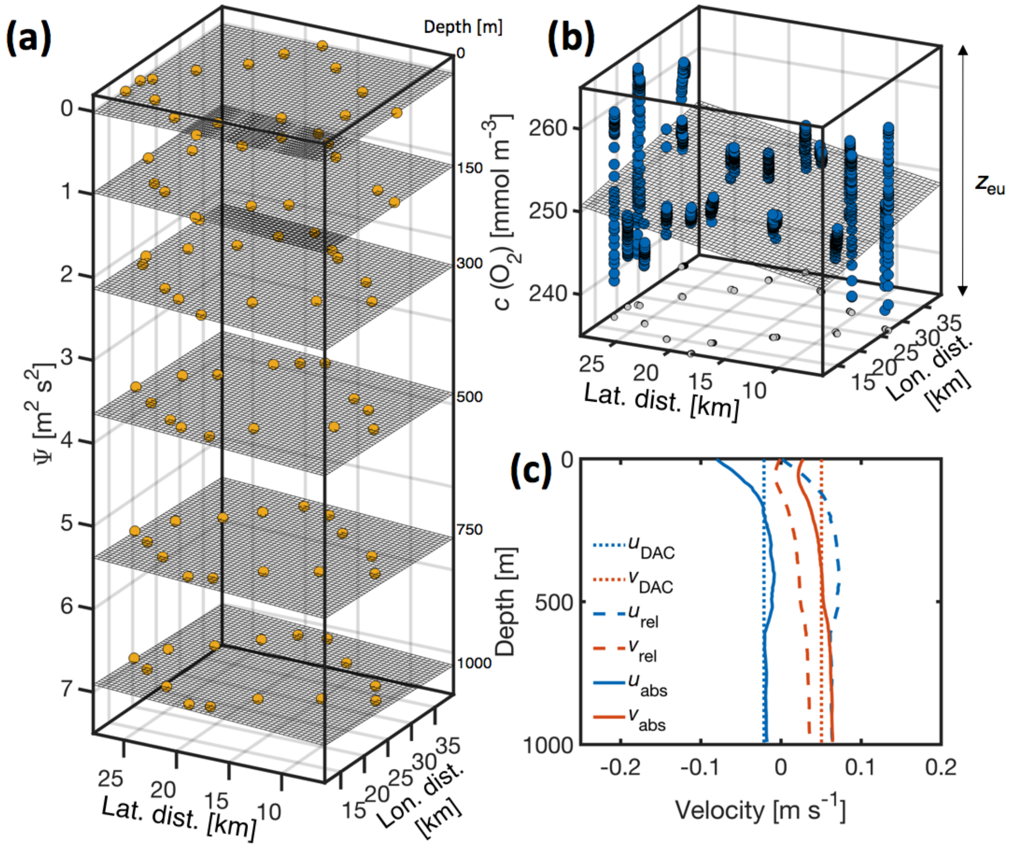

Figure 3.11: (a) Plane-fits of binned geopotential anomalies (ψ) at six depths: surface, 150 m, 300 m 500 m 750 m and 1000 m. (b) Plane-fit of dissolved oxygen concentrations ($c(\text{O}_2)$) within the euphotic depth (z_{eu}). The grey markers identify the locations of the blue $c(\text{O}_2)$) points. (c) Approximately 5-10 m vertically smoothed relative (dashed line) and absolute (filled line) geostrophic zonal (u) and meridional (v) velocities. Dive-averaged currents (DACs, dotted line) are displayed for reference. Data shown in (a)-(c) are for March 25.

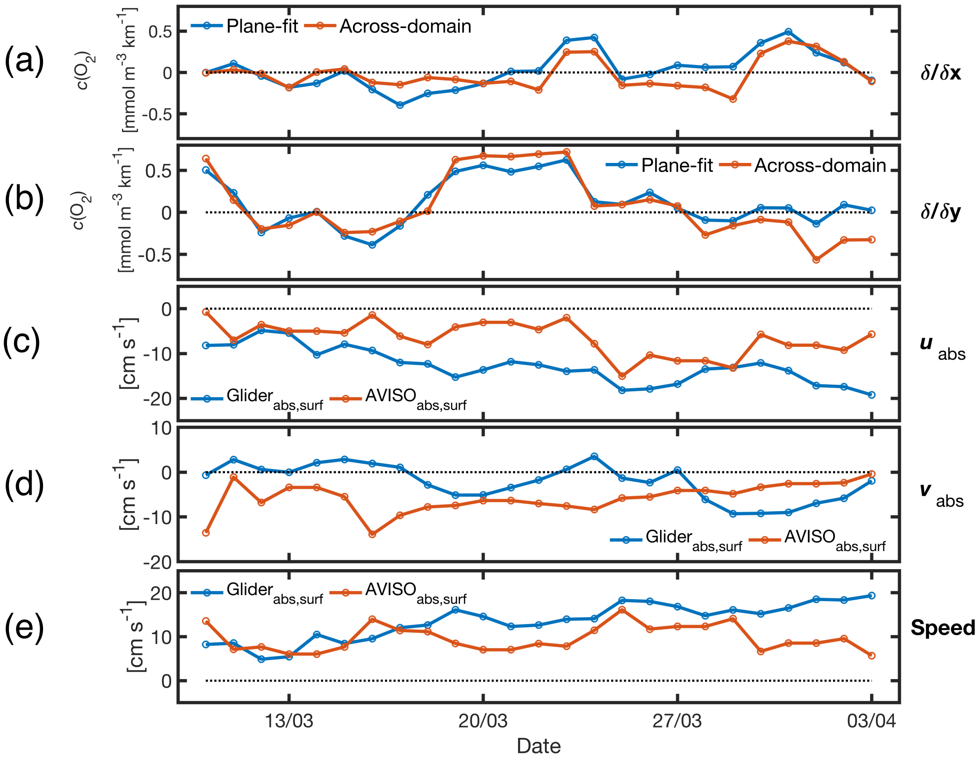

Figure 3.12: (a) Zonal and (b) meridional horizontal $c(O_2)$ gradients calculated using the plane-fit (blue) and across-domain (red) methods. (c) Absolute mean *u* velocity, (d) *v* velocity, and (e) current speed calculated using glider measurements in the top 10 m of the water column (blue), and absolute mean current speed derived from reprocessed (L4) satellite AVISO daily sea level information (red), downloaded from the Copernicus Marine Environment Monitoring Service (http://marine.copernicus.eu/services-portfolio/access-to-products).

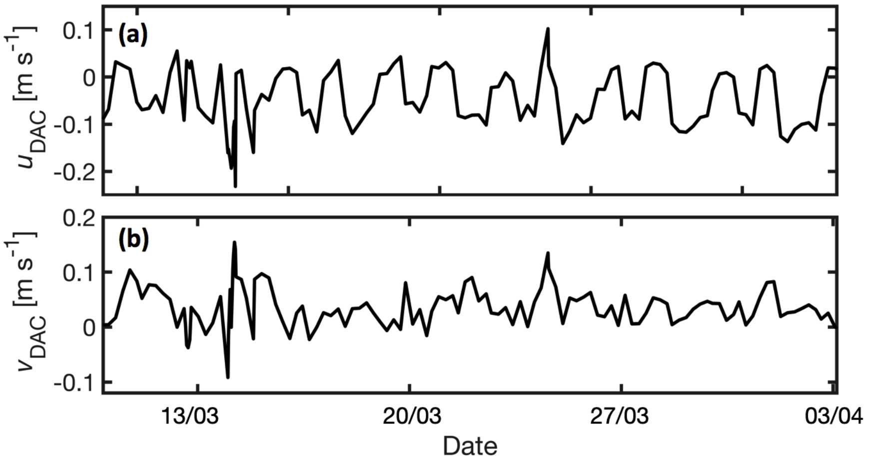

Figure 3.13: Glider (a) zonal and (b) meridional dive-averaged currents (DAC) between March 10 and April 4.

The advective flux (F_{ADV}) was calculated by multiplying the absolute geostrophic velocities with the $c(\mathrm{O_2})$ horizontal gradients:

$$F_{\mathrm{ADV}} = u\frac{\partial\, c(\mathrm{O_2})}{\partial x} + v\frac{\partial\, c(\mathrm{O_2})}{\partial y} \tag{3.8}$$

The mean daily F_{ADV} over the 25 day time period was (-27 ± 120) mmol m^{-2} d^{-1}. The mean error was calculated taking into account errors associated with the calculated velocities and $c(\mathrm{O_2})$ horizontal gradients. Comparing this low estimate of advection on a 25 day timescale with significant short term advection, such as on March 17 (Fig. 3.13), suggests the importance of considering advection when calculating N on time scales of less than a month.

3.5.5 Air-Sea Gas Exchange

To calculate the air-sea exchange component required to estimate $N_{\mathrm{g,O_2}}$ (‘g’ for glider), $c(\mathrm{O_2})$, salinity, and *in situ* temperature at the surface, and wind speed at 10 m above sea level at the Azur meteorological buoy (Fig. 3.1) were used:

$$F_{\mathrm{ASE}} = k_{\mathrm{O_2}}\,(\,c_{\mathrm{surf}}(\mathrm{O_2}) - c_{\mathrm{sat}}(\mathrm{O_2}) \times (1 + \Delta)\,) \tag{3.9}$$

$$\Delta = 1 + (\,0.01\,(\,\mathrm{W_{10}}\,/\,9\,\mathrm{m\,s^{-1}}\,)^2\,) \tag{3.10}$$

where $k_{\mathrm{O_2}}$ is the gas transfer velocity. $c_{\mathrm{surf}}(\mathrm{O_2})$ is the mean oxygen concentration in the top 10 m. $c_{\mathrm{sat}}(\mathrm{O_2})$ is the oxygen saturation concentration derived using algorithms described by Garcia and Gordon (1992) using salinity, *in situ* temperature, and *in situ* atmospheric pressure. Δ represents the effect of bubble injection on $c_{\mathrm{sat}}(\mathrm{O_2})$ woolf1991bubbles. $\mathrm{W_{10}}$ is the wind speed at 10 m above sea level. The Schmidt number, required to calculate $k_{\mathrm{O_2}}$, was calculated using the expression for $\mathrm{O_2}$ described by Wanninkhof (2014). Equation 3.10 follows Woolf and Thorpe (1991), where 9 m s^{-1} represents the wind speed at which the oxygen saturation is 101 %. Negative F_{ASE} represents an influx of $\mathrm{O_2}$ from the atmosphere to the ocean when $c_{\mathrm{sat}}(\mathrm{O_2})$ multiplied by (1 + Δ) is higher than $c_{\mathrm{surf}}(\mathrm{O_2})$. All parameters used for the F_{ASE} calculation were mean values using a moving 4 day time window, similar to F_{ADV} and $\frac{\partial I}{\partial t}$ calculations (Fig. A2). The mean daily F_{ASE} over the 25 day time period was (-25 ± 17) mmol m^{-2} d^{-1}. The mean error was calculated taking into account the 20 % uncertainty associated with $k_{\mathrm{O_2}}$ (Wanninkhof, 2014), and uncertainty associated with the $c(\mathrm{O_2})$ calibration.

3.5.6 Entrainment

When the mixed layer deepens to depths greater than z_{eu}, water from below with different $c(O_2)$ mixes with water within the layer. As a result, there is either a reduction or an increase in mean $c(O_2)$ within z_{eu} depending on the vertical distribution of $c(O_2)$. To account for this, F_{ENT} was estimated following the method described by Binetti (2016):

$$F_{ENT} = \frac{c_I(O_2, t_1, z_{mixed}(t_2)) \times (\frac{z_{eu}}{z_{mixed}(t_2)}) - c_I(O_2, t_1, z_{eu})}{t_2 - t_1} \tag{3.11}$$

where t_2-t_1 represents the change in time, z_{mixed} is the depth of the mixed layer, $c_I(O_2, t_1, z_{mixed}(t_2))$ is the mean $c(O_2)$ within z_{eu} at t_1 multiplied by z_{mixed} at t_2, and $c_I(O_2, t_1, z_{eu})$ is equal to the mean $c(O_2)$ within z_{eu} at t_1. z_{mixed} was calculated using mixed layer depths for glider dives estimated using the algorithm described by Holte and Talley (2009), which models the general shape of a profile, searches for physical features, and compares estimates using traditional threshold and gradient methods. Similar to previous N_{g,O_2} budget components, z_{mixed}, and $c(O_2)$ used in this calculation were mean values over a 4 day moving time window. F_{ENT} was calculated on 5 days only when z_{mixed} was deeper than z_{eu} at the beginning of the time period. The mean F_{ENT} flux was (-4 ± 46) mmol m^{-2} d^{-1} averaging over the 25 day period. The mean error was calculated taking into account the difference in spread of $c(O_2)$ at t_1 within $z_{mixed}(t_2)$, and $c(O_2)$ at t_1 within z_{eu}.

3.5.7 Net Community Production (N_{g,O_2})

Glider N_{O_2} (N_{g,O_2}) was negative for roughly two thirds of the time period (Fig. 3.14), indicating net respiration. A removal of $c(O_2)$ from z_{eu} of up to -275 mmol O_2 m^{-2} d^{-1} was seen on March 30. N_{g,O_2} was negative during most of the time period due to ingassing resulting from $c(O_2)$ undersaturation and high mean wind speeds, and high advection, with both processes providing additional O_2 to the water column via physics, rather than biological processes. N_{g,O_2} was positive on March 16, March 21, March 24 to 28, March 31, and April 2 to 3. A maximum addition of roughly 200 mmol O_2 m^{-2} d^{-1} was seen on March 16. The F_{ASE} and F_{ADV} absolute values decreased close to zero between March 24 and March 29. This indicated that a larger proportion of oxygen inventory change was related to N_{g,O_2}. F_{ASE} was positive, and therefore outgassing, during the period of oxygen supersaturation beginning on March 27 (Fig. 3.7b). When considering that near-surface c(DIC) started decreasing at the BOUSSOLE biogeochemical buoy after March 19 (Fig. 3.7a), it could be expected that N_{g,O_2} would start increasing at around the same time due to a shift from net respiration to net photosynthesis. However, as $F_{ADV} < 0$, more $c(O_2)$ was entering the domain than leaving, resulting in lower N_{g,O_2}.

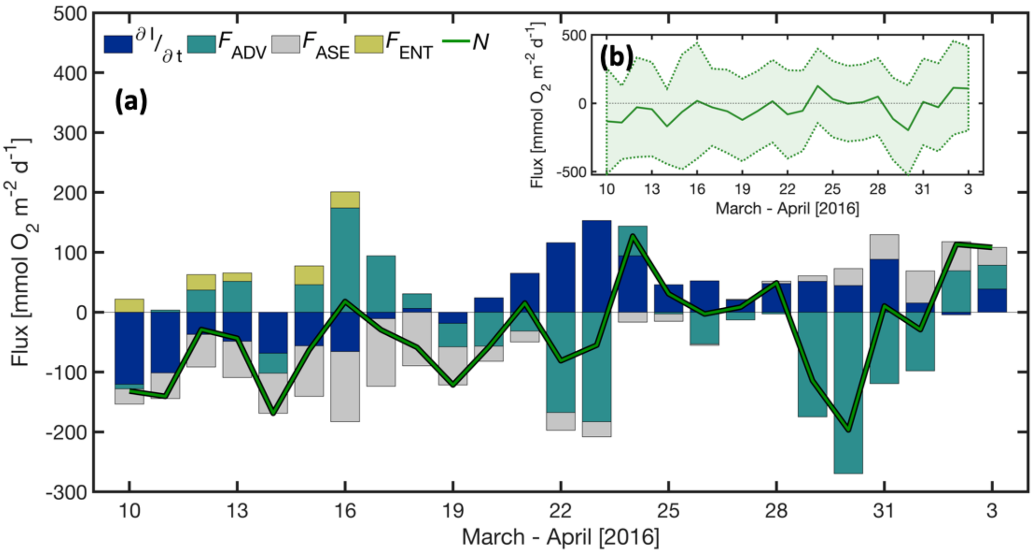

Figure 3.14: (a) Oxygen inventory change ($\frac{\partial I}{\partial t}$, dark blue), advection (F_{ADV}, turquoise), air-sea exchange (F_{ASE}, grey), entrainment (F_{ENT}, yellow), and estimated net community production (N, green line) in the euphotic layer between March 10 and April 4. (b) Estimated N with error boundaries.

Average $N_{\mathrm{g,O_2}}$ over the 25 day time period was (-36 ± 313) mmol m^{-2} d^{-1}. The overall $N_{\mathrm{g,O_2}}$ uncertainty was large (Fig. 3.14b), which was calculated using error propagation methods combining uncertainties relating to each flux term. This 25 day mean, when ignoring the error, indicated that respiration was the dominating biological process. Using an O_2:C stoichiometric ratio of -1.45 (Hedges et al., 2002; Anderson, 1995), which assumes that nitrate was the main driver of primary production within the survey domain, a mean inorganic carbon release of (25 ± 216) mmol m^{-2} d^{-1} was estimated.

3.6 Estimating N Using c(DIC)

3.6.1 Glider $N_{\mathrm{g,DIC}}$

Similarly to $c(O_2)$, the change in c(DIC) is related to biological processes, such as photosynthesis, respiration, and calcification, and physical processes, such as air-sea exchange, mixing, and advection. N using glider c(DIC) ($N_{\mathrm{g,DIC}}$) normalised to a salinity of 38.3 was estimated, derived from calibrated glider $\mathrm{pH_T}$, and A_{T} using CO2SYS (see section 3.3.4). As discussed in Section 3.3.3, calibrated glider $\mathrm{pH_T}$ observed in the top 300 m of the water column on or after March 25 seemed to be erroneous. Measurements obtained on or after this date at these depths had stronger vertical gradients than the days before March 25 (Fig. 3.15b). Variations in temperature and $c(O_2)$ did not correlate with the decreased c(DIC), as discussed for $\mathrm{pH_T}$ in section 3.3.3. Comparing c(DIC) from the buoy, and from the glider at 10 m < 5 km away from the buoy (Fig. 3.15a) illustrated that the glider pH_T calibration was relatively good before March 25, but poor afterwards. Glider c(DIC) after March 25 was up to 70 mmol m^{-3} lower than was estimated from the buoy at the same time.

$N_{g,DIC}$ was estimated between March 10 and March 25 using Eq. (3.4), previously used for estimating N_{g,O_2}, and which is explained in more detail in section 3.5. F_{ADV}(C) was estimated using horizontal planes fitted to c(DIC) within the euphotic depth multiplied by the absolute velocities calculated in section 3.5.4. The mean differences over 25 days between horizontal gradients obtained by fitting planes and those obtained using the across-domain method (Sect. 3.5.4) in time were < 0.09 mmol m^{-3} km^{-1} (Fig. A3). F_{ASE}(C) was calculated following Eq. (3.14) described in section 3.6.1 (Fig. A4), and $\frac{\partial I(c)}{\partial t}$ and F_{ENT}(C) were calculated using the methods described in sections 3.5.3 and 3.5.6, respectively. All parameters used for estimating $N_{g,DIC}$ were averaged using the same 4 day moving time window used to estimate N_{g,O_2}. Contrary to the calculation of N_{g,O_2}, negative $N_{g,DIC}$ represented net photosynthesis, whilst positive $N_{g,DIC}$ represented net respiration.

The sign of $N_{g,DIC}$ has been switched for comparison with N_{g,O_2}. $N_{g,DIC}$ was negative (positive in Fig. 3.16) between March 10 and March 15, indicating net respiration, and positive (negative in Fig. 3.16) from March 16 onwards, indicating net photosynthesis. During this time, $\frac{\partial I(C)}{\partial t}$ decreased to -230 mmol m^{-2} d^{-1}, and absolute F_{ADV}(C) fluxes were at times > 300 mmol m^{-2} d^{-1} (e.g. March 24).

The mean $N_{g,DIC}$ was (115 ± 1188) mmol m^{-2} d^{-1} over the time period, indicating net photosynthesis. The mean fluxes of F_{ADV}(C), F_{ASE}(C), and F_{Ent}(C) were (-78 ± 290) mmol m^{-2} d^{-1}, (-6 ± 4) mmol m^{-2} d^{-1}, and (3 ± 96) mmol m^{-2} d^{-1}, respectively. The effects of air-sea exchange were small, but the effects of advection were large. $N_{g,DIC}$ estimates for specific time periods are compared with N_{g,O_2}, and $N_{b,DIC}$ in Table 3.2.

3.6.2 $N_{b,DIC}$

During the daytime, photosynthesis, respiration, and air-sea exchange are the main processes affecting c(DIC) close to the surface. A warm layer of low c(DIC) water forms here, a result of higher temperatures and biological production. At nighttime, convection mixes colder high c(DIC) waters below with the formed warmer low c(DIC) waters above. Comparing the change in c(DIC) at nighttime, and particularly during the early hours of the morning when a daily maximum in c(DIC) should be expected, over a given time period is equal to N after accounting for non-biological processes. This N represents the difference between gross community production and metabolic CO_2 release within the mixed layer. Net community production using buoy c(DIC) ($N_{b,DIC}$) was calculated using

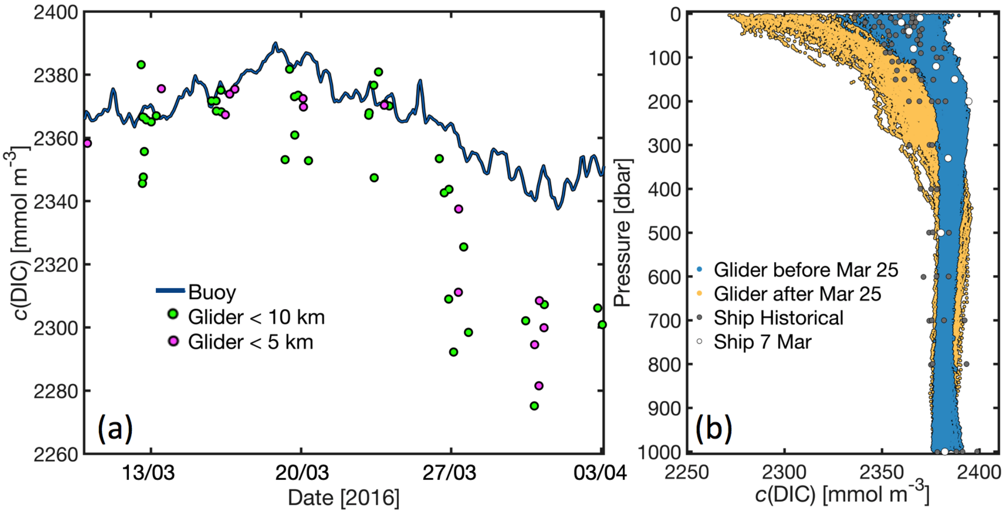

Figure 3.15: (a) Hourly *c*(DIC) estimated at a depth of 10 m at the buoy (dark blue), and estimated by the glider at 10 m < 10 km (green), and < 5 km (pink) away from the buoy. (b) Glider *c*(DIC) from the entire deployment period, before (blue) and after (yellow) March 25. Historical ship *c*(DIC) observed intermittently in March between 1998 and 2013 is shown alongside the ship samples retrieved on March 7, 2016. All *c*(DIC) shown in this figure are normalised to a salinity of 38.3.

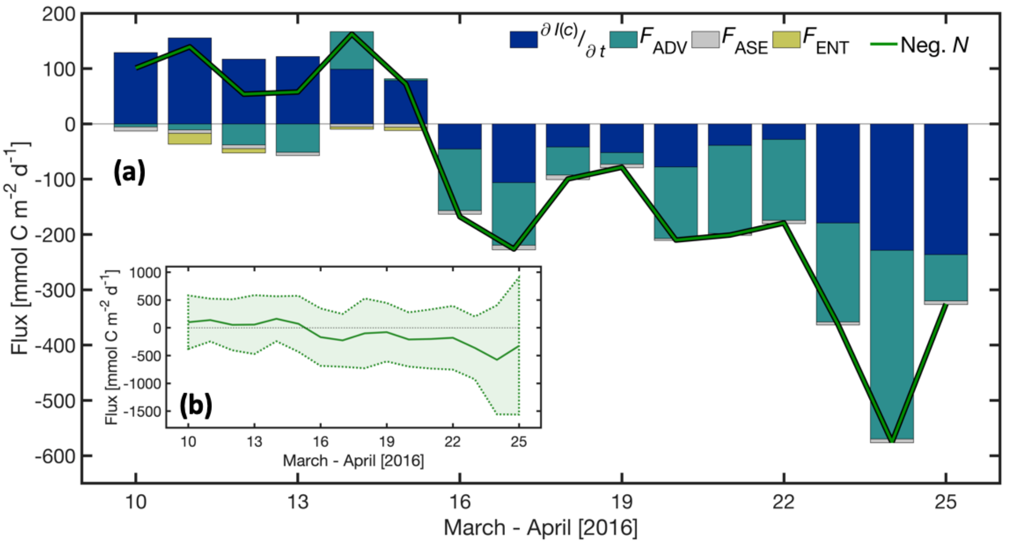

Figure 3.16: (a) Glider dissolved inorganic carbon (*c*(DIC)) inventory change ($\frac{\partial I(c)}{\partial t}$, dark blue), advection (F_{ADV}, turquoise), air-sea exchange (F_{ASE}, grey), entrainment (F_{ENT}, yellow), and estimated negative net community production (N, green line) in the euphotic layer between March 10 and March 25. (b) Estimated N with error boundaries.

Eq. (3.12):

$$- N_{\mathrm{b,DIC}} = \frac{\partial C}{\partial t} + F_{\mathrm{ASE}}(C) \tag{3.12}$$

$$\frac{\partial C}{\partial t} = \int \frac{\partial I(\mathrm{c})}{\partial t} \partial z \; \rho \tag{3.13}$$

where ρ is seawater density (kg m^{-3}), ∂z is the euphotic depth, $\frac{\partial I(\mathrm{C})}{\partial t}$ is the c(DIC) change (µmol kg^{-1}) over time using consecutive maxima (Fig. 3.15), and F_{ASE} is the air-sea exchange of CO_2 (mmol m^{-2} d^{-1}), negative when there is an ingassing of CO_2 from the atmosphere to the ocean.

This method using buoy measurements assumes that calcification, entrainment, and advection have a negligible effect. However, it has been shown using glider $c(O_2)$ and c(DIC) that advection in the region of the BOUSSOLE site can at times be significant (Fig. 3.14 and 3.16). Therefore, $N_{\mathrm{b,DIC}}$ has been estimated excluding and including an advection flux (F_{ADV}). The average glider c(DIC) F_{ADV} calculated using daily F_{ADV} during the time periods chosen to estimate $N_{\mathrm{b,DIC}}$ was added to the result of Eq. (3.12).

$N_{\mathrm{b,DIC}}$ was calculated from c(DIC) derived using CO2SYS, A_{T} derived from salinity, and measured $f(CO_2)$ (see Section 3.3.4) obtained at the BOUSSOLE biogeochemical buoy close to the surface. Changes in local precipitation and evaporation were considered and their effects removed by normalising c(DIC) to a salinity of 38.3 (Bates et al., 2005; Friis et al., 2003), which was the mean salinity in the euphotic depth between March 10 and April 3. This normalisation decreased c(DIC) at the buoy on average by 14 µmol kg^{-1}. c(DIC) measurements obtained between 04:00 and 07:00 local time only were used, when daily maxima were expected. Changes in salinity at the surface are likely related to advection and/or entrainment, as salinity is not significantly affected by photosynthesis or respiration. $N_{\mathrm{b,DIC}}$ was estimated during time periods when there were signs of limited advection and/or vertical mixing. Although, when considering $c(O_2)$ advection across the wider BOUSSOLE glider domain, this was not true. Two time periods were chosen (Fig. 3.17 and Table 3.2), when the average standard deviation of salinity was < 0.014. z_{eu} was chosen to be consistent with the calculation of $N_{\mathrm{g,O_2}}$. Linear regression was used to obtain slope coefficients for c(DIC) in time for the two different time periods, representing $\frac{\partial I(\mathrm{C})}{\partial t}$ (Fig. 3.17). F_{ASE}(C) was estimated as follows:

$$F_{\mathrm{ASE}}(\mathrm{C}) = k_{\mathrm{CO_2}} \; \alpha \; (\, f(\mathrm{CO_2}) - \chi_{\mathrm{atm}}(\mathrm{CO_2}) \;\; p_{\mathrm{atm}} \,) \tag{3.14}$$

where $k_{\mathrm{CO_2}}$ is the gas transfer velocity of CO_2, α is the solubility constant according to

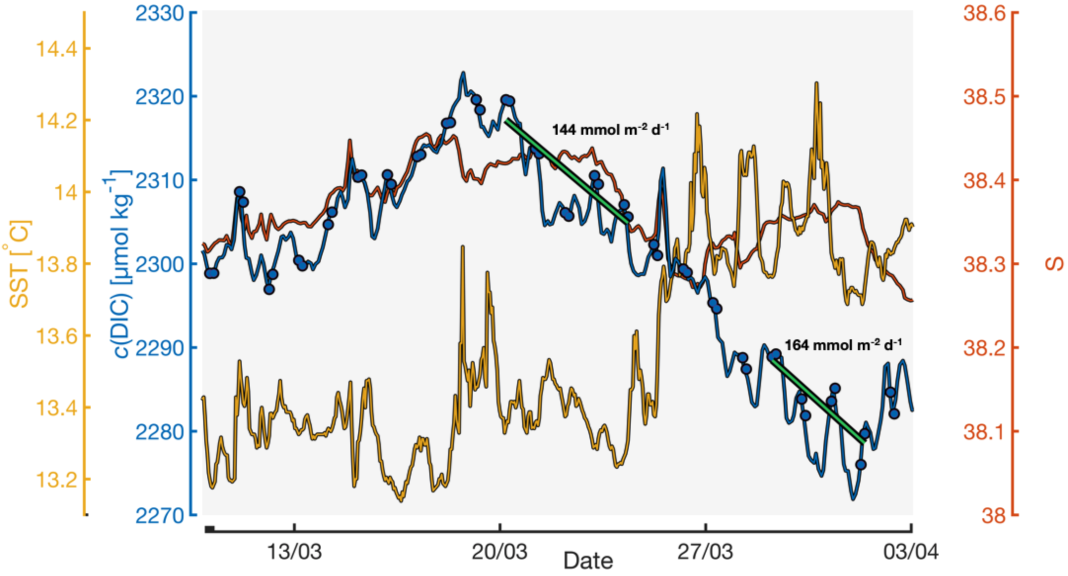

Figure 3.17: Sea surface temperature (SST, orange), salinity (S, red), and dissolved inorganic carbon concentration normalised to a salinity of 38.3 (c(DIC), blue) observed close to the surface at the BOUSSOLE biogeochemical buoy. The calculated net community production estimates ($N_{\mathrm{b,DIC}}$) are written, corresponding to the change in c(DIC) over time ($\frac{\partial I(\mathrm{C})}{\partial t}$, green lines) for two time periods.

Weiss (1974), $\chi_{\mathrm{atm}}(\mathrm{CO_2})$ is the mole fraction of atmospheric CO_2 obtained by flask air-sample collection at Lampedusa, Italy in March 2016 (downloaded from ftp://aftp.cmdl.noaa.gov/data/trace_gases/co2), and p_{atm} is sea level pressure measured by the Meteorology buoy. The Schmidt number, required to calculate $k_{\mathrm{CO_2}}$, was calculated using the expression for CO_2 described by Wanninkhof (2014).

$N_{\mathrm{b,DIC}}$ estimates are summarised in Table 3.2. $N_{\mathrm{b,DIC}}$ was 144 mmol m^{-2} d^{-1} (including F_{ADV}, 317 mmol m^{-2} d^{-1}) between March 20 and March 25, and 164 mmol m^{-2} d^{-1} (including F_{ADV}, 196 mmol m^{-2} d^{-1}) between March 28 and April 1.

3.7 Uncertainty

Each of the fluxes used to calculate N had some degree of uncertainty (Table 3.3). When combined, the total uncertainty was large for $N_{\mathrm{g,O_2}}$ (Fig. 3.14b), $N_{\mathrm{g,DIC}}$ (3.16b), and $N_{\mathrm{b,DIC}}$ (Table 3.3). The largest sources of error were associated with the inventory change and advection fluxes. These fluxes depend somewhat on the assumption that concentrations were homogenous across the glider survey domain. Although general patterns over time were relatively consistent across the domain (Fig. 3.10), there were at times differences of up to 20 mmol m^{-2} d^{-1} (e.g. between the southern- and western-most points of the domain on March 16). This suggests that the domain was at times dynamic. Therefore the spatial standard deviations of the glider concentrations and the glider dive-averaged currents for a given time step, used to derive errors in inventory change and advection, respectively, and when integrated over the euphotic layer (46 m), were responsible for a large proportion of overall uncertainty. In future, this uncertainty might be reduced if more gliders are deployed, decreasing the time-length of the moving window used to calculate N.

3.8 N in the Northwestern Mediterranean Sea

In this study, the mean $N_{\mathrm{O_2}}$ flux estimated between March 10 and March 27 using glider $c(\mathrm{O_2})$ measurements was $(-44 \pm 316)\,\mathrm{mmol\,m^{-2}\,d^{-1}}$. The mean $N_{\mathrm{O_2}}$ flux estimated between March 10 and March 27 using glider $c(\mathrm{DIC})$ was $(133 \pm 605)\,\mathrm{mmol\,m^{-2}\,d^{-1}}$, whilst the average $N_{\mathrm{O_2}}$ fluxes estimated using buoy $c(\mathrm{DIC})$ including advection at 10 m depth between March 20 and March 25, and between March 29 and April 1, were $(460 \pm 870)\,\mathrm{mmol\,m^{-2}\,d^{-1}}$, and $(284 \pm 927)\,\mathrm{mmol\,m^{-2}\,d^{-1}}$, respectively (Table 3.2). The mean N fluxes estimated using $c(\mathrm{DIC})$ suggest net photosynthesis, whilst the mean N fluxes estimated using $c(\mathrm{O_2})$ suggest net respiration, which is unlikely in spring.

Mean $N_{\mathrm{O_2}}$ fluxes estimated in this study were compared with estimates in other studies in the northwestern Mediterranean Sea using different methods and time periods. Coppola et al. (2018) estimated annual $N_{\mathrm{O_2}}$ at the DyFAMed site using excess $\mathrm{O_2}$ above 100 % saturation over a period of 20 years, assuming that the depth of 100 % saturation corresponded to the compensation depth (the depth where gross primary production minus total community respiration is equal to zero). Net annual production was estimated as the difference between the minimum and maximum oxygen inventory between the surface and the depth of 100 % saturation, divided by the number of days in between, and multiplied by 365 days. Annual $N_{\mathrm{O_2}}$ was calculated by removing the net air-sea flux from the net annual production. Although the methods of estimating $N_{\mathrm{O_2}}$ in this study differed greatly from that used by Coppola et al. (2018), their estimate of $9.2\,\mathrm{mol\,m^{-2}\,a^{-1}}$ (equivalent to $25\,\mathrm{mmol\,m^{-2}\,d^{-1}}$) is within the range of $N_{\mathrm{O_2}}$ estimates presented here ($N_{\mathrm{O_2}}$ of between $-82\,\mathrm{mmol\,m^{-2}\,d^{-1}}$ to $460\,\mathrm{mmol\,m^{-2}\,d^{-1}}$).

Copin-Montégut (2000) estimated $N_{\mathrm{O_2}}$ at between $0.6\,\mathrm{mol\,m^{-2}\,a^{-1}}$ and $2.2\,\mathrm{mol\,m^{-2}\,a^{-1}}$ (equivalent of between $1.6\,\mathrm{mmol\,m^{-2}\,d^{-1}}$ and $6\,\mathrm{mmol\,m^{-2}\,d^{-1}}$) in the top 40 m of the water column at the DyFAMed biogeochemical buoy using continuous changes in $c(\mathrm{O_2})$ in May 1995 and a vertical diffusion model. The estimates published by Copin-Montégut (2000) are situated within the range of mean $N_{\mathrm{O_2}}$ fluxes estimated in this study. Mean chlorophyll and nitrate concentrations close to the surface at the DyFAMed / BOUSSOLE site in May are typically low when compared with other months (Antoine et al., 2008), hence the range of $N_{\mathrm{O_2}}$ estimated by Copin-Montégut (2000) might be considered as post-bloom.

Table 3.2: Net community production (N) estimated in this study is compared with N estimated in other studies close to stations BOUSSOLE and DyFAMed. The associated time periods, estimated mean advection fluxes (F_{ADV}), and estimated mean air-sea exchange fluxes (F_{ASE}) are also listed. N has been converted to/from carbon units using a molar stoichiometry O_2:C ratio of -1.45 (Hedges et al., 2002; Anderson, 1995). Positive N represents photosynthesis, whilst negative N represents respiration. The superscript ^{c} has been used to identify N converted to/from carbon units. The superscript ^{u} has been used to identify values that have been converted from different units (e.g. from mol m^{-2} a^{-1} to mmol m^{-2} d^{-1}).

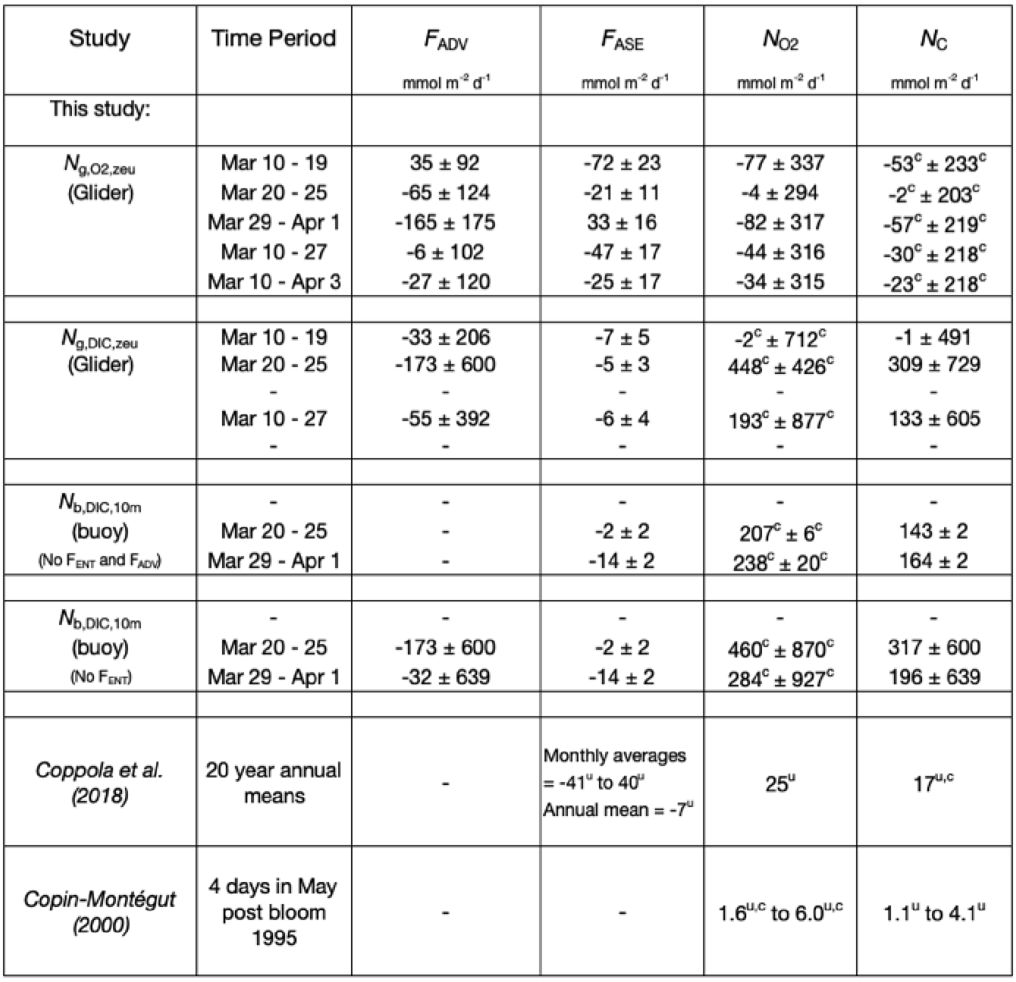

Study	Time Period	F_{ADV} mmol m^{-2} d^{-1}	F_{ASE} mmol m^{-2} d^{-1}	N_{O2} mmol m^{-2} d^{-1}	N_{C} mmol m^{-2} d^{-1}
This study:					
$N_{g,O2,zeu}$ (Glider)	Mar 10 - 19 Mar 20 - 25 Mar 29 - Apr 1 Mar 10 - 27 Mar 10 - Apr 3	35 ± 92 -65 ± 124 -165 ± 175 -6 ± 102 -27 ± 120	-72 ± 23 -21 ± 11 33 ± 16 -47 ± 17 -25 ± 17	-77 ± 337 -4 ± 294 -82 ± 317 -44 ± 316 -34 ± 315	$-53^{c} \pm 233^{c}$ $-2^{c} \pm 203^{c}$ $-57^{c} \pm 219^{c}$ $-30^{c} \pm 218^{c}$ $-23^{c} \pm 218^{c}$
$N_{g,DIC,zeu}$ (Glider)	Mar 10 - 19 Mar 20 - 25 - Mar 10 - 27 -	-33 ± 206 -173 ± 600 - -55 ± 392 -	-7 ± 5 -5 ± 3 - -6 ± 4 -	$-2^{c} \pm 712^{c}$ $448^{c} \pm 426^{c}$ - $193^{c} \pm 877^{c}$ -	-1 ± 491 309 ± 729 - 133 ± 605 -
$N_{b,DIC,10m}$ (buoy) (No F_{ENT} and F_{ADV})	- Mar 20 - 25 Mar 29 - Apr 1	- - -	- -2 ± 2 -14 ± 2	- $207^{c} \pm 6^{c}$ $238^{c} \pm 20^{c}$	- 143 ± 2 164 ± 2
$N_{b,DIC,10m}$ (buoy) (No F_{ENT})	- Mar 20 - 25 Mar 29 - Apr 1	- -173 ± 600 -32 ± 639	- -2 ± 2 -14 ± 2	- $460^{c} \pm 870^{c}$ $284^{c} \pm 927^{c}$	- 317 ± 600 196 ± 639
Coppola et al. (2018)	20 year annual means	-	Monthly averages = -41^{u} to 40^{u} Annual mean = -7^{u}	25^{u}	$17^{u,c}$
Copin-Montégut (2000)	4 days in May post bloom 1995	-	-	$1.6^{u,c}$ to $6.0^{u,c}$	1.1^{u} to 4.1^{u}

3.9 Conclusion

This study demonstrates the capability of estimating N using measurements obtained by an autonomous glider. Both $c(O_2)$ and $c(\text{DIC})$ were used to create mass budgets, taking into account physical fluxes relating to horizontal advection, air-sea exchange, and mixing. It was clear that on timescales of less than a month, physical fluxes can be significant and should not be ignored when estimating N. Daily mean N fluxes estimated using mass

Table 3.3: The associated mean errors of the fluxes, and individual components, used to calculate N using $c(\mathrm{O_2})$ (blue), and c(DIC) (green), and the errors associated with N calculated using buoy measurements (yellow).

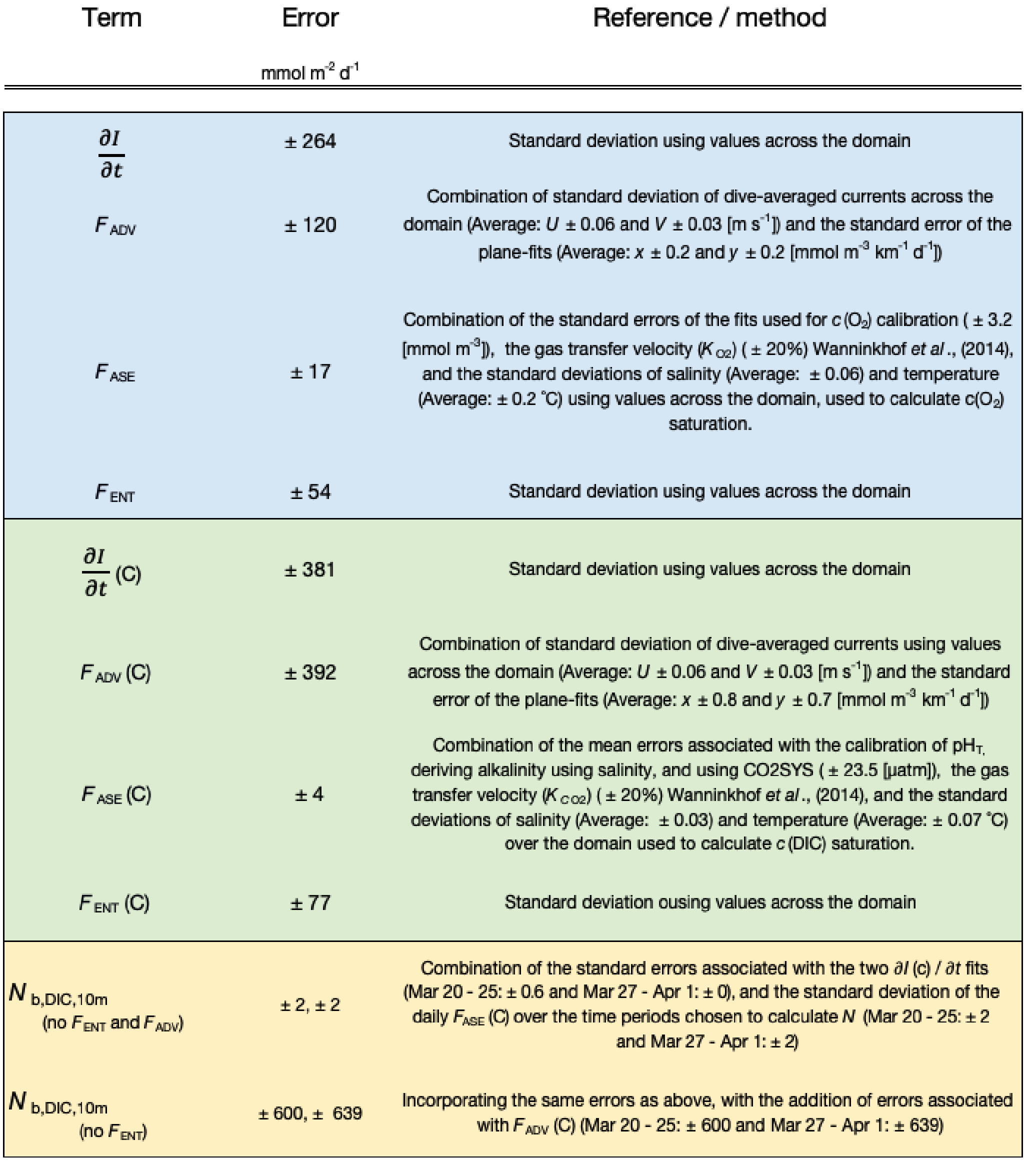

Term	Error mmol m^{-2} d^{-1}	Reference / method
$\frac{\partial I}{\partial t}$	± 264	Standard deviation using values across the domain
F_{ADV}	± 120	Combination of standard deviation of dive-averaged currents across the domain (Average: U ± 0.06 and V ± 0.03 [m s^{-1}]) and the standard error of the plane-fits (Average: x ± 0.2 and y ± 0.2 [mmol m^{-3} km^{-1} d^{-1}])
F_{ASE}	± 17	Combination of the standard errors of the fits used for $c(\mathrm{O_2})$ calibration (± 3.2 [mmol m^{-3}]), the gas transfer velocity (K_{O2}) (± 20%) Wanninkhof *et al*., (2014), and the standard deviations of salinity (Average: ± 0.06) and temperature (Average: ± 0.2 ˚C) using values across the domain, used to calculate $c(\mathrm{O_2})$ saturation.
F_{ENT}	± 54	Standard deviation using values across the domain
$\frac{\partial I}{\partial t}$ (C)	± 381	Standard deviation using values across the domain
F_{ADV} (C)	± 392	Combination of standard deviation of dive-averaged currents using values across the domain (Average: U ± 0.06 and V ± 0.03 [m s^{-1}]) and the standard error of the plane-fits (Average: x ± 0.8 and y ± 0.7 [mmol m^{-3} km^{-1} d^{-1}])
F_{ASE} (C)	± 4	Combination of the mean errors associated with the calibration of pH$_T$, deriving alkalinity using salinity, and using CO2SYS (± 23.5 [µatm]), the gas transfer velocity (K_{CO2}) (± 20%) Wanninkhof *et al*., (2014), and the standard deviations of salinity (Average: ± 0.03) and temperature (Average: ± 0.07 ˚C) over the domain used to calculate c(DIC) saturation.
F_{ENT} (C)	± 77	Standard deviation ousing values across the domain
$N_{b,DIC,10m}$ (no F_{ENT} and F_{ADV})	± 2, ± 2	Combination of the standard errors associated with the two ∂I (c) / ∂t fits (Mar 20 - 25: ± 0.6 and Mar 27 - Apr 1: ± 0), and the standard deviation of the daily F_{ASE} (C) over the time periods chosen to calculate N (Mar 20 - 25: ± 2 and Mar 27 - Apr 1: ± 2)
$N_{b,DIC,10m}$ (no F_{ENT})	± 600, ± 639	Incorporating the same errors as above, with the addition of errors associated with F_{ADV} (C) (Mar 20 - 25: ± 600 and Mar 27 - Apr 1: ± 639)

budgets were significantly affected by advection. N fluxes estimated using buoy c(DIC) with / without including advection were useful for comparing with N estimated using glider measurements during certain time periods, although calcification and entrainment effects were not explored. The spring bloom started in this area of the northwestern Mediterranean Sea on or around March 19 2016. This date was identified using trends in physical and biogeochemical measurements obtained by the glider and the buoy, and N estimated using all three methods. This date in March was expected, when considering that phytoplankton blooms occurred in either March or April in the past. However, this was the first time that high-resolution vertical profiles covering the wider DyFAMed area were used, offering insights into the biogeochemical and physical processes before, during, and after, the bloom.

4

Physical and Biogeochemical Scales of Variability in the Northwestern Mediterranean Sea Using Glider Measurements

4.1 Summary

Underwater gliders are more advantageous than traditional methods of ocean data collection, as high-resolution spatial and temporal information can be obtained remotely. Physical and biogeochemical spatial characteristics in the northwestern Mediterranean Sea were quantified using semivariograms derived from underwater glider measurements. The horizontal spatial scales obtained using semivariograms highlight the influence of certain processes (e.g. biology, weather) on key physical and biogeochemical parameters. Spatial scales are generally small when affected by photosynthesis (i.e. where chlorophyll patches form), and large when dominated by large-scale processes, such as atmospheric forcing. This was however not universal to every orientation and dataset, and in some cases the opposite could be seen. There is some anisotropy (i.e. different scales in different directions), as ranges calculated using zonal distances were larger than those calculated using meridional distances. This anisotropy may be related to ocean currents, or in the case of REP14 - MED, may be related to the limited meridional measurements collected by the gliders. The semivariogram models used to extract the spatial characteristics did not perform as well as in other studies (lower coefficient of determination (r^2) values). Obtaining spatial scales in the northwestern Mediterranean Sea is useful for designing

future observational glider campaigns in the region.

4.2 Introduction

High-resolution measurements of physical and biogeochemical parameters were obtained by underwater gliders at two locations in the northwestern Mediterranean Sea: the Sardinian Sea in June 2014, and close to the BOUSSOLE (translated from French as 'buoy for the acquisition of a long-term optical time series', (Antoine et al., 2008)) biogeochemical buoy in March - April 2016 off the coast of France (Fig. 4.1). Underwater gliders are relatively cheap, costing a fraction of the cost of a full ship survey or mooring deployment. Gliders are more manoeuvrable, and energy efficient than ship and mooring measurements (Eriksen et al., 2001). Ship surveys normally last just a few weeks or months at a time. Measurements obtained by ship are often higher resolution in the vertical (1 m to 2 m) than in the horizontal (some kilometres), and data distributions are often discrete and not repeated over time. Measurements obtained by moored buoys are isolated spatially, both horizontally and vertically, but temporal resolution is good (Hemsley, 2003). Therefore, measurements obtained by ship or moored buoys cannot resolve all scales of temporal and spatial variability. Underwater glider spatial and temporal information can be controlled. High-resolution spatial and temporal measurements can be repeated over periods lasting months at a time (Eriksen et al., 2001; Rudnick, 2016). With an expected increase in underwater glider use in future, quantifying scales of spatial variability is useful in the design of underwater glider observational campaigns that aim to capture important features and processes. Determining the spatial characteristics of water masses in a particular region aid the development of ocean models by establishing the dominant processes determining variability, and improve data assimilation techniques through the determination of observation spatial footprints (Schaeffer et al., 2016).

The physical characteristics of water masses are predominantly driven by density changes, wind forcing, and bathymetry, whilst the biogeochemical characteristics of water masses are further determined by locally acting biological processes, such as photosynthesis and respiration, nutrient cycling, and remineralisation (Schaeffer et al., 2016; Ballantyne IV et al., 2011). The mechanisms driving phytoplankton communities are complex, and their distributions range over many spatial scales of variability (Schaeffer et al., 2016; Martin, 2003). A range of theories exist relating to the physical and biological controls on the patchiness of phytoplankton communities (Steele, 1978; Denman and Abbott, 1988). Processes occurring at the interface between the continental shelf and the open ocean are relevant on small spatial scales, as water masses governed by either oceanic, or coastal processes interact here (Yoder et al., 1987).

The Mediterranean Sea is considered a 'laboratory basin', where global-scale processes occur on smaller spatial and temporal scales than in other oceans (Álvarez et al., 2014). The Mediterranean Sea is generally considered oligotrophic when compared globally (Álvarez et al., 2014), however phytoplankton blooms are common in spring and autumn, and a deep chlorophyll maximum (DCM) is often present during the summer when waters are stratified (Estrada, 1996). The northwestern Mediterranean Sea is characterised by Modified Atlantic Water (MAW) typically in the top 140 m of the water column, Levantine Intermediate Water (LIW) typically between 80 m and 730 m, Winter Intermediate Water (WIW) typically between 120 m and 400 m, and Western Mediterranean Deep Water (WMDW) deeper than 535 m. These depth ranges are dependent on space and time (Knoll et al., 2017). Wind-driven vertical mixing in the top 300 m of the water column is dominant during the winter and autumn periods, whilst surface stratification is common during the summer (Copin-Montégut et al., 2004).

The Sardinian Sea includes both open ocean and continental shelf environments. In June 2014, off-shelf geostrophic transport in the Sardinian Sea was northward. Closer to the shelf edge, it was southward near the surface (MAW), but predominantly northward at depths corresponding to LIW across all areas (Knoll et al., 2017). As a result of strong summer stratification, a DCM was present in the Sardinian Sea at depths of 20 m to 90 m in 2014 (Fig. 2.12).

The BOUSSOLE site is considered open ocean, with a bottom depth >2000 m. West / south-westward geostrophic transport is found here at depths corresponding to MAW and LIW (Millot, 1999; Niewiadomska et al., 2008). In 2016, wind-driven vertical mixing at the BOUSSOLE site was strong during the first half of March, but weaker during the second half, resulting in an increase in primary production after 19 March (Fig 3.7).

In this chapter, physical and biogeochemical spatial characteristics in the northwestern Mediterranean Sea are quantified using semivariograms derived from underwater glider measurements. The purpose of this is to understand the variability of physical and biogeochemical properties in this region, relating the observed correlation patterns to underlying processes. The glider data sets, including the sensor payloads, calibrations, and data processing techniques are described in Section 4.3.1, and semivariograms are described in Section 4.3.2. The results, including the spatial characteristics, spatial anisotropy, and the unresolved variances are presented and discussed in Section 4.4. Previous studies investigating spatial characteristics at other regions are discussed in Section 4.5, and the results are discussed within the context of designing observational systems in Section 4.6. Finally, the conclusions of the chapter are presented in Section 4.7.

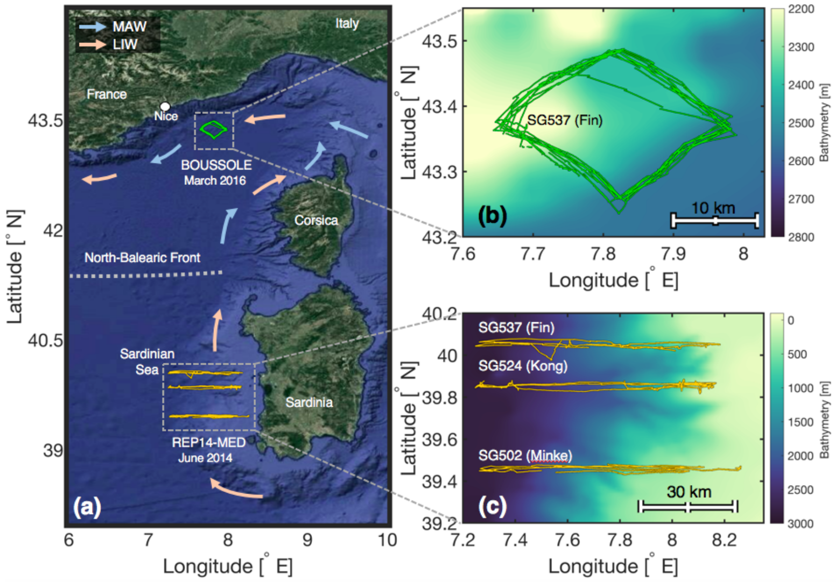

Figure 4.1: (a) The locations of the BOUSSOLE (green) and REP14 - MED (orange) deployments. (b) A close-up of the BOUSSOLE deployment between 7 March and 5 April 2016. (c) A close-up of the REP14 - MED experiment between 6 and 25 June 2014. The satellite image in panel (a) has been taken from GoogleMaps, and has no corresponding colour scale. GEBCO 1 minute resolution bathymetry data (metres) were used in (b) and (c) (http://www.bodc.ac.uk/projects/international/gebco/). Note the difference in bathymetry scales in (b) and (c). Circulation flows in Modified Atlantic Water (MAW, blue), and Levantine Intermediate Water (LIW, pink) are shown, which are adapted from Millot (1999).

4.3 Data and Methods

4.3.1 Glider Datasets

REP14

Three gliders operated by the University of East Anglia were deployed between 6 and 25 June 2014 in the northwestern Mediterranean Sea off the west coast of Sardinia, Italy as part of the REP14 - MED experiment (Fig. 4.1). These three gliders were Fin (SG537), Kong (SG524), and Minke (SG502), which carried out repeat zonal transects between 7.2° and 8.3° E, 39.3° and 40.2° N. Fin and Kong were separated by 0.2° of latitude from one another, whilst Minke was 0.4° further south from Kong. Gliders Fin, Kong, and Minke completed dives down to a maximum depth of 1000 m when not on the shelf, with surface coordinates separated approximately by 2 km to 4 km. An in-depth overview of the REP14-MED trial, its objectives, and the collected observational data is described by Onken et al. (2018). ‘REP14 - MED’ will be shortened to ‘R14’ below to improve the flow of reading.

BOUSSOLE

Glider Fin was deployed between 7 March and 5 April 2016 close to the BOUSSOLE buoy in the northwestern Mediterranean Sea, roughly 52 km away from Nice, France (Fig. 4.1). Fin repeatedly sampled four transects in time every four days. A diamond pattern was formed by the four transects, with eight diamond patterns completed over the course of the deployment. Most dives reached a maximum depth of 1000 m, with surface dive coordinates separated approximately 5 km on average. A detailed overview of the BOUSSOLE location, and the deployment objectives can be found in Chapter 3. 'BOUSSOLE' will be shortened to 'B16' below to improve the flow of reading.

Sensor Payloads, Calibrations, and Data processing

Gliders Minke, Kong, and Fin had different sensor payloads (Table 4.1). During R14, temperature and salinity were obtained by each glider using the glider CTD sensor. Dissolved oxygen concentrations ($c(\mathrm{O_2})$) were measured using an Aanderaa model 4330 optode sensor by Minke and Fin only. During B16, Fin measured temperature, salinity, and $c(\mathrm{O_2})$, using the exact same sensors as those used during R14. pH on the total scale ($\mathrm{pH_T}$) was measured using experimental ion sensitive field effect transistor (ISFET) pH-$p(\mathrm{CO_2})$ sensors attached to Fin during both the R14 and B16 deployments (see Section 2.3.2). Optical backscatter at a wavelength of 700 nm was measured using a WET Labs Eco Puck sensor on Fin.

R14 and B16 glider measurements were compared with ship CTD casts and water samples undertaken close in time and space. This included temperature, salinity, $c(\mathrm{O_2})$, and $\mathrm{pH_T}$. During R14, this included 256 CTD casts undertaken by research ships *Alliance* and *Planet* (Onken et al., 2018). Eight casts included dissolved inorganic carbon ($c(\mathrm{DIC})$) and total alkalinity (A_T) (used to derive $\mathrm{pH_T}$), and $c(\mathrm{O_2})$ water samples, and 111 casts measured $c(\mathrm{O_2})$ using a SBE43 electrode sensor. During B16, two CTD casts were undertaken by the research ship *Tethys II*: one in March, and one in April 2016. Additional temperature, salinity, and $c(\mathrm{O_2})$ measurements recorded at the biogeochemical mooring (Fig. 3.1) were used to compare with B16 glider measurements.

Glider $c(\mathrm{O_2})$ was higher than $c(\mathrm{O_2})$ in samples collected by ship during R14 and B16. This was particularly true in the top 100 m of the water column. During R14 and B16, $c(\mathrm{O_2})$ measured by each glider was calibrated to take into account the response time (τ) lag of the sensor, and the differences between ship and glider $c(\mathrm{O_2})$. The method of calibrating glider $c(\mathrm{O_2})$ for R14 and B16 is described in detail in Section 2.3.2 and Section 3.3.3, respectively.

$\mathrm{pH_T}$ measured by the experimental ISFET sensors during R14 and B16 were different to $\mathrm{pH_T}$ derived using ship water samples of $c(\mathrm{DIC})$ and A_T. The ISFET $\mathrm{pH_T}$ were first

Table 4.1: Data information for the top 300 m for each glider used during REP14 - MED (R14) and BOUSSOLE (B16).

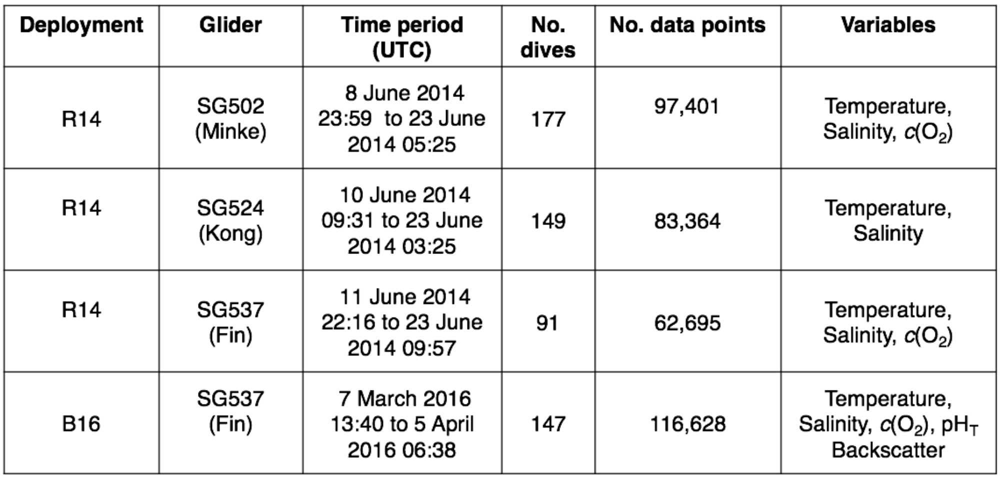

Deployment	Glider	Time period (UTC)	No. dives	No. data points	Variables
R14	SG502 (Minke)	8 June 2014 23:59 to 23 June 2014 05:25	177	97,401	Temperature, Salinity, $c(O_2)$
R14	SG524 (Kong)	10 June 2014 09:31 to 23 June 2014 03:25	149	83,364	Temperature, Salinity
R14	SG537 (Fin)	11 June 2014 22:16 to 23 June 2014 09:57	91	62,695	Temperature, Salinity, $c(O_2)$
B16	SG537 (Fin)	7 March 2016 13:40 to 5 April 2016 06:38	147	116,628	Temperature, Salinity, $c(O_2)$, pH_T Backscatter

corrected for linear drift over time using pH_T measurements in 2-aminopyridine (AMP) and 2-amino-2-hydroxymethy-1,3-propanediol (TRIS) buffer solutions with defined pH_T (6.79 and 8.09, respectively) before and after the deployments. The ISFET pH_T were further corrected for multi-directional residual drift (i.e. non-linear, depth-independent drift), and for temperature and pressure effects. The methods used to correct ISFET pH_T during R14 and B16 have been described in detail in Section 2.3.2, Section 2.4.2, and Section 3.3.3, respectively.

Glider samples of all parameters collected within the top 300 m were used for analysis. This depth was chosen as it included the mixed layer (generally < 20 m during R14, and < 200 m during B16), MAW, and LIW, and reduced the computational power and time required to calculate semi-variograms for the entire profile. Between 62,695 and 116,628 data points were measured by each glider within this 300 m depth range during a given deployment (Table 4.1). Overall, more data points were obtained during R14 than during B16 (Fig. 4.2c). During R14, a higher concentration of data points was obtained closer to the shelf than in the open ocean (Fig. 4.2a). In contrast, during B16 the data points were collected more uniformly along the diamond-forming transects (Fig. 4.2b). All data were visually inspected, and outliers outside certain thresholds (e.g. *n* times the standard deviation at a given depth) were flagged and discarded from further analysis.

Temperature measured in the top 5 m of the water column was subject to a diel cycle (Fig. 4.3a,b). The temperature anomaly cycle was calculated by obtaining averages each hour every 1 m depth, which were subtracted from the the mean temperature anomaly at the same depth throughout time. The temperature diel cycle in the top 5 m had a negligible effect on the calculated semivariances used for semivariogram analysis (explained in Section 4.3.2). In the top 20 m of the water column, the r^2 values calculated by fitting an

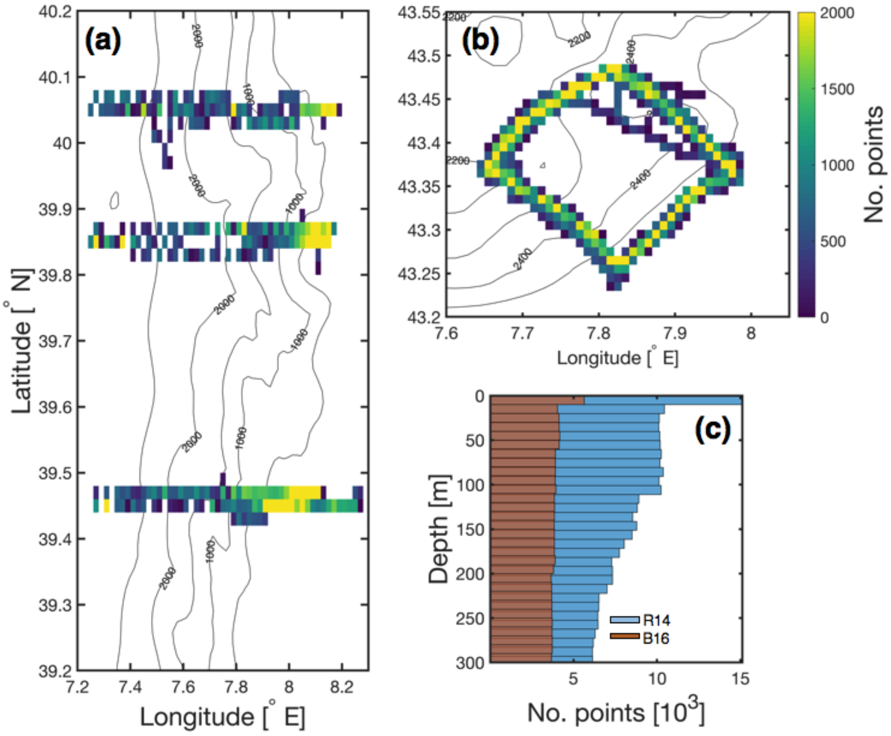

Figure 4.2: The number of glider data points per bin area during R14 (a), and during B16 (b) in the top 300 m. Contour lines in (a) and (b) represent depth in metres. (c) Data point distributions between the surface and 300 m depth during R14 (blue) and B16 (red).

exponential fit on temperature semivariances was 0.69 irrespective of whether the diel cycle was removed or not, and the semivariogram components (explained in Section 4.3.2) were similar. Therefore, the diel cycle was not removed from glider measurements.

4.3.2 Characterising Spatial Variability

Semivariograms

Semivariograms were first introduced by Journel and Huijbregts (1978) in the field of geostatistics to characterise the spatial variability of sparsely populated and irregularly spaced data. Since then, their usefulness in oceanography has been demonstrated using satellite ocean surface measurements, and glider measurements (Doney et al., 2003; Legaard and Thomas, 2007; Schaeffer et al., 2016; Todd et al., 2013). A semivariogram is used to determine the average dissimilarity (or semivariance) between data points as a function of the distance between them. The semivariance is small when data points are close together and better correlated with one another, but large when data points are further separated and less correlated with one another.

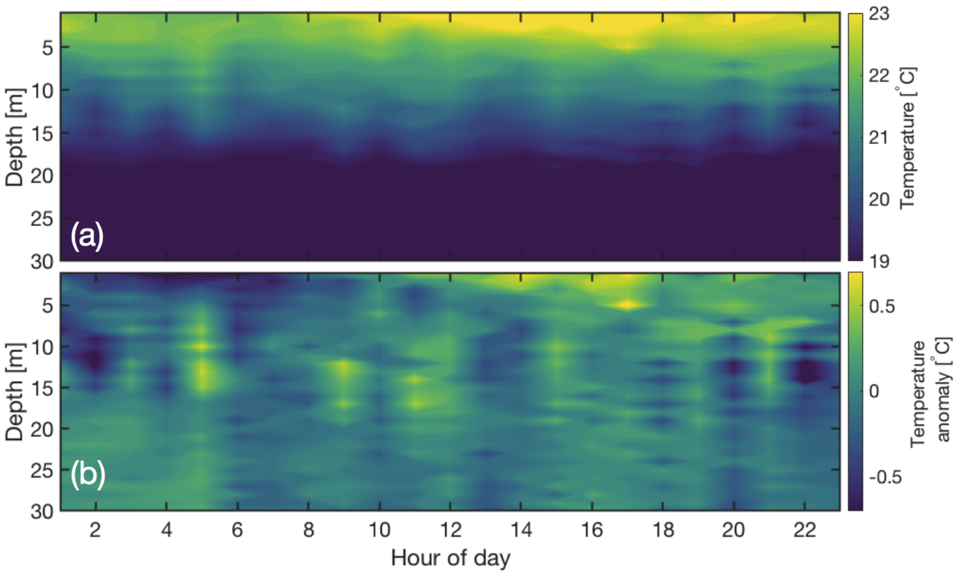

Figure 4.3: (a) Glider Minke temperature in the top 30 m of the water column as a function of the time of day. (b) Glider Minke temperature anomalies in the top 30 m calculated for each hour of the day (UTC).

A semivariogram is defined as half the mean square difference between a single variable anomaly ($Z(x)$) and the remaining variable anomalies separated by distance (l):

$$\gamma(l) = \frac{1}{2}\frac{1}{N}\sum([Z(x) - Z(x+l)]^2) \tag{4.1}$$

where the resulting sum is over all N pairs of variable anomalies that are separated by l in the x direction. Equation 1 assumes that the distribution of the variable anomalies is normal. However, in practice variable anomaly distributions can be skewed as a result of outliers. Cressie and Hawkins (1980) proposed a more robust semivariogram that reduces the skewness of distributions contaminated by outliers:

$$\gamma(l) = \frac{\frac{1}{2}\left(\frac{1}{N}\sum([Z(x) - Z(x+l)]^{\frac{1}{2}}\right)^4}{0.457 + \frac{0.494}{N}} \tag{4.2}$$

where the fourth root of $[Z(x) - Z(x+l)]^2$ provides a robust estimate of the semivariogram, the fourth square amends the scale and units to that as in Eq. (1), and the bias is adjusted using the denominator.

Anomalies of the variables were calculated by removing the deployment-period trend, reducing the influence of temporal variability on calculated semivariances. For R14, each glider data set was de-trended separately. Anomaly differences ($[Z(x) - Z(x+l)]$) within 1 day of one another were used for semivariogram analysis. Whether or not variability depended on direction (anisotropy/isotropy) was investigated, where l was either zonal or meridional distance, or the zonal and meridional axes combined. Distance l was discretised using 1 km intervals (i.e. one semivariance value was calculated every 1 km distance). Semivariograms were calculated for individual 5 m depth bins from the surface down to 300 m for the deployment time period. The semivariances for each 5 m bin were calculated using measurements within 2 standard deviations of the mean of the selected data (roughly 95 % of data points), and using at least 30 pairs (i.e. $[Z(x) - Z(x + l)]$ contains ≥ 30 elements). The median number of pairs per discretised 1 km distance lag was 1642 when considering all gliders and deployments. During R14, semivariances calculated closer to the surface used a higher number of pairs than those calculated at greater depth, as more data points were measured here (Fig. 4.2c). This was because the gliders performed shallower dives across the shelf slope. Cartesian coordinates were used for l, which were calculated by subtracting each longitude and latitude measurement point from one constant location outside of the domain. This constant location (arbitrarily chosen) was situated to the north west of the most north-westerly glider measurement in both R14, and B16.

A mathematical exponential model (Biswas and Si, 2013) was fit to the empirical semivariogram to extract three components: the nugget (σ_0^2), sill (σ^2), and range (r) (Fig. 4.4), which help to identify dominant scales of variability:

$$\gamma(l) = \sigma_0^2 + (\sigma^2 - \sigma_0^2)\left\{1 - \exp\left(\frac{-l}{r}\right)\right\} \tag{4.3}$$

σ_0^2 represents the lower semivariance limit. Any variability below this threshold has not been resolved by the glider measurements, or has been masked by instrumental noise (Doney et al., 2003). σ^2 is the semivariance at $l \rightarrow \infty$ identified by the exponential model. r is the distance where semivariances start to plateau (i.e. at optimum decorrelation). The exponential model was fit to semivariances within the first 30 km. This was to ensure consistency between semivariograms calculated using R14 and B16 measurements, as the range of B16 measurements did not exceed 30 km. If the exponential fit did not plateau within 30 km, the fit was extrapolated further in length until a plateau was reached, and r was determined. Spherical, gaussian, and circular models were also tested. However, the coefficient of the determination (r^2) statistics for these fits were on average 0.05 less than the r^2 statistics using the exponential fit. Depth layers where the r^2 value was less than 0.2 were excluded from analysis (See Fig. A.5 in the appendix for examples of semivariogram exponential model fits with varying r^2 statistics). The exponential fits were weighted following Cressie (1985), where most weight is given to shorter lags, and lags with more pairs. Each semivariogram was analysed by eye to check whether the exponential fits adequately modelled the semivariances. The overall number of points used for the fit, the residuals within the first 5 km to 10 km, and the residuals over the entire distance range when ignoring outlier semivariances were considered when analysing the fits by eye. The root mean squared error (RMSE) was used to assess the exponential models further, which incorporates the residuals of the dependent and predicted values in the model. The RMSE was calculated for each exponential fit between the surface and 300 m depth. As the R14 and B16 RMSEs varied as a function of depth (dependent on the variance) and the parameter used, they could not be directly compared with one another. Instead, the RMSE percentage was calculated by dividing the RMSE by the semivariance range for that particular depth and parameter, multiplied by 100. The average RMSE percentage for a given deployment and variable was calculated using all RMSEs between the surface and 300 m depth. Zonal transects obtained during R14 were typically 80 to 90 km long. Semivariances calculated using variable anomalies separated >30 km away from one another, such as during R14, were compared with those calculated <30 km, and the exponential fit, to determine whether the sill had been correctly predicted by the model. R14 $\mathrm{pH_T}$ fits were overall poor (low r^2 values), hence the corresponding semivariograms and associated spatial characteristic components (e.g. r, σ_0^2, etc.) are excluded from further discussion.

The semivariogram components used to characterise spatial variability, and calculated every 5 m, are presented as profiles using means every 20 m between the surface and 300 m depth. Binning the profiles every 20 m smoothed out outlier spatial characteristic components (e.g. r, σ_0^2 ..) at some depths. The binned standard deviations illustrate the depths where outlier components were calculated. Semivariograms were calculated using zonal and meridional distances separately, and across the entire domains regardless of direction to investigate anisotropy. For R14, the zonal and meridional orientations have been named ‘across-shelf’ and ‘along-shelf’, respectively, to highlight the dominance of the shelf. For B16, the zonal and meridional orientations have been named ‘along-current’ and ‘across-current’, respectively, to highlight the dominance of a west / south-westward geostrophic current in the region.

Example Semivariogram Calculations

To test that the semivariograms were working correctly, three artificially produced data fields covering a 50 km x 50 km area were used. The first data field (Fig. 4.5a) represented a random assortment of temperature values between 14 °C and 15 °C. As the correlation between data points was consistently low at all separation distances, the exponential fit failed, and the corresponding σ_0^2, σ^2, and r were not estimated (Fig. 4.5d). The second (Fig. 4.5b) represented a temperature field between 13.8 °C and 15 °C dominated by a consistent sinusoidal signal in space emanating from the southwest, perhaps resembling in part an area affected by internal tides. For this example, the σ_0^2, σ^2, and r, were

1×10^{-4} °C, 5.5×10^{-4} °C, and 5 km, respectively (Fig. 4.5e). The consistent sinusoidal signal could be seen in the calculated semivariances after distance r. The semivariances were therefore indicative of multiple correlations throughout the area. The third artificially created temperature field (Fig. 4.5c) represented a normally distributed data set with the mean set at 14 °C, and a standard deviation of 0.3 °C. This field was created using the MATLAB function 'randomfield.m', using a spatially varying variance (equal to $\cos(\pi \times \sin(2\,\pi\, y) + 1.5)$. This temperature field might resemble in part a patchy ocean environment where cooler water is actively mixing with warmer water. This data field produced a 'typical' semivariogram pattern (Fig. 4.5f), with the semivariance increasing gradually from close to zero at minimum l, towards σ^2. In this case, the σ_0^2, σ^2, and r, were 0.02 °C, 0.17 °C, and 13 km, respectively. The third artificially created temperature field had a clear anisotropic pattern. Calculating semivariograms seperately along the zonal and meridional orientations produced different results. The range r of variability was 8 km and 15 km in the zonal, and meridional orientations, respectively.

To test whether the spatial distribution of data obtained during R14 and B16 (Fig. 4.2a,b) had an effect on calculated semivariograms, data created in the same manner as produced for Fig. 4.5c was subsampled onto similar cartesian coordinates as R14 and B16 measurements. The subsampled data field was spatially larger than the data field shown in Fig. 4.5c to accommodate R14 coordinates (80 km x 90 km, rather than 50 km x 50 km), but the general patterns were visually similar. The range and r^2 were affected by the spatial distribution of the data collected during R14, and B16 (Table. 4.2). B16 semivariograms had lower r^2 fits than calculated for R14, and when no subsampling was done, and the ranges in each orientation (zonal, meridional, and domain-wide) were not consistent. These results suggest that the spatial characteristics obtained by semivariograms depend on the sampling method undertaken by a glider. However, the artificially-created data field was gridded, which is unlike the scattered glider measurements.

4.4 Results and Discussion

4.4.1 r^2 Statistic

The performance of the exponential models was assessed using their r^2 statistics, which varied between deployment, as a function of depth, and axes direction (Fig. 4.6a-c, 4.7a-c). The models performed best for across-shelf/along-current and domain-wide semivariances during R14. r^2 values were at some depths > 0.7. Overall, the r^2 statistics were higher using R14 measurements than B16 measurements, particularly within the top 100 m of the water column (Table 4.3 and Table 4.4). This could be related to the increased number of data points during R14, compared with B16 (as demonstrated using artificially generated data - Table. 4.2), particularly closer to the surface (Fig. 4.2c). On average, the B16 r^2 values

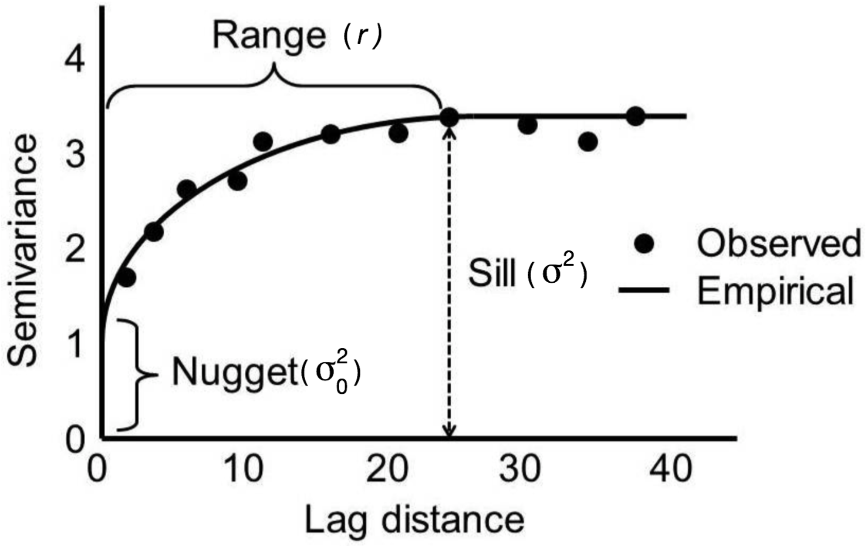

Figure 4.4: An example of a semivariogram showing the nugget (σ_0^2), range (r), and sill (σ^2) components (Biswas and Si, 2013)

Table 4.2: The ranges, and r-squared statistics obtained using artificially-created data (similar to Fig. 4.5c) along different orientations (longitude, latitude, and domain-wide), using the complete field, subsampling R14 coordinates, and subsampling B16 coordinates.

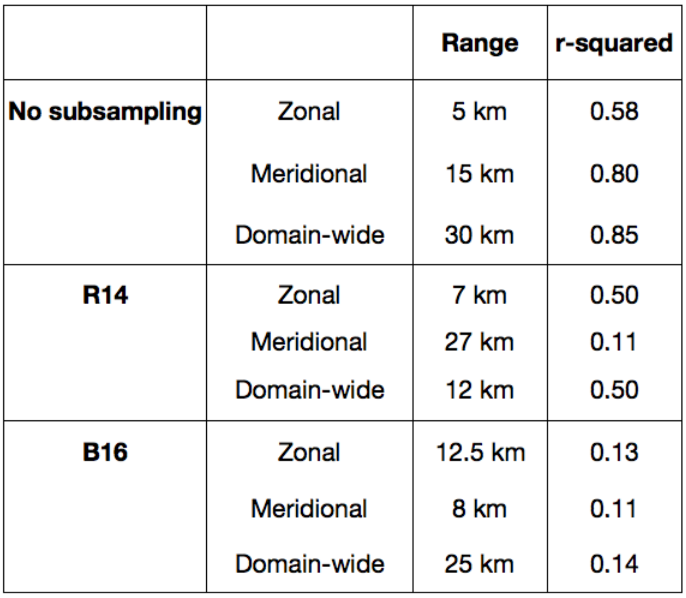

		Range	**r-squared**
No subsampling	Zonal	5 km	0.58
	Meridional	15 km	0.80
	Domain-wide	30 km	0.85
R14	Zonal	7 km	0.50
	Meridional	27 km	0.11
	Domain-wide	12 km	0.50
B16	Zonal	12.5 km	0.13
	Meridional	8 km	0.11
	Domain-wide	25 km	0.14

were low. The spread of differences between variable anomalies as a function of distance ($[Z(x) - Z(x + l)]$) prior to calculating the robust semivariance proposed by Cressie and Hawkins (1980) were generally positively skewed for R14 and B16 for most depths, with the majority of variable anomaly differences being low. Low r^2 values were associated with depths that included a considerable amount of outlier semivariances over the 30 km range (Appendix A, Fig. A.5). Most outlier semivariances resulted from a lack of data points,

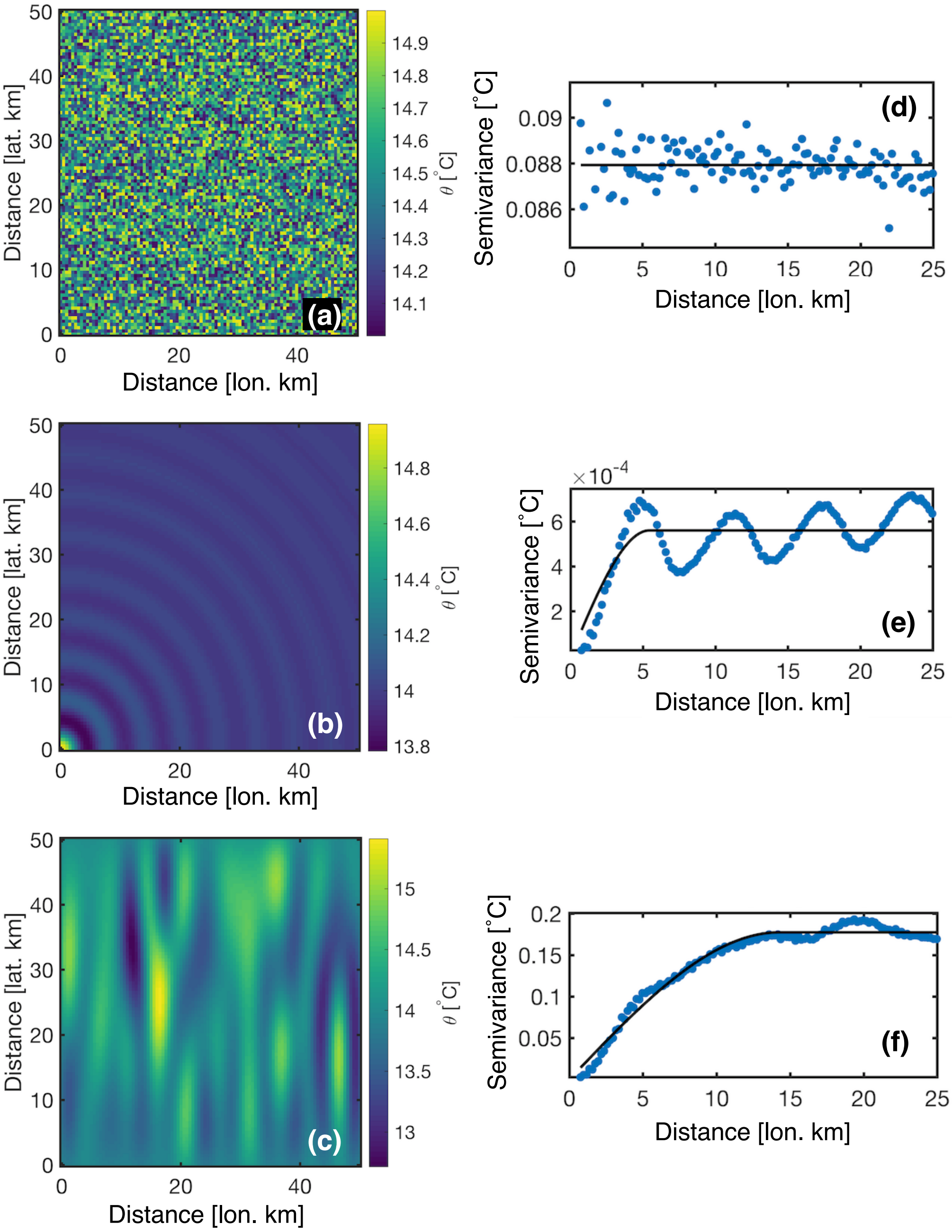

Figure 4.5: Three artificially generated temperature fields with specific characteristics: random distribution (a), dominant sinusoidal signal (b), and normal distribution (c). The corresponding semivariograms for the temperature fields in (a)-(c) can be found alongside in (d)-(f).

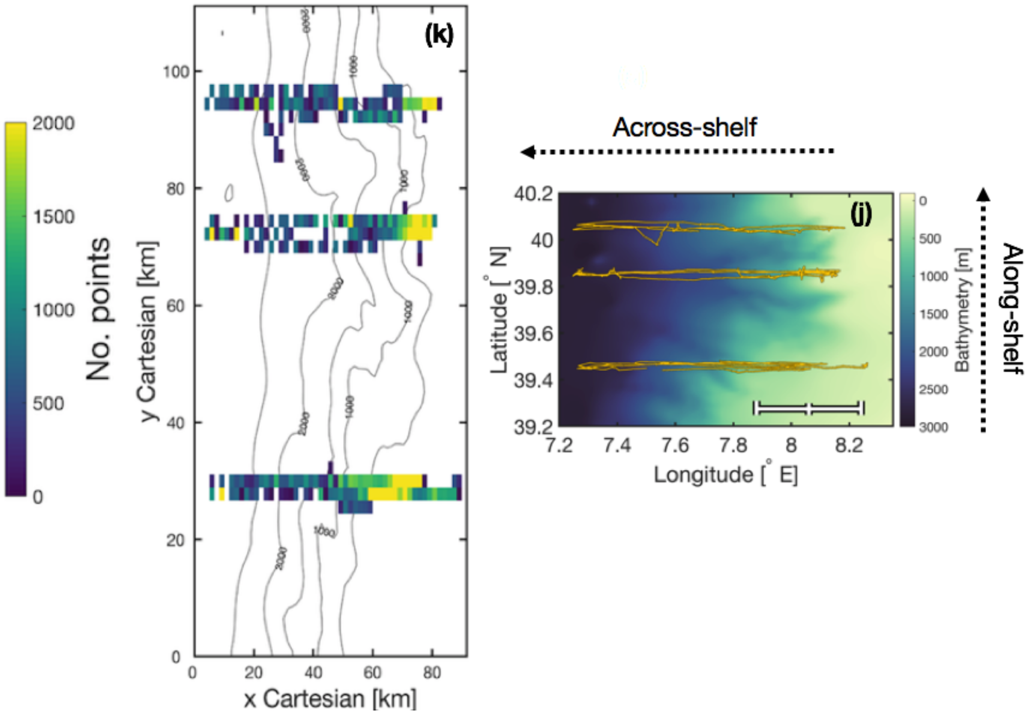

Figure 4.6: This figure and caption includes the panels above and on the next page. The calculated REP14 - MED (R14) semivariogram coefficient of a determination (r^2), ranges (r), and sills (σ^2) for temperature (blue), salinity (red), and dissolved oxygen concentrations ($c(O_2)$, yellow) using across-shelf distances (a,d,g), along-shelf distances (b,e,h), and domain-wide distances (c,f,i). The shaded areas represent the standard deviations and are linked to the lines by colour. Standard deviations were calculated when binning the results every 20 m. The glider transects are superimposed on top of the bathymetry (j, taken from Fig. 4.2b) and coloured by the number of data points available in the top 300 m (k, taken from Fig. 4.2a) with the across-shelf and along-shelf arrows added. The blue, red, and yellow x-axes below panels (g), (h), and (i) represent the scales for temperature, salinity, and $c(O_2)$ sill values.

where the spread of $[Z(x) - Z(x+l)]$ was less dense around the distribution statistical mode (i.e. small distribution kurtosis), or where a large proportion of variable anomaly differences were similar (i.e. large distribution kurtosis). This was the case for B16. A large number of exponential fits using along-shelf R14 measurements produced r - square values < 0.2. This can be explained by semivariance gaps within the distance lag l range. Along-shelf temperature and salinity semivariances for R14 could only be calculated within the first 30 km, between 40 km and 50 km, and between 55 km and 70 km due to the latitudinal positions of the glider transects (Fig. A.6). As R14 $c(O_2)$ were only measured by Minke and Fin a gap of 45 km separated the semivariances, reducing the quality of the exponential fits. Although along-shelf $c(O_2)$ semivariances existed within the first 30 km where the exponential model was fitted, the number of pairs used to calculate these semivariances were lower than the number of pairs used to calculate across-shelf, and domain-wide $c(O_2)$ semivariances.

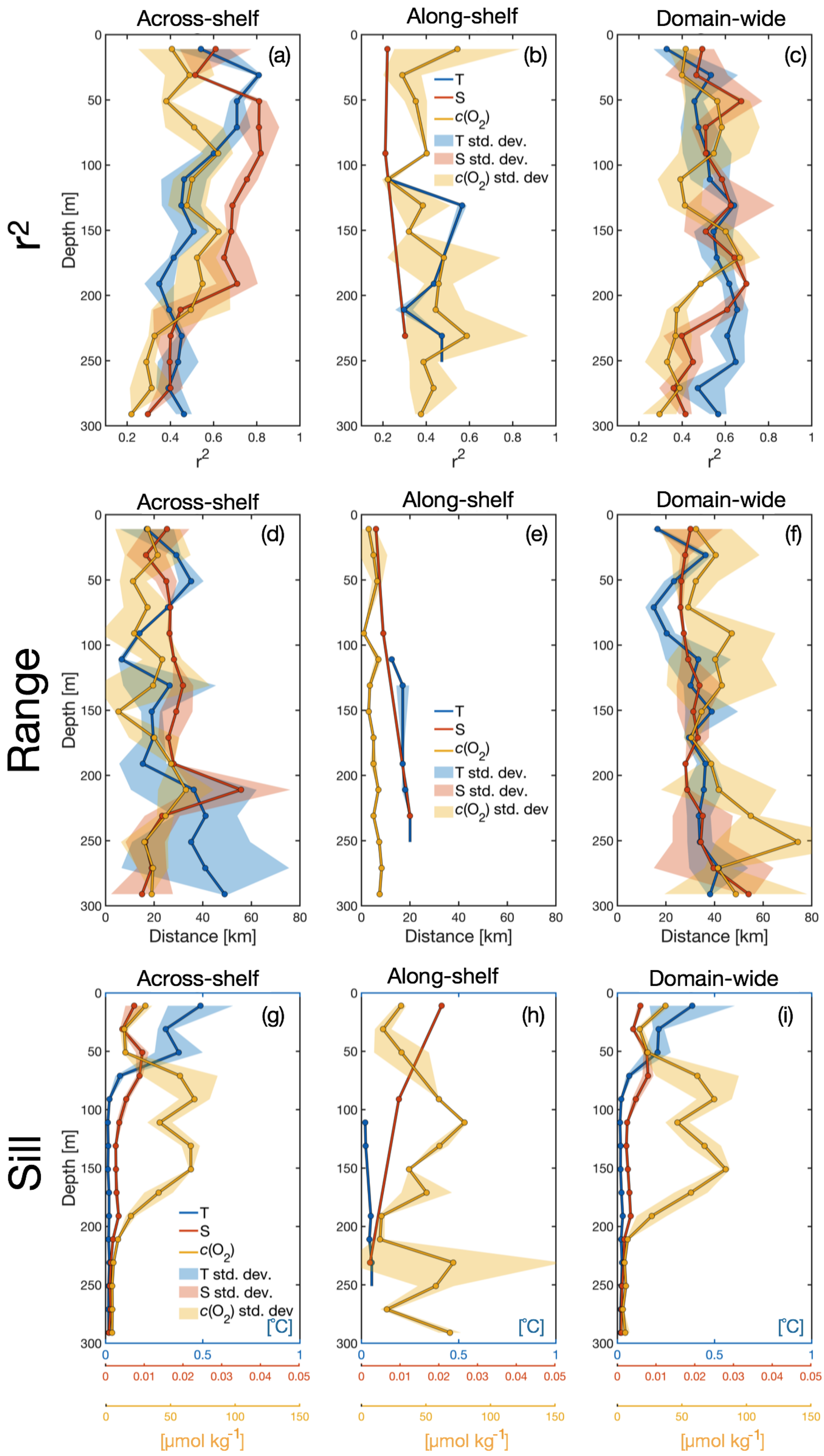
r2
Range
Sill
Across-shelf
Along-shelf
Domain-wide
(a)
(b)
(c)
(d)
(e)
(f)
(g)
(h)
(i)
Depth [m]
0
50
100
150
200
250
300
r2
0.2
0.4
0.6
0.8
1
Distance [km]
0
20
40
60
80
T
S
c(O2)
T std. dev.
S std. dev.
c(O2) std. dev
[°C]
0
0.5
1
0
0.01
0.02
0.03
0.04
0.05
0
50
100
150
[μmol kg-1]

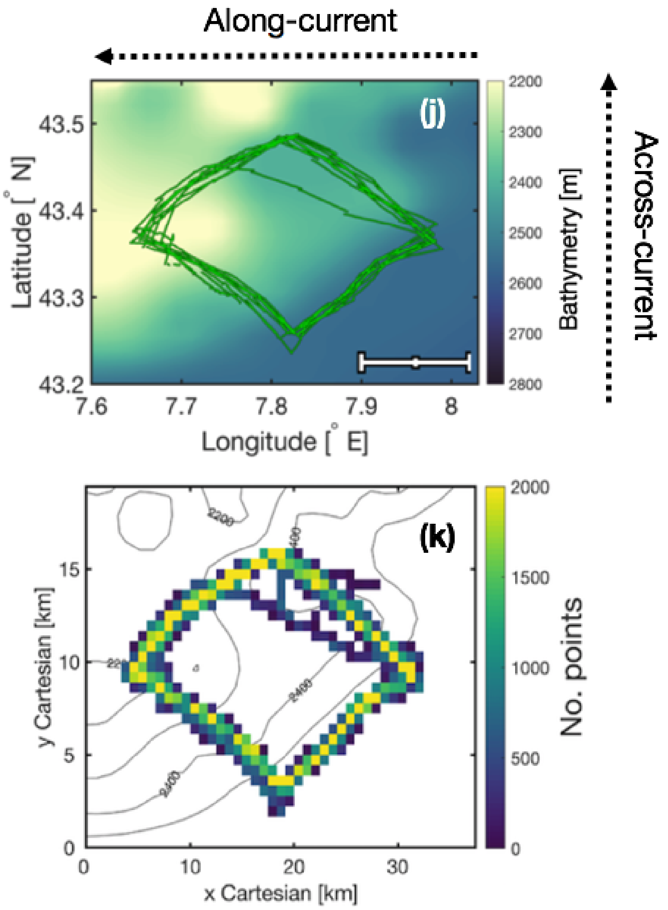

Figure 4.7: This figure and caption includes the panels above and on the next page. The calculated BOUSSOLE (B16) determination of a coefficient (r^2), ranges (r), and sills (σ^2) for temperature (blue), salinity (red), dissolved oxygen concentrations ($c(O_2)$, yellow), pH_T (purple), and optical backscatter (green) using across-shelf distances (a), along-shelf distances (b), and domain-wide distances (c). The shaded areas represent the standard deviations and are linked to the lines by colour. Standard deviations were calculated when binning the results every 20 m. The glider transects are superimposed on top of the bathymetry (j, taken from Fig. 4.2b) and coloured by the number of data points available in the top 300 m (k, taken from Fig. 4.2a) with the along-current and across-current arrows added. The blue, red, yellow, purple, and green x-axes below panels (g), (h), and (i) represent the scales for temperature, salinity, $c(O_2)$, pH, and optical backscatter sill values.

The RMSE percentages were calculated to assess the exponential models. On average, R14 and B16 RMSE percentages were between 14 % and 24 % of the semivariance range when considering all depths, directions, and parameters. The highest average RMSE percentages were calculated using the R14 meridional residuals. However, most average RMSE percentages were less than 19 %.

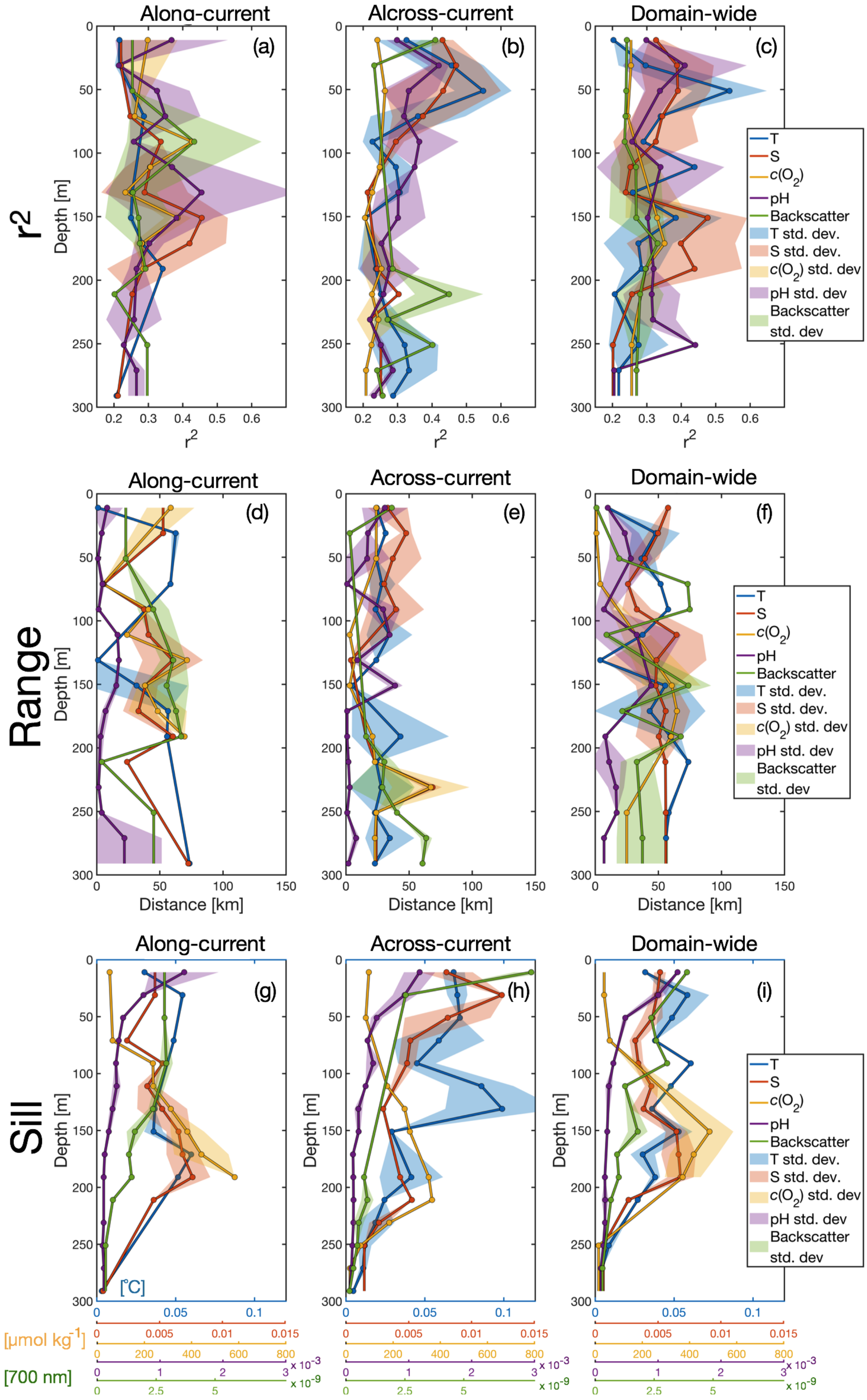
r2
Along-current
(a)
Alcross-current
(b)
Domain-wide
(c)
Depth [m]
r2
T
S
c(O2)
pH
Backscatter
T std. dev.
S std. dev.
c(O2) std. dev
pH std. dev
Backscatter std. dev
Range
Along-current
(d)
Across-current
(e)
Domain-wide
(f)
Distance [km]
Sill
(g)
(h)
(i)
[°C]
[µmol kg-1]
[700 nm]
0.05
0.1
0.005
0.01
0.015
200
400
600
800
x 10-3
x 10-9
2.5
5

4.4.2 Range

Horizontal ranges calculated using the zonal direction only (Across-shelf for R14, and Along-current for B16) tended to be larger than those calculated using the meridional direction only (Along-shelf for R14, and Across-current for B16) (Fig. 4.6 d-e, Fig. 4.7d-e). Average differences are clearer between R14 along- and across-shelf ranges (Table 4.3), than with the B16 across- and along-current ranges (Table 4.4). This suggests that there was anisotropy at these regions during the deployments. However, many R14 along-shelf ranges could not be calculated due to the poor fits (low r^2), and as discussed in Section. 4.3.1, this apparent anisotropy could just be a result of the glider meridional sampling. R14 and B16 domain-wide ranges tended to be larger than the ranges calculated using single directional axes. Average along-shelf and across-shelf R14 $c(O_2)$ ranges were often smaller than temperature and salinity ranges, whereas average domain-wide $c(O_2)$ ranges were often larger than temperature and salinity ranges. This suggests that biological processes may have been the driving force in $c(O_2)$ variability. Average R14 temperature, salinity, and $c(O_2)$ ranges were between 5 km and 36 km, 6 km and 60 km, and 2 km and 43 km, respectively, irrespective of direction. Small temperature and $c(O_2)$ ranges were found within the top 10 m of the water column during R14. Average B16 temperature, salinity, $c(O_2)$, and backscatter ranges were typically between 23 km and 72 km irrespective of direction, when excluding the anomalous domain-wide surface average backscatter range of 1 km. Large ranges were quite often found at the surface, such as in the across-current direction. B16 pH_T ranges were typically lower (between 2 km and 21 km) than the other measured parameters, irrespective of direction.

Temperature and salinity on spatial scales of variability found in this study (5 km to 72 km) are a product of large-scale meteorological conditions affecting vertical mixing and surface temperatures and salinity, ocean circulation, coastal upwelling, riverine output, eddies and fronts, and internal tides (Ruhl et al., 2011; Schaeffer et al., 2016; Mahadevan and Campbell, 2002). The water column was stratified during R14 due to calm meteorological conditions (average wind speed of $2\,\mathrm{m\,s^{-1}}$ at meteorological buoy M1 - see Fig. 2.1 for location). In contrast, the water column during B16 was mostly well mixed, with later periods of stratification (see Section 3.4). During R14, the surface circulation at depths corresponding to MAW was northward off the shelf, and southward across the shelf slope, and mostly northward at depths corresponding to LIW during R14. Transport varied considerably in the across-shelf direction, with strong eastward or westward currents measured depending on location (Knoll et al., 2017). Surface circulation was mostly west/south-westward during B16 (Fig. 3.1) . Therefore, differences in vertical density, buoyancy gradients, and circulation likely contributed to the differences in horizontal ranges between R14 and B16. The anisotropy found in both R14 and B16 deployments was the same; the horizontal ranges were larger in the zonal direction than in the meridional direction. This could either be related to oceanographic processes in the region, or glider sampling. For R14, this orientation crossed the shelf, whereas for B16, this orientation was off-shelf including a westward-flowing geostrophic current (Millot, 1999; Niewiadomska et al., 2008). Large physical and biogeochemical horizontal ranges can arise as a result of physical flows, such as boundary currents (Schaeffer et al., 2016; Doney et al., 2003). The larger along-current B16 horizontal ranges may be explained by the predominant west / south-westward flow. During R14, the across-shelf flows were considerable (-0.26 Sv to 0.32 Sv) at the glider transect locations (Knoll et al., 2017). However, the larger across-shelf R14 ranges are likely related to there being more overall measurements in the open ocean (158,582 measurements west of 8° E), than on the shelf (84,878 measurements east of 8° E , Fig. 4.6k). Open ocean environments are dominated by large scale processes (Schaeffer et al., 2016). Furthermore, the R14 data gaps along-shelf may have contributed to the smaller spatial scales of variability (Fig. A.6 in the Appendix, Table. 4.2).

$c(O_2)$ and pH_T variability is related (directly or indirectly) to physical processes such as mixing, ocean circulation, and air-sea gas exchange, and biological processes, such as photosynthesis, respiration, grazing, nutrient-cycling, and remineralisation (Ruhl et al., 2011; Schaeffer et al., 2016; Mahadevan and Campbell, 2002). $c(O_2)$ close to the surface is predominantly affected by air-sea gas exchange and therefore should vary on similar scales to surface temperature, as both are influenced by meteorological forcing (Schaeffer et al., 2016). This was the case for R14 across-shelf ranges. A DCM situated at depths of between 30 m and 80 m was present during R14. Phytoplankton distributions are generally fine-scale and patchy because the time for phytoplankton to grow in the presence of nutrients is less than the time for surface temperature to equilibrate with atmospheric forcing (Mahadevan and Campbell, 2002). As this layer is biologically-driven, it could be expected that $c(O_2)$ ranges here would be small. Smaller R14 domain-wide $c(O_2)$ ranges were calculated at these depths when compared with layers directly above and below, but there was no clear reduction at these depths when analysing R14 across- and along-shelf ranges. pH_T is a function of hydrogen ion activity, which is related to the dissociation of carbonate species that when combined form c(DIC) (Zeebe and Wolf-Gladrow, 2001). pH_T variability is mostly affected by photosynthesis and respiration at the surface, altering the carbonate equilibria (Cornwall et al., 2013; Copin-Montégut and Bégovic, 2002), and the effect of CO_2 air-sea gas exchange is small (Fig. 3.17, Mahadevan and Campbell (2002)). pH_T B16 ranges were generally smaller than ranges calculated using other parameters, suggesting that variability was mainly biologically-driven.

The first baroclinic Rossby radius of deformation (R_d) is useful for characterising mesoscale processes on horizontal spatial scales of variability , which depends on the density of the water, latitude, and depth (Chelton et al., 1998). In the Mediterranean Sea, R_d is much smaller than in other ocean regions (generally < 15 km) (Brasseur et al., 1996). Ranges calculated using semivariograms, irrespective of deployment, direction, and the parameter used, were mostly larger than R_d. When comparing both R14 and B16 irrespective of direction, some variable (e.g. $c(\mathrm{O}_2)$, pH_T) ranges were lower than R_d at some depths (e.g. at the surface). The horizontal spatial scales of variability found in the northwestern Mediterranean Sea suggests that physical variability at certain depth levels (e.g. R14 temperature in the top 10 m of the water column, Table. 4.3), were related to local buoyancy effects, but the majority of physical variability at most depths were a result of planetary rotation processes, such as geostrophic currents and eddies.

4.4.3 Sill

The sill (σ^2) represents the point where calculated semivariances plateau. σ^2 can be used to get a sense of the spread of measurements; a higher sill represents a larger spread of measurements. The sill profiles calculated here can be directly compared with time series figures in Chapter 2, and Chapter 3 (Fig. 2.5, Fig. 2.12, Fig. 3.8). R14 temperature, salinity, and $c(\mathrm{O}_2)$ sill profile variations across-shelf, and domain-wide were roughly similar to one another (Fig. 4.6g-i). R14 temperature sills were highest at the surface, decreasing towards and below the thermocline (roughly 100 m depth, Fig. 2.12). R14 salinity sills were highest at the surface, and at depths of between 30 m and 80 m. Greater temperature and salinity variability is generally at depths corresponding to MAW (top 140 m). Here, there are larger spatial temperature and salinity gradients between the open ocean and the shelf (Fig. 2.12, (Knoll et al., 2017)). The greater surface temperature and salinity variability may suggest that meteorological forcing (e.g. air temperature, evaporation) is more important at depths corresponding to MAW than other physical processes. R14 $c(\mathrm{O}_2)$ sills were lower at the DCM (Fig. 2.12), between 30 m and 80 m, and highest between 80 m and 220 m. This suggests that variability is smaller within regimes predominantly affected by biological processes, such as photosynthesis, respiration, zooplankton grazing, and nutrient-cycling. The higher variability below 80 m was situated within the oxycline, which varies horizontally as a function of depth across the Sardinian Sea. Concentrations of $c(\mathrm{DIC})$ were highest here (Fig. 2.5) perhaps indicating increased consumption of $c(\mathrm{O}_2)$ by grazers and remineralisation. The along-shelf temperature, salinity, and $c(\mathrm{O}_2)$ sill profiles varied differently at some depths when compared with the across-shelf and domain-wide sills, such as $c(\mathrm{O}_2)$ below 200 m.

B16 temperature, salinity, and optical backscatter sill profiles were similar along- and across- current, and domain-wide (Fig. 4.7g-i). Temperature and salinity sills were highest within the top 200 m, decreasing to almost zero close to 300 m. These high sills may be explained by the wind-driven mixing that was prominent multiple times over the course of the deployment (Fig. 3.7). Mixed layer depths (Fig. 3.8) varied between 10 m and 200 m during the B16 deployment. Similar to R14, the along-current, across-current, and domain-wide $c(\mathrm{O}_2)$ sills were smaller at the surface and at depth, but larger at intermediate depths between 75 m and 225 m. A DCM was not evident during the B16 deployment as it was Spring, and the water column was mixed. Therefore, nutrients were available at a wider range of depths (Fig. 3.9). On average, the oxycline was situated between 20 m and 300 m depth. The smaller variability within the top 75 m of the water column is related to the highest concentrations of $c(\mathrm{O_2})$ where biological processes and air-sea gas exchange (see Chapter 3) were prominent. Below these depths, remineralisation and grazing would likely be prominent. B16 along-current, across-current, and domain-wide $\mathrm{pH_T}$ sills were highest at the surface, decreasing with depth to very small values close to 300 m. $\mathrm{pH_T}$ variability was high at the surface where the majority of primary production took place (Section 3.4). However, some of this $\mathrm{pH_T}$ variability may be attributed to the temperature and pressure corrections undertaken to correct the raw ISFET $\mathrm{pH_T}$ (Section 3.3.3).

4.4.4 Unresolved Variance

The ratio between the nugget (σ_0^2) and the sill (σ^2) (expressed as a percentage by multiplying by 100) can be used to examine the degree to which the glider resolved variability in the region (Fig. 4.8). Any variability below σ_0^2 has not been resolved by the glider measurements, or has been masked by instrumental noise (Doney et al., 2003). σ_0^2 is obtained from the exponential models where the difference between the two closest measurements is not equal to zero, which occurs at the origin of the semivariogram (Schaeffer et al., 2016). If σ_0^2 is high, a high proportion of the range of variability (i.e. σ^2) has not been observed, and the ratio percentage will be high. In this case, a high proportion of the variance will be unresolved.

Overall, the high-resolution glider measurements resolved a considerable proportion of spatial variability during R14 and B16, as all ratio percentages were generally less than 40 % (excluding across-current and domain-wide optical backscatter at 290 m and 70 m, respectively). Stated differently, in all cases the glider resolved > 60 % of the variance. A number of calculated σ_0^2/σ^2 ratio percentages were close to zero at some depths (e.g. across-shelf $\mathrm{pH_T}$ between 170 m and 300 m) indicating that the glider resolved almost all of the variance. This was the case for $c(\mathrm{O_2})$, $\mathrm{pH_T}$, salinity, and temperature during R14 and B16 on various orientations. It seemed that more measurements might be needed in future to reduce the ratio percentages further at depths where ratio percentages were high and the r-squared statistics were low. For comparison, Schaeffer et al. (2016) found much lower σ_0^2/σ^2 ratio percentages when performing a similar analysis to this study. They used measurements from 23 glider deployments sampling in zig - zag patterns across a dynamic shelf region over a period of 6 years.

Table 4.3: The average ranges, r-squared statistics, and sill / nugget ratios (σ_0^2/σ^2) as percentages for temperature, salinity, and dissolved oxygen concentrations ($c(O_2)$) for four different depth ranges: 0 m - 10 m, 10 m - 50 m, 50 m - 100 m, and 100 m - 300 m, using distances along different orientations (across-shelf, along-shelf, and domain-wide) measured during REP14 - MED (R14). Missing information is associated with excluded semivariograms with low exponential fits (r-squares < 0.2).

			Temperature	Salinity	$c(O_2)$
Across-shelf	0-10m	range	5 km	45 km	2 km
		r^2	0.64	0.62	0.26
		σ_0^2 / σ^2	9%	24%	17%
	10-50m	range	28 km	18 km	24 km
		r^2	0.73	0.57	0.48
		σ_0^2 / σ^2	14%	21%	23%
	50-100m	range	23 km	27 km	14 km
		r^2	0.67	0.81	0.51
		σ_0^2 / σ^2 %	8%	8%	18%
	100-300m	range	29 km	28 km	21km
		r^2	0.43	0.57	0.45
		σ_0^2 / σ^2	21%	14%	9%
Along-shelf	0-10m	range	-	6 km	3 km
		r^2	-	0.22	0.80
		σ_0^2 / σ^2	-	1%	16%
	10-50m	range	-	-	5 km
		r^2	-	-	0.33
		σ_0^2 / σ^2	-	-	21%
	50-100m	range	-	9 km	5 km
		r^2	-	0.21	0.36
		σ_0^2 / σ^2	-	1%	7%
	100-300m	range	17 km	18 km	6 km
		r^2	0.41	0.27	0.44
		σ_0^2 / σ^2	8%	14%	3%
Domain-wide	0-10m	range	19km	60 km	-
		r^2	0.57	0.38	-
		σ_0^2 / σ^2	17%	25%	-
	10-50m	range	31 km	28 km	40 km
		r^2	0.46	0.53	0.43
		σ_0^2 / σ^2	10%	18%	15%
	50-100m	range	18 km	27 km	34 km
		r^2	0.48	0.55	0.55
		σ_0^2 / σ^2	0%	0%	4%
	100-300m	range	36 km	34 km	43 km
		r^2	0.57	0.52	0.45
		σ_0^2 / σ^2	1%	5%	1%

Table 4.4: The average ranges, r-squared statistics, and sill / nugget ratios (σ_0^2/σ^2) as percentages for temperature, salinity, dissolved oxygen concentrations ($c(O_2)$), pH_T, and optical backscatter for four different depth ranges: 0 m- 10 m, 10 m- 50 m, 50 m- 100 m, and 100 m- 300 m, using distances along different orientations (across-shelf, along-shelf, and domain-wide) measured during BOUSSOLE (B16). Missing information is associated with excluded semivariograms with low exponential fits (r-squares < 0.2).

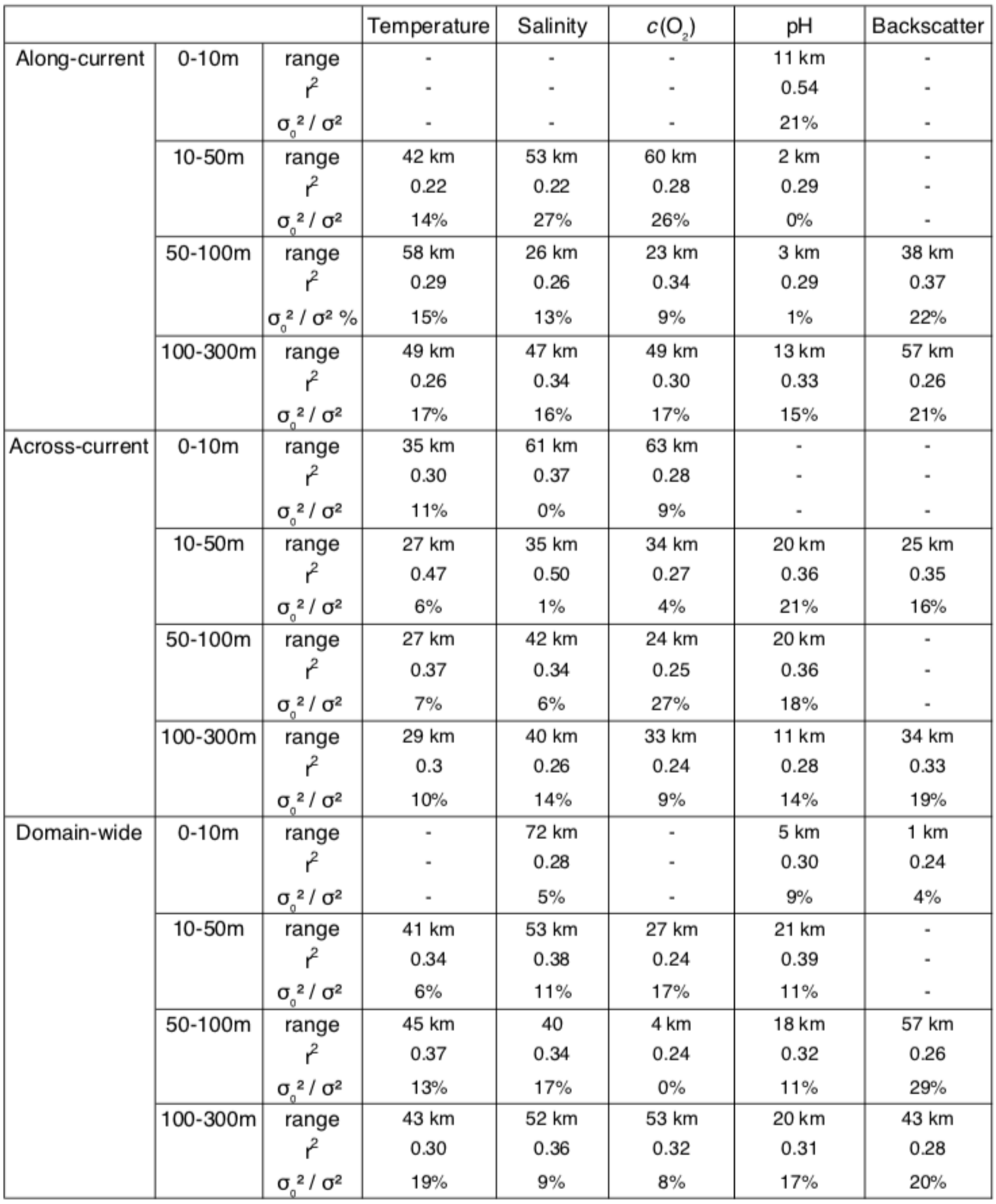

			Temperature	Salinity	$c(O_2)$	pH	Backscatter
Along-current	0-10m	range	-	-	-	11 km	-
		r^2	-	-	-	0.54	-
		σ_0^2 / σ^2	-	-	-	21%	-
	10-50m	range	42 km	53 km	60 km	2 km	-
		r^2	0.22	0.22	0.28	0.29	-
		σ_0^2 / σ^2	14%	27%	26%	0%	-
	50-100m	range	58 km	26 km	23 km	3 km	38 km
		r^2	0.29	0.26	0.34	0.29	0.37
		σ_0^2 / σ^2 %	15%	13%	9%	1%	22%
	100-300m	range	49 km	47 km	49 km	13 km	57 km
		r^2	0.26	0.34	0.30	0.33	0.26
		σ_0^2 / σ^2	17%	16%	17%	15%	21%
Across-current	0-10m	range	35 km	61 km	63 km	-	-
		r^2	0.30	0.37	0.28	-	-
		σ_0^2 / σ^2	11%	0%	9%	-	-
	10-50m	range	27 km	35 km	34 km	20 km	25 km
		r^2	0.47	0.50	0.27	0.36	0.35
		σ_0^2 / σ^2	6%	1%	4%	21%	16%
	50-100m	range	27 km	42 km	24 km	20 km	-
		r^2	0.37	0.34	0.25	0.36	-
		σ_0^2 / σ^2	7%	6%	27%	18%	-
	100-300m	range	29 km	40 km	33 km	11 km	34 km
		r^2	0.3	0.26	0.24	0.28	0.33
		σ_0^2 / σ^2	10%	14%	9%	14%	19%
Domain-wide	0-10m	range	-	72 km	-	5 km	1 km
		r^2	-	0.28	-	0.30	0.24
		σ_0^2 / σ^2	-	5%	-	9%	4%
	10-50m	range	41 km	53 km	27 km	21 km	-
		r^2	0.34	0.38	0.24	0.39	-
		σ_0^2 / σ^2	6%	11%	17%	11%	-
	50-100m	range	45 km	40	4 km	18 km	57 km
		r^2	0.37	0.34	0.24	0.32	0.26
		σ_0^2 / σ^2	13%	17%	0%	11%	29%
	100-300m	range	43 km	52 km	53 km	20 km	43 km
		r^2	0.30	0.36	0.32	0.31	0.28
		σ_0^2 / σ^2	19%	9%	8%	17%	20%

4.5 Comparison With Previous Studies

Schaeffer et al. (2016) calculated semivariograms between 29° S and 34° S off the eastern coast of Australia. This region has an R_d of between 10 km and 15 km, which is similar to

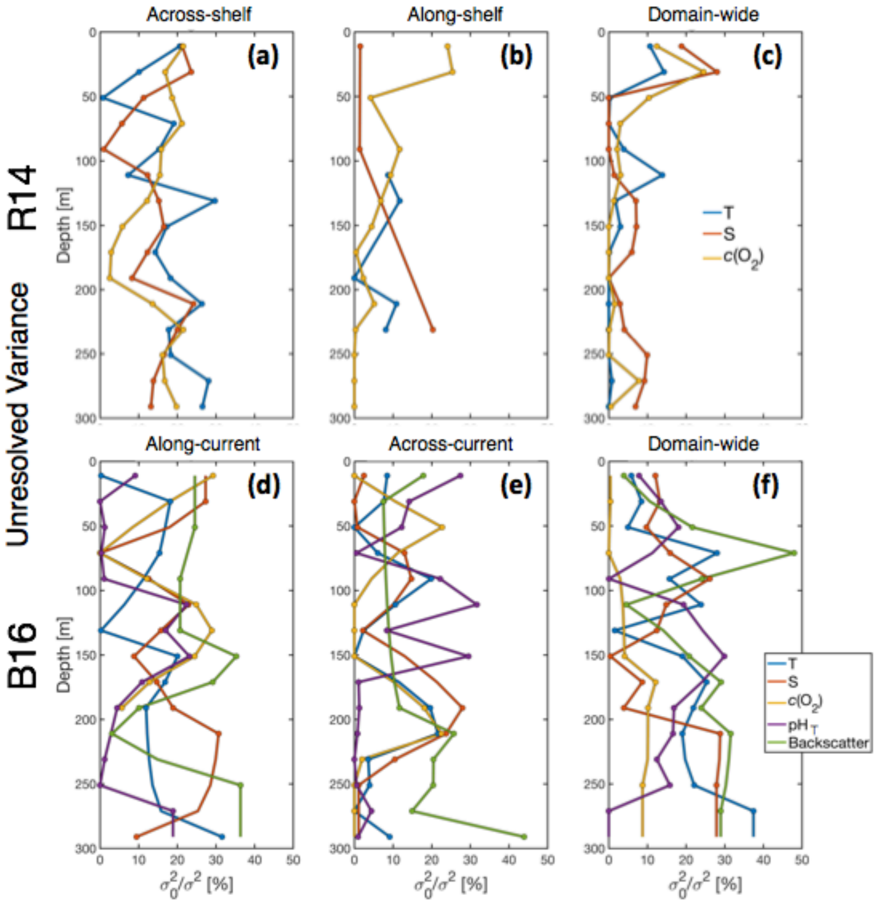

Figure 4.8: The calculated nugget / sill ratios (σ_0^2/σ^2) as percentages for temperature (blue), salinity (red), dissolved oxygen concentrations ($c(O_2)$, yellow), pH$_T$ (purple), and optical backscatter (green) using across-shelf distances, along-shelf distances, and domain-wide distances during REP14 - MED (R14) (a-c), and during BOUSSOLE (B16) (d-f).

the northwestern Mediterranean Sea (< 15 km). Schaeffer et al. (2016) found temperature, salinity, and $c(O_2)$ ranges within the top 50 m of between 14 km and 37 km, 10 km and 15 km, and 8 km and 35 km, respectively. The majority of ranges calculated in this study are either smaller, or larger than the ranges in that study, but generally of the same order of magnitude. The majority of fits obtained by Schaeffer et al. (2016) had higher r^2 statistics (e.g. temperature fits > 0.9) than in this study, perhaps because they used a higher number of glider measurements or that the spatial distribution was better. The spatial characteristics obtained from their semivariograms are more robust than the ones obtained in this study. Doney et al. (2003) calculated semivariograms globally using satellite-derived surface ocean colour data (9 km x 9 km nominal resolution) in 1998. They found horizontal ranges between some 10s km and 350 km depending on location and orientation, although they could not characterise variability on scales < 15 km. Temperature ranges in this chapter (R14: 5 km to 36 km, B16: 27 km to 58 km) are generally of the same order of magnitude as ranges derived using satellite SST in the

Malvinas current region (20 km to 47 km, Tandeo et al. (2014)), and those derived using glider measurements in the Mid Atlantic Bight region (10 km to 35 km, Todd et al. (2013)). There was a directional difference (or anisotropy) in R14 and B16 horizontal ranges. This is consistent with previous studies that found anisotropy (e.g. Schaeffer et al. (2016), Jones et al. (2015), Oke and Sakov (2012), Doney et al. (2003)). However, due to data limitations, Oke and Sakov (2012) and Jones et al. (2015) could only examine broad scale (>15 to 40 km and > 40 km, respectively) processes.

4.6 Designing an Observing System

Semivariogram horizontal ranges are useful for designing observing systems. It is important to observe oceanographic biogeochemical and physical parameters on a range of scales of variability in order to capture key features and processes. The σ_0^2/σ^2 ratio percentages calculated for R14 and B16 in the northwestern Mediterranean Sea suggest that variability was best captured by the gliders at certain depths (e.g. across-shelf $c(O_2)$ between 150 m and 200 m). The small ranges calculated for $c(O_2)$, and pH_T at some depths (e.g. surface R14 across-shelf $c(O_2)$, surface B16 domain-wide pH_T) suggest that a high density of measurements might be needed to adequately resolve their variability, compared with other parameters (e.g. temperature). To ensure that physical and biogeochemical variability is adequately captured, and to improve overall σ_0^2/σ^2 ratio percentages , the number of underwater gliders used for one transect line could be increased. However, this is more costly, and would depend on research objectives. Increasing the density of measurements along transects (i.e. by performing steeper dives with closer surfacing points) would increase the spatial resolution, whilst increasing the number of gliders along transects would increase the temporal resolution (i.e. by repeatedly sampling similar locations in time). Increasing the density of measurements, and the number of gliders along transects would be useful for studies focussing on sub-mesoscale processes (e.g. physical-biological interactions, internal tides, coastal upwelling etc.).

Glider measurements complement other (sometimes spatially-isolated) observing platforms by providing more information in space and time in the same area. Close to the DyFAMed site, measurements are collected hourly at fixed depths on a buoy, and monthly by ship. Knowing scales of variability in this region allows the planning of glider sampling patterns. Spatial scales of variability were often smaller for parameters directly or indirectly affected by biological activity in the water, and larger for parameters affected by physical processes. Therefore, in order to relate glider measurements to the buoy and ship measurements in this region, careful planning must ensure that glider sampling adequately resolves the scales of variability. If the key objectives of the observing system involve biogeochemical processes, it is required that the glider samples within a short distance to the buoy and ship casts, or that more gliders are deployed at the same time, as the scales of variability are often small.

However, if the key objectives involve physical processes, the glider may sample further away from the buoy and ship casts, as long as it remains within the range of variability.

Ranges were larger zonally (R14: across-shelf, B16: along-current), than meridionally (R14: along-current, B16: across-current). Assuming that this anisotropy is related to oceanographic processes, rather than an artefact of the sampling, future observing system designers investigating this region could increase the meridional density of zonal transects across the shelf, or could undertake meridional transects, separated by zonal distance. Increasing the number of transects in this way would provide improved resolution to capture smaller scale variability. In future, it would also be beneficial to characterise spatial scales of variability over time, to determine the corresponding temporal scales of variability. Obtaining temporal scales of variability will determine which temporal patterns are dominant at certain depths.

4.7 Conclusion

The characterisation of horizontal spatial scales of variability in the northwestern Mediterranean Sea was achieved using glider measurements obtained during two deployments: one in the Sardinian Sea in June 2014 (REP14 - MED), and one close to the BOUSSOLE biogeochemical buoy in March-April 2016. Horizontal spatial scales of variability were calculated using two physical parameters (temperature and salinity), and three biogeochemical parameters ($c(\mathrm{O_2})$, pH, and optical backscatter). Semivariograms were used to derive the scales of variability by determining the average dissimilarity between data points as a function of the distance between them. Exponential models were fit to the semivariograms to extract the σ_0^2, σ^2, and r components.

The influence of certain processes on key physical and biogeochemical parameters has been highlighted using the three semivariogram components. The spatial scales of variability (i.e. r) were mostly small at depths affected by photosynthesis (e.g. $\mathrm{pH_T}$, $c(\mathrm{O_2})$) and large at depths affected by large-scale processes, such as atmospheric forcing (e.g. temperature). This was however not universal to every orientation and dataset, and in some cases the opposite could be seen (e.g. $c(\mathrm{O_2})$ R14 domain-wide). Differences between r calculated using R14 and B16 measurements was likely related to the differences in vertical density, buoyancy gradients, and circulation. During R14 the water column was stratified and the circulation was either northward / southward depending on the location, whereas during B16 the water column was mostly mixed and the circulation was mostly south / south-westward. The spatial scales of variability were mostly larger than the Rossby radius of deformation (generally < 15 km), irrespective of deployment, direction, and parameter used. This suggested that physical variability at most depths were a result of planetary rotation processes, such as geostrophic currents and eddies.

There was some anisotropy, as semivariograms calculated using zonal distances were mostly larger than those calculated using meridional distances. This anisotropy may be related to the ocean currents. Large physical and biogeochemical horizontal scales of variability can arise as a result of physical flows, such as boundary currents (Schaeffer et al., 2016; Doney et al., 2003). The large along-current B16 spatial scales of variability may be explained by the west/south-westward flow. Otherwise, this anisotropy may be related to the glider sampling patterns, particularly when considering R14 meridional measurements.

σ^2 can be used to get a sense of the spread of measurements used for the semivariogram. Using σ^2, the spread of measurements as a function of depth were linked to water masses, and physical and biogeochemical processes. During R14, high temperature and salinity σ^2 were found at depths corresponding with MAW, and at the surface, which may be related to meteorological forcing. $c(O_2)$ σ^2 were low at the DCM during R14, possibly because of increased biological activity there. During B16, temperature and salinity σ^2 were high in the top 200 m of the water column, likely related to mixing. Small $c(O_2)$ σ^2 were low where the highest $c(O_2)$ were found, and where biological processes and air-sea gas exchange were prominent. High pH_T σ^2 were found close to the surface, which may be related to biological productivity.

Overall, the models used to extract the spatial characteristics did not perform as well as in other studies (e.g. Schaeffer et al. (2016)), particularly for B16. Spatial scales of variability are useful in the design of observational glider campaigns, and future glider campaigns that study sub-mesoscale processes in the northwestern Mediterranean Sea must aim to resolve the small horizontal spatial scales of variability that characterise physical and biogeochemical processes in this region.

5

Thesis Summary and Outlook

5.1 The Implementation of an Experimental pH Sensor on an Underwater Glider

5.1.1 Key Findings

Two non-commercially available experimental ion sensitive field effect transistor (ISFET) pH - $p(CO_2)$ sensors were attached to an underwater glider during the REP14 - MED experiment; one dual sensor was stand-alone, and the other dual sensor was integrated into the glider electronics. Data retrieved from the dual pH - $p(CO_2)$ glider-integrated sensor, and from the $p(CO_2)$ unit of the stand-alone sensor could not be used due to quality issues.

Data retrieved from the stand-alone pH sensor was corrected following a number of procedures. The pH data were subject to multidirectional residual drift after initially correcting for linear drift using TRIS and AMP buffer solutions before and after the deployment. A depth-constant time-varying offset was applied to each dive to correct for this multidirectional drift. These offsets were calculated using the difference between ship and glider pH at a more dynamically stable depth where the temperature of the water was 14 °C.

It seemed temperature and pressure had an effect on pH observed by the stand-alone sensor. Studies have shown that it is possible for ISFET sensors to experience some issues due to varying temperature and pressure. This temperature and pressure effect was unexpected as the sensor had previously shown good temperature and pressure characteristics. The stand-alone pH measurements were corrected for temperature and pressure using the relationships with ΔpH (the differences between glider and ship pH).

The stand-alone ISFET pH sensor was affected by light. pH anomalies were as much as 0.1 lower around the time of maximum sunlight irradiance. This light effect was also found when testing the pH stand-alone sensor in reference buffer solution using LED and halogen lights in the laboratory.

The BOUSSOLE deployment offered a second trial of the experimental ISFET dual pH - $p(CO_2)$ sensors. Both the stand-alone and integrated dual sensors were positioned on the underside of the glider to limit the effect of sunlight on measurements, and backup batteries were provided to supply power in between sampling, as recommended above. Unfortunately the stand-alone dual pH - $p(CO_2)$ sensor ceased operating early into the deployment because of an issue with its power supply. For this reason, pH obtained by the glider-integrated dual pH - $p(CO_2)$ sensor was used. Once again, there was an issue with the stability of the $p(CO_2)$ sensors, therefore limiting the usefulness of $p(CO_2)$ measurements. Similarly to the REP14 - MED trial, the glider-integrated pH sensor suffered from linear and multi-directional drift, and experienced apparent temperature and pressure effects. The methods of correcting the glider pH measurements during the BOUSSOLE deployment were similar to those applied to REP14 - MED measurements. The temperature and pressure slope coefficients used to correct the glider pH were of similar magnitude for both the REP14 - MED and BOUSSOLE trials. Considering that each trial occurred at a different location, a different time of the year, and in vastly different environments (i.e. mixing vs. stratification), the similar slope coefficients suggest that the derived ISFET pH sensor corrections are applicable to a wide range of situations.

The potential use of the corrected glider pH measurements for uncovering biogeochemical and physical variability was explored. For REP14 - MED measurements, a link between the corrected pH and biological activity was made. In the top 100 m of the water column, pH was high where dissolved oxygen concentrations ($c(O_2)$) were high. This was particularly clear at the depth of the DCM. Low pH was found in the western part of the glider transects, which may have been a result of the remineralisation of organic matter. High pH in the eastern part of the glider transects may have been transported from the eastern Mediterranean Sea where pH is generally higher. Closer to shore, shoaling isopycnals and low salinity, temperature, pH, $c(O_2)$, concentrations of dissolved inorganic carbon (c(DIC)), total alkalinity (A_T), and chlorophyll fluorescence in shallow waters may have been indicative of upwelling. At BOUSSOLE, the corrected pH measurements were useful as indicators of primary production, for deriving c(DIC) using A_T and the program CO2SYS, and for estimating spatial scales of variability.

5.1.2 Lessons Learnt and Future Improvements

The results were initially disappointing, and it is clear from these trials that the procedure of attaching ISFET sensors to underwater gliders still requires some development. However, by correcting the pH measurements, the potential usefulness of deploying ISFET sensors was illustrated.

The stability of the glider-integrated and stand-alone $p(\mathrm{CO_2})$ ISFET sensors was poor. It is unclear why there was a problem with these measurements. However, the stability of the sensors may in part be related to the gas-permeable membrane. To measure $p(\mathrm{CO_2})$, the pH of the water is measured within a gas permeable membrane filled with an inner solution. Variations in the pH of this inner solution is related to the penetration of $\mathrm{CO_2}$ through the membrane, and is used to derive $p(\mathrm{CO_2})$. It may have been the case that the diffusion of $\mathrm{CO_2}$ across or within the membrane was highly variable. Furthermore, relating to the glider-integrated dual ISFET pH - $p(\mathrm{CO_2})$ sensor, it was thought that there was an issue with the electricity supply from the glider. It was thought that the regular on / off cycling of power to the integrated sensor in between sampling did not allow it to function properly. The addition of backup batteries to supply the integrated sensor in between sampling was tested during the BOUSSOLE deployment. This worked for the glider-integrated ISFET pH sensor. However, the glider-integrated ISFET $p(\mathrm{CO_2})$ sensor still encountered stability issues. The cause of this is unclear.

Due to thesis time constraints and the poorer quality $p(\mathrm{CO_2})$ measurements, the method of converting raw ISFET $p(\mathrm{CO_2})$ counts (corresponding to the inner-membrane solution pH) to quantitative $p(\mathrm{CO_2})$ units was not explored. In previous work, raw ISFET $p(\mathrm{CO_2})$ counts were used to provide qualitative discussion only (e.g. Shitashima et al. (2013, 2008)). In future, a method using reference solutions of known $p(\mathrm{CO_2})$ to calibrate $p(\mathrm{CO_2})$ counts before and after the deployment could be developed.

The stability of the stand-alone ISFET pH sensor was poor. The multi-directional drift was inconsistent over time and spatially-independent. It was clear that this multi-directional drift was related to an issue with the ISFET sensor, rather than the environmental conditions at the time. It is thought that a change in the interface potential (E^*) between the two n type silicon parts of the semiconductor might be responsible for this drift. To elucidate this drift further, in future two ISFET sensors should be tested in laboratory conditions within a bridge circuit to attempt to isolate possible factors contributing to drift. Focussing on the root cause of the sensor drift, rather than correcting the pH data for drift after the deployment, would be more beneficial to the longterm study of ISFET pH-$p(\mathrm{CO_2})$ sensors. It is also possible that the limited pre-conditioning of the sensor in local seawater caused the sensor to drift during the deployment. Pre-conditioning an ISFET sensor prior to a deployment limits the effect of bromide on sensor performance, and an asymptotic drift can be experienced when the sensor is in contact with water. Such drifts usually last a couple of days. The ISFET stand-alone pH sensor was preconditioned for one hour only due to time constraints, although pre-conditioning is recommended for some weeks. In future, it is recommended to pre-condition the sensor for at least one week prior to a deployment.

The sensor was apparently affected by temperature and pressure during the REP14 and BOUSSOLE deployments. It is unclear to what extent the empirical relationship between *insitu* temperature, pressure and pH can be generalised. To explore these relationships further, it is recommended to follow similar steps to those described by Johnson et al. (2016). Their ISFET DuraFET sensor was tested for its response to temperature and pressure changes using a custom-built titanium chamber. The sensor was calibrated by cycling through the typical range of temperature and pressure that may be experienced by the sensor when in the field.

The effect of light on the ISFET pH - $p(CO_2)$ sensor was unexpected. This effect had not been highlighted in previous work (e.g. Shitashima et al. (2013, 2008)), as the focus had been on observing deep measurements (e.g. monitoring seabed CO_2 leakages) on shorter timescales. It was suggested for the BOUSSOLE trial to either surround the sensors with a light shield or to place the sensors on the underside of the glider. Placing the sensor on the underside of the glider during the BOUSSOLE deployment significantly limited the affect of light on pH measurements.

The development of the ISFET pH - $p(CO_2)$ sensor during the course of this study was limited due to practical issues. The sensors were loaned to the University of East Anglia for the duration of the deployments, and for a period of two days in the laboratory. This meant that it was not possible to explore the issues raised in this work further over a longer time period in the laboratory at the University of East Anglia. Due to this limitation, it was also not possible to pre-condition the sensors for a longer time period prior to the deployments.

At the current stage of development, the ISFET pH - $p(CO_2)$ sensor can be used on autonomous platforms to measure pH in the Mediterranean Sea and globally. However, time should be invested to properly pre-condition the sensor before deployment, and to collect reference ship pH samples to deal with likely instrumental issues. Although the calibration equations derived using the relationship between pH and temperature, and pH and pressure in the northwestern Mediterranean Sea worked in reducing the large range of variability associated with instrumental issues, it is unclear whether they could be applied to pH measurements obtained in other regions. However, considering that each trial occurred at a different location, a different time of the year, and in vastly different environments (i.e. mixing vs. stratification), the similar slope coefficients suggest that the derived ISFET pH sensor corrections are applicable to a wide range of situations. Unless improvements are made to the experimental ISFET pH - $p(CO_2)$ sensor used in this study, it is suggested that those wishing to measure *insitu* pH autonomously with high spatial and temporal resolution as part of an established observing program explore other ISFET technologies. For example, Saba et al. (2018) used a Deep-Sea ISFET sensor attached to a Slocum glider to measure pH in the Mid-Atlantic Bight. Although the instrument experienced a time lag that required correcting, glider and ship pH measurements were in good agreement at some depths and times.

The majority of past studies on pH variability used fixed-location time series globally (e.g. Hofmann et al. (2011)) and in the northwestern Mediterranean Sea (e.g. Copin-Montégut and Bégovic (2002)). Such studies provide the typical range in pH that can be experienced at certain depths and times, but lack detail in horizontal space. Ship-based studies (e.g. Álvarez et al. (2014)) measure pH variability in both vertical and horizontal space, but are limited by the sparsity of profiles in time and horizontal space. The pH variability presented in this thesis has a higher resolution than previous studies, both in horizontal and vertical space, and in time. It was the first time that pH measurements have been made in the Sardinian Sea (Álvarez et al. (2014) measured pH south of Sardinia) and across the wider DyFAMed area. The high-resolution pH measurements in the northwestern Mediterranean Sea were used to identify different water masses in vertical and horizontal space over time, and links could be made with biogeochemistry (e.g. primary production, remineralisation, etc.) and physical processes (e.g. upwelling, circulation, etc.).

5.2 Net Community Production

5.2.1 Key Findings

Deploying an underwater glider close to a buoy provides further context of the wider region conditions during the time of a Spring bloom. The BOUSSOLE buoy measurements at 10 m depth suggested that the spring bloom started on March 19. This was the point in which the fugacity of CO_2 ($f(CO_2)$) started to decrease, wind speeds decreased, and SST started to increase. Over the same time period and at the same depth, glider salinity started to decrease, whilst biologically-related parameters pH, $c(O_2)$, and optical backscatter, started to increase. Using glider measurements, the mixed layer depth (MLD) could be estimated before and during the spring bloom. MLDs were deeper before March 19. This suggested that wind-driven mixing pre-conditioned the upper water column prior to the spring bloom, evidenced by the higher nutrient concentrations, relatively constant buoy SST, and increasing buoy $f(CO_2)$ and glider salinity.

Glider $c(O_2)$ were useful for comparing with the calibrated glider pH, and for estimating net community production (N). Although Aanderaa $c(O_2)$ sensors have been on the market for a number of years, there is still a need for user-level calibration. This was apparent for $c(O_2)$ observations during both the REP14 - MED and BOUSSOLE deployments. In both cases, the glider $c(O_2)$ were calibrated to take into account the response time of the sensor (dependent on its foil), and to account for the difference between the glider and ship measurements, which was more prominent in the top 300 m of the water column.

N was estimated using glider $c(O_2)$ and derived $c(\mathrm{DIC})$, and buoy derived $c(\mathrm{DIC})$. Glider N was estimated using mass budgets taking into account physical fluxes relating to horizontal advection, air-sea exchange, and mixing. The horizontal gradients in $c(O_2)$ and $c(\mathrm{DIC})$ observed by the glider across the domain allowed the estimation of advection. N_{O_2} estimated using glider $c(O_2)$ and derived $c(\mathrm{DIC})$ ranged between -82 mmol m^{-2} d^{-1} and 448 mmol m^{-2} d^{-1} between March 10 and April 3. N_{O_2} estimated between March 20 and April 1 at the buoy ranged between 207 mmol m^{-2} d^{-1} and 238 mmol m^{-2} d^{-1} when excluding advection, but between 284 mmol m^{-2} d^{-1} and 460 mmol m^{-2} d^{-1} when including advection. The mean N fluxes estimated using $c(\mathrm{DIC})$ suggest net photosynthesis, whilst the mean N fluxes estimated using $c(O_2)$ suggest net respiration, which is unlikely in spring.

When combining the error associated with each individual flux estimate together, the total uncertainty was large for N_{g,O_2}, $N_{\mathrm{g,DIC}}$, and $N_{\mathrm{b,DIC}}$. The largest sources of error were associated with inventory change and advection. Although the N estimated by Copin-Montégut (2000) and Coppola et al. (2018) lay within the range of N estimated in this study, the corresponding N uncertainty limited a meaningful comparison.

5.2.2 Lessons Learnt and Future Improvements

The glider measurements could only be compared with buoy measurements when the glider was close (generally < 10 km). This limited the frequency of comparisons between glider and buoy measurements, useful for calibrating the glider sensors, and determining the timing of the spring bloom. In future, it would be better to set the glider way points used to complete the glider surveying pattern in a way that would benefit glider-buoy comparisons, whilst ensuring horizontal gradients are measured over a suitable range (i.e. greater than the Rossby Radius) used to estimate advection. For example, larger diamond patterns could be completed every even numbered survey, whilst smaller diamond patterns closer to the buoy could be completed every odd numbered survey. This would ensure that the larger horizontal gradients are measured typically every 2 days, whilst more data points are collected closer to the buoy. Another example could be a butterfly glider-observing pattern, similar to that used by Alkire et al. (2014). Transect lines within the butterfly pattern could cross the domain close to the buoy. The ideal scenario, however, would be to deploy an extra glider. One glider could survey the wider area to obtain the horizontal gradients, whilst the second glider could encircle the buoy.

A constant problem during this study related to the erroneous raw glider $c(O_2)$ measurements. The glider $c(O_2)$ N (N_{g,O_2}) estimated in this thesis depended on the quality of the glider $c(O_2)$ measurements. The glider $c(O_2)$ measurements were corrected for a time lag effect, and were corrected to account for the difference between the glider $c(O_2)$ measurements and ship $c(O_2)$ measurements. In future, it would be beneficial to add a second $c(O_2)$ sensor to the glider which would provide a further comparison. Furthermore, if a $c(O_2)$ sensor was positioned towards the rear of the glider, similar to the method described by Bittig and Körtzinger (2015) on Argo floats, measurements obtained near-surface / in-air when the glider surfaces could be used to correct for drift. This would be useful for ensuring correct glider $c(O_2)$ measurements over the duration of the deployment.

Each flux used to calculate N had some degree of uncertainty. When combined, the total uncertainty was large for N_{g,O_2}, the glider c(DIC) N ($N_{g,DIC}$), and the buoy c(DIC) N ($N_{b,DIC}$). The largest sources of error were associated with inventory change and advection. The general patterns of glider $c(O_2)$ and c(DIC) over time were relatively consistent across the domain, however, there were at times significant spatial contrasts. This suggests that the scale of horizontal variability in $c(O_2)$ and c(DIC) may at times be small (although not evidenced in the euphotic depth in Chapter 4). The errors associated with the advection and inventory change fluxes were calculated using the standard deviation of measurements across the domain within the euphotic depth (z_{eu}) for a given time step, multiplied by z_{eu}. Such errors may be reduced in future if a second glider was deployed. The addition of more glider measurements across the domain could offer a better glimpse of the conditions at the time, confining the mean horizontal gradient and reducing the root mean squared error and standard deviation.

5.3 Spatial Scales of Variability

5.3.1 Key Findings

Horizontal spatial scales of variability were estimated in the northwestern Mediterranean Sea using glider measurements obtained during the REP14 - MED and BOUSSOLE deployments. The horizontal scales of variability highlight the influence of certain processes on key physical and biogeochemical parameters. Semivariograms were used to determine the average dissimilarity (or semivariance) between data points as a function of the distance between them. Horizontal spatial scales of variability were determined by fitting exponential models to the semivariances. A range of models were tested, but the coefficient of the determination (r^2) values calculated using the exponential fit were highest.

Overall, the performance of the exponential models was poor. r^2 values were generally low, although the r^2 was greater than 0.7 at some depths. The horizontal spatial scales of variability (defined as *r* using the exponential fits) were mostly small at depths affected by photosynthesis, and large at depths affected by large-scale processes, such as atmospheric forcing. Although this wasn't consistent in every direction (meridional, zonal, domain-wide), and varied per glider deployment. The horizontal spatial scales of variability found in the northwestern Mediterranean Sea were mostly larger than the first baroclinic Rossby radius of deformation irrespective of direction, deployment, and the parameter used. This suggested that the majority of physical variability was a product of planetary rotation processes, such as geostrophic currents and eddies. There was some anisotropy (i.e. direction-dependency), as semivariograms calculated using zonal distances were larger than those calculated using meridional distances. This anisotropy may be related to ocean currents, or instead may be related to the glider sampling pattern (e.g. REP14 - MED meridional sampling distribution). The sills derived from the semivariogram exponential models indicated the relative magnitude of variability at different depths. In some cases, the sills might be explained by physical (e.g. mixing) and biogeochemical (e.g. biological activity at the DCM) processes. The unresolved variance, estimated using the ratio percentage between the nugget and sill, was generally less than 40 %, indicating that the glider measurements resolved a considerable proportion of spatial variability in the northwestern Mediterranean Sea.

5.3.2 Lessons Learnt and Future Improvements

Although the spatial scales of variability obtained in this thesis may be useful for designing observational systems, the available data could be used further. Data collected by all eleven REP14 - MED gliders could be used to derive horizontal spatial scales of variability, which may improve the robustness of the REP14 - MED meridional spatial semivariogram components (e.g. r^2). The transects used to calculate semivariograms could be split into on- and off-shelf sections during REP14 - MED to explore the effect of shelf and open ocean processes on horizontal ranges. Furthermore, horizontal ranges calculated using surface satellite measurements could be compared with horizontal ranges calculated using surface glider measurements, and temporal scales of variability could be calculated using different ocean parameters at different depths. It was not possible to undertake this work due to the time constraints of the thesis. However if undertaken in future, there is potential to improve the discussion of the horizontal scales of physical and biogeochemical variability in the northwestern Mediterranean Sea.

5.4 A Full Perspective

5.4.1 Overall

The world's oceans are becoming increasingly acidic as a result of absorbed atmospheric anthropogenic CO_2 in the ocean. Decreasing ocean pH has the potential to affect calcifying organisms, such as marine algae and reef-building corals, due to changes in seawater carbonate chemistry (Doney et al., 2009). Obtaining measurements of ocean pH that are both accurate and precise, in the laboratory and in the field, is challenging due to the scale in which pH varies in space and time. Exploring how pH varies in the ocean with high spatial and temporal resolution improves our understanding of how future ocean acidification may impact marine ecosystems. The experimental ISFET dual pH - $p(CO_2)$ sensor was used in an attempt to measure acidification-related ocean properties. Although there were problems with the sensor during the trials, corrections were applied, and ocean pH variability was presented in high-resolution, uncovering the biogeochemical variability associated with biological and physical features in the northwestern Mediterranean Sea. The experimental ISFET sensor requires a number of modifications and careful planning in future to capture pH variability with higher accuracy and precision.

The amount of absorbed CO_2 in the ocean is related to physical processes, such as air-sea gas exchange and mixing, and biological activity (Raven et al., 2005). Estimates of net community production (N) are useful for quantifying the production of organic carbon from CO_2 in the water column. Changes in N, particularly during times of phytoplankton blooms, influence the vertical export of carbon to depth (Alkire et al., 2014). This study presented the first estimates of N in the northwestern Mediterranean Sea using both glider and buoy measurements before and during a spring bloom. Some N estimates were surprising, when considering that negative values were calculated (i.e. respiration was dominant during the spring bloom), and the overall errors associated with the glider N estimates were large. However in spite of this, a method has been presented that can be worked on by others in the research community, and some suggestions to reduce the overall uncertainty have been provided (Section 5.2.2).

Understanding and projecting the impacts of a changing climate on the ocean requires high-resolution ocean data. Quantifying spatial scales of variability is useful in the design of underwater glider observational campaigns that capture climate-related features and processes in high-resolution, and aid the development of models (Schaeffer et al., 2016). The spatial scales of variability estimated using semivariograms in this study varied with depth, the parameter that was used, and direction, which was likely related to physical and biogeochemical processes, and the sampling pattern of the data. The fits used to extract the spatial scales of variability were poor and improvements to the method (Section 5.3.2) should be made in future.

5.4.2 Potential Impacts of This Study

The results presented in this thesis, and the related contributions have led to three peer-reviewed publications: Hemming et al. (2017), Knoll et al. (2017) and Onken et al. (2018), and Chapter 3 is currently in preparation to be submitted as a research paper. Future studies planning to use ISFET sensor technology on underwater gliders can refer to the evidence of light, temperature, and pressure effects on ISFET pH measurements in this thesis. The calibration procedure discussed in Chapter 2 may be helpful in determining the calibration of other ISFET sensors. The estimates of N in Chapter 3 can be compared with future estimates of N at the same region, and the high-resolution information obtained by the glider at the BOUSSOLE site provides context to future studies in the region. We now have more information of the physical and biogeochemical variability leading up to, and proceeding, a spring bloom at the BOUSSOLE site. The horizontal spatial scales of variability estimated in Chapter 4 could be useful for future experiment planning, or the designing of observing systems in the northwestern Mediterranean Sea.

References

Aanderaa, October 2016. URL `https://www.aanderaa.com/media/pdfs/oxygen-optode-4330-4330f.pdf`.

Alkire, M. B., D'Asaro, E., Lee, C., Perry, M. J., Gray, A., Cetinić, I., Briggs, N., Rehm, E., Kallin, E., Kaiser, J., et al. Estimates of net community production and export using high-resolution, Lagrangian measurements of O_2, NO_{3-}, and POC through the evolution of a spring diatom bloom in the North Atlantic. *Deep Sea Research Part I: Oceanographic Research Papers*, 64:157–174, 2012.

Alkire, M. B., Lee, C., D'Asaro, E., Perry, M. J., Briggs, N., Cetinić, I., and Gray, A. Net community production and export from Seaglider measurements in the North Atlantic after the spring bloom. *Journal of Geophysical Research: Oceans*, 119(9):6121–6139, 2014.

Álvarez, M., Sanleón-Bartolomé, H., Tanhua, T., Mintrop, L., Luchetta, A., Cantoni, C., Schroeder, K., and Civitarese, G. The CO_2 system in the Mediterranean Sea: a basin wide perspective. *Ocean Science*, 10(1):69–92, 2014.

Anderson, L. A. On the hydrogen and oxygen content of marine phytoplankton. *Deep sea research part I: Oceanographic research papers*, 42(9):1675–1680, 1995.

Antoine, D., d'Ortenzio, F., Hooker, S. B., Bécu, G., Gentili, B., Tailliez, D., and Scott, A. J. Assessment of uncertainty in the ocean reflectance determined by three satellite ocean color sensors (MERIS, SeaWiFS and MODIS-A) at an offshore site in the Mediterranean Sea (BOUSSOLE project). *Journal of Geophysical Research: Oceans*, 113(C7), 2008.

Arrigo, K. R., van Dijken, G. L., and Bushinsky, S. Primary production in the Southern Ocean, 1997–2006. *Journal of Geophysical Research: Oceans*, 113(C8), 2008.

Aßmann, S., Frank, C., and Körtzinger, A. Spectrophotometric high-precision seawater pH determination for use in underway measuring systems. *Ocean Science*, 7(5):597–607, 2011.

Avril, B. DOC dynamics in the northwestern Mediterranean Sea (DYFAMED site). *Deep Sea Research Part II: Topical Studies in Oceanography*, 49(11):2163–2182, 2002.

Azov, Y. Eastern Mediterranean—a marine desert? *Marine Pollution Bulletin*, 23:225–232, 1991.

Ballantyne IV, F., Schofield, O. M., and Levin, S. A. The emergence of regularity and variability in marine ecosystems: the combined role of physics, chemistry and biology. *Scientia Marina*, 75(4):719–731, 2011.

Bates, N. R., Best, M. H., and Hansell, D. A. Spatio-temporal distribution of dissolved inorganic carbon and net community production in the Chukchi and Beaufort Seas. *Deep Sea Research Part II: Topical Studies in Oceanography*, 52(24):3303–3323, 2005.

Bates, N., Best, M., Neely, K., Garley, R., Dickson, A., and Johnson, R. Detecting anthropogenic carbon dioxide uptake and ocean acidification in the North Atlantic Ocean. *Biogeosciences*, 9(7):2509–2522, 2012.

Bendschneider, K. and Robinson, R. J. A new spectrophotometric method for the determination of nitrite in sea water. 1952.

Binetti, U. *Dissolved oxygen-based annual biological production from glider observations at the Porcupine Abyssal Plain (North Atlantic)*. PhD thesis, University of East Anglia, 2016.

Biswas, A. and Si, B. C. Model averaging for semivariogram model parameters. In *Advances in Agrophysical Research*. InTech, 2013.

Bittig, H. C. and Körtzinger, A. Tackling oxygen optode drift: Near-surface and in-air oxygen optode measurements on a float provide an accurate in situ reference. *Journal of Atmospheric and Oceanic Technology*, 32(8):1536–1543, 2015.

Bittig, H. C., Fiedler, B., Scholz, R., Krahmann, G., and Körtzinger, A. Time response of oxygen optodes on profiling platforms and its dependence on flow speed and temperature. *Limnology and Oceanography: Methods*, 12(8):617–636, 2014.

Borghini, M., Bryden, H., Schroeder, K., Sparnocchia, S., and Vetrano, A. The mediterranean is becoming saltier. *Ocean Science*, 10(4):693–700, 2014.

Bosse, A., Testor, P., Mortier, L., Prieur, L., Taillandier, V., d'Ortenzio, F., and Coppola, L. Spreading of Levantine Intermediate Waters by submesoscale coherent vortices in the northwestern Mediterranean Sea as observed with gliders. *Journal of Geophysical Research: Oceans*, 120(3):1599–1622, 2015.

Brasseur, P., Beckers, J.-M., Brankart, J., and Schoenauen, R. Seasonal temperature and salinity fields in the Mediterranean Sea: climatological analyses of a historical data set. *Deep Sea Research Part I: Oceanographic Research Papers*, 43(2):159–192, 1996.

Bresnahan, P. J., Martz, T. R., Takeshita, Y., Johnson, K. S., and LaShomb, M. Best practices for autonomous measurement of seawater pH with the Honeywell Durafet. *Methods in Oceanography*, 9:44–60, 2014.

Byrne, R. H. and Breland, J. A. High precision multiwavelength pH determinations in seawater using cresol red. *Deep Sea Research Part A. Oceanographic Research Papers*, 36(5):803–810, 1989.

Caldeira, K. and Wickett, M. E. Oceanography: anthropogenic carbon and ocean ph. *Nature*, 425(6956):365, 2003.

Carlson, C. A., Ducklow, H. W., Hansell, D. A., and Smith, W. O. Organic carbon partitioning during spring phytoplankton blooms in the Ross Sea polynya and the Sargasso Sea. *Limnology and Oceanography*, 43(3):375–386, 1998.

Chavez, F. P., Sevadjian, J., Wahl, C., Friederich, J., and Friederich, G. E. Measurements of $p\mathrm{CO}_2$ and pH from an autonomous surface vehicle in a coastal upwelling system. *Deep Sea Research Part II: Topical Studies in Oceanography*, 2017.

Chelton, D. B., Deszoeke, R. A., Schlax, M. G., El Naggar, K., and Siwertz, N. Geographical variability of the first baroclinic rossby radius of deformation. *Journal of Physical Oceanography*, 28(3):433–460, 1998.

Collins, M., Knutti, R., Arblaster, J., Dufresne, J.-L., Fichefet, T., Friedlingstein, P., Gao, X., Gutowski, W., Johns, T., Krinner, G., et al. Long-term climate change: projections, commitments and irreversibility. 2013.

Copin-Montégut, C. Consumption and production on scales of a few days of inorganic carbon, nitrate and oxygen by the planktonic community: results of continuous measurements at the Dyfamed station in the northwestern Mediterranean Sea (May 1995). *Deep Sea Research Part I: Oceanographic Research Papers*, 47(3):447–477, 2000.

Copin-Montégut, C. and Bégovic, M. Distributions of carbonate properties and oxygen along the water column (0–2000m) in the central part of the NW Mediterranean Sea (Dyfamed site): influence of winter vertical mixing on air–sea CO_2 and O_2 exchanges. *Deep Sea Research Part II: Topical Studies in Oceanography*, 49(11):2049–2066, 2002.

Copin-Montégut, C., Bégovic, M., and Merlivat, L. Variability of the partial pressure of CO_2 on diel to annual time scales in the Northwestern Mediterranean Sea. *Marine Chemistry*, 85(3):169–189, 2004.

Copin-Montégut, G. and Avril, B. Vertical distribution and temporal variation of dissolved organic carbon in the North-Western Mediterranean Sea. *Deep Sea Research Part I: Oceanographic Research Papers*, 40(10):1963–1972, 1993.

Coppola, L., Legendre, L., Lefevre, D., Prieur, L., Taillandier, V., and Riquier, E. D. Seasonal and inter–annual variations of dissolved oxygen in the northwestern Mediterranean Sea (DYFAMED site). *Progress in Oceanography*, 2018.

Cornwall, C. E., Hepburn, C. D., McGraw, C. M., Currie, K. I., Pilditch, C. A., Hunter, K. A., Boyd, P. W., and Hurd, C. L. Diurnal fluctuations in seawater pH influence the response of a calcifying macroalga to ocean acidification. *Proceedings of the Royal Society of London B: Biological Sciences*, 280(1772):20132201, 2013.

Cressie, N. Fitting variogram models by weighted least squares. *Journal of the International Association for Mathematical Geology*, 17(5):563–586, 1985.

Cressie, N. and Hawkins, D. M. Robust estimation of the variogram: I. *Journal of the International Association for Mathematical Geology*, 12(2):115–125, 1980.

Curry, R., Dickson, B., and Yashayaev, I. A change in the freshwater balance of the Atlantic Ocean over the past four decades. *Nature*, 426(6968):826, 2003.

Cyr, F., Tedetti, M., Besson, F., Beguery, L., Doglioli, A. M., Petrenko, A. A., and Goutx, M. A new glider-compatible optical sensor for dissolved organic matter measurements: test case from the NW Mediterranean Sea. *Frontiers in Marine Science*, 4:89, 2017.

de Fommervault, O. P., Migon, C., d'Alcalà, M. R., Coppola, L., et al. Temporal variability of nutrient concentrations in the northwestern Mediterranean sea (DYFAMED time-series station). *Deep Sea Research Part I: Oceanographic Research Papers*, 100:1–12, 2015.

Denman, K. L. and Abbott, M. R. Time evolution of surface chlorophyll patterns from cross-spectrum analysis of satellite color images. *Journal of Geophysical Research: Oceans*, 93(C6):6789–6798, 1988.

Dickson, A. pH scales and proton-transfer reactions in saline media such as sea water. *Geochemica et Cosmochimica Acta*, 48(11):2299–2308, 1984.

Dickson, A. and Millero, F. J. A comparison of the equilibrium constants for the dissociation of carbonic acid in seawater media. *Deep Sea Research Part A. Oceanographic Research Papers*, 34(10):1733–1743, 1987.

Dickson, A. G. Thermodynamics of the dissociation of boric acid in synthetic seawater from 273.15 to 318.15 K. *Deep Sea Research Part A. Oceanographic Research Papers*, 37(5):755–766, 1990.

Dickson, A. G. The measurement of sea water pH. *Marine Chemistry*, 44(2):131–142, 1993.

Dickson, A. G., Sabine, C. L., Christian, J. R., et al. Guide to best practices for ocean CO_2 measurements. 2007.

Dobricic, S., Pinardi, N., Testor, P., and Send, U. Impact of data assimilation of glider observations in the Ionian Sea (Eastern Mediterranean). *Dynamics of Atmospheres and Oceans*, 50(1):78–92, 2010.

Doney, S. C., Glover, D. M., McCue, S. J., and Fuentes, M. Mesoscale variability of Sea-viewing Wide Field-of-view Sensor (seawifs) satellite ocean color: Global patterns and spatial scales. *Journal of Geophysical Research: Oceans*, 108(C2), 2003.

Doney, S. C., Fabry, V. J., Feely, R. A., and Kleypas, J. A. Ocean acidification: the other CO_2 problem. *Marine Science*, 1:169–192, 2009.

El Sayed, M. A., Aminot, A., and Kerouel, R. Nutrients and trace metals in the northwestern Mediterranean under coastal upwelling conditions. *Continental Shelf Research*, 14(5): 507–530, 1994.

Eriksen, C. C., Osse, T. J., Light, R. D., Wen, T., Lehman, T. W., Sabin, P. L., Ballard, J. W., and Chiodi, A. M. Seaglider: A long-range autonomous underwater vehicle for oceanographic research. *Oceanic Engineering, IEEE Journal of*, 26(4):424–436, 2001.

Estrada, M. Primary production in the northwestern Mediterranean. *Scientia Marina*, 60 (2):55–64, 1996.

Fabry, V. J., Seibel, B. A., Feely, R. A., and Orr, J. C. Impacts of ocean acidification on marine fauna and ecosystem processes. *ICES Journal of Marine Science: Journal du Conseil*, 65(3):414–432, 2008.

Flato, G., Marotzke, J., Abiodun, B., Braconnot, P., Chou, S. C., Collins, W., Cox, P., Driouech, F., Emori, S., Eyring, V., et al. Evaluation of climate models, 2013.

Flecha, S., Pérez, F. F., García-Lafuente, J., Sammartino, S., Ríos, A. F., and Huertas, I. E. Trends of pH decrease in the Mediterranean Sea through high frequency observational data: indication of ocean acidification in the basin. *Scientific reports*, 5, 2015.

Frajka-Williams, E., Eriksen, C. C., Rhines, P. B., and Harcourt, R. R. Determining vertical water velocities from Seaglider. *Journal of Atmospheric and Oceanic Technology*, 28 (12):1641–1656, 2011.

Friis, K., Körtzinger, A., and Wallace, D. W. The salinity normalization of marine inorganic carbon chemistry data. *Geophysical Research Letters*, 30(2), 2003.

Garau, B., Ruiz, S., Zhang, W. G., Pascual, A., Heslop, E., Kerfoot, J., and Tintoré, J. Thermal lag correction on Slocum CTD glider data. *Journal of Atmospheric and Oceanic Technology*, 28(9):1065–1071, 2011.

Garcia, H. E. and Gordon, L. I. Oxygen solubility in seawater: Better fitting equations. *Limnology and oceanography*, 37(6):1307–1312, 1992.

Hall, T. M., Waugh, D. W., Haine, T. W., Robbins, P. E., and Khatiwala, S. Estimates of anthropogenic carbon in the Indian Ocean with allowance for mixing and time-varying air-sea CO_2 disequilibrium. *Global Biogeochemical Cycles*, 18(1), 2004.

Hedges, J., Baldock, J., Gélinas, Y., Lee, C., Peterson, M., and Wakeham, S. The biochemical and elemental compositions of marine plankton: A NMR perspective. *Marine Chemistry*, 78(1):47–63, 2002.

Hemming, M. P., Kaiser, J., Heywood, K. J., Bakker, D. C., Boutin, J., Shitashima, K., Lee, G., Legge, O., and Onken, R. Measuring pH variability using an experimental sensor on an underwater glider. *Ocean Science*, 13:427–442, 2017.

Hemsley, J. OBSERVATIONS PLATFORMS — Buoys. In North, G. R., Pyle, J., and Zhang, F., editors, *Encyclopedia of Atmospheric Sciences (Second Edition)*, pages 264 – 267. Academic Press, Oxford, second edition edition, 2003. ISBN 978-0-12-382225-3. doi: https://doi.org/10.1016/B978-0-12-382225-3.00256-5. URL `http://www.sciencedirect.com/science/article/pii/B9780123822253002565`.

Hofmann, G. E., Smith, J. E., Johnson, K. S., Send, U., Levin, L. A., Micheli, F., Paytan, A., Price, N. N., Peterson, B., Takeshita, Y., et al. High-frequency dynamics of ocean pH: a multi-ecosystem comparison. *PloS one*, 6(12):e28983, 2011.

Holte, J. and Talley, L. A new algorithm for finding mixed layer depths with applications to Argo data and subantarctic mode water formation. *Journal of Atmospheric and Oceanic Technology*, 26(9):1920–1939, 2009.

Hood, E. and Merlivat, L. Annual to interannual variations of fCO_2 in the northwestern Mediterranean Sea: Results from hourly measurements made by CARIOCA buoys, 1995-1997. *Journal of Marine Research*, 59(1):113–131, 2001.

Hu, C., Lee, Z., and Franz, B. Chlorophyll a algorithms for oligotrophic oceans: A novel approach based on three-band reflectance difference. *Journal of Geophysical Research: Oceans*, 117(C1), 2012.

Ignatiades, L. Scaling the trophic status of the aegean sea, eastern mediterranean. *Journal of Sea Research*, 54(1):51–57, 2005.

Johnson, K. M., King, A. E., and Sieburth, J. M. Coulometric TCO_2 analyses for marine studies; an introduction. *Marine Chemistry*, 16(1):61–82, 1985.

Johnson, K. S., Jannasch, H. W., Coletti, L. J., Elrod, V. A., Martz, T. R., Takeshita, Y., Carlson, R. J., and Connery, J. G. Deep-Sea DuraFET: A pressure tolerant pH sensor designed for global sensor networks. *Analytical Chemistry*, 88(6):3249–3256, 2016.

Johnson, K. S., Plant, J. N., Coletti, L. J., Jannasch, H. W., Sakamoto, C. M., Riser, S. C., Swift, D. D., Williams, N. L., Boss, E., Haëntjens, N., et al. Biogeochemical sensor performance in the soccom profiling float array. *Journal of Geophysical Research: Oceans*, 122(8):6416–6436, 2017.

Joint, I., Doney, S. C., and Karl, D. M. Will ocean acidification affect marine microbes? *The ISME journal*, 5(1):1, 2011.

Jones, E. M., Doblin, M. A., Matear, R., and King, E. Assessing and evaluating the ocean-colour footprint of a regional observing system. *Journal of Marine Systems*, 143:49–61, 2015.

Journel, A. G. and Huijbregts, C. J. *Mining geostatistics*. Academic press, 1978.

Key, R. M., Tanhua, T., Olsen, A., Hoppema, M., Jutterström, S., Schirnick, C., Van Heuven, S., Lin, X., Wallace, D. W., and Mintrop, L. The CARINA data synthesis project: introduction and overview. *Earth System Science Data*, 2:105–121, 2010.

Knoll, M., Benecke, J., Russo, A., and Ampolo-Rella, M. Comparison of CTD measurements obtained by NRV Alliance and RV Planet during REP14-MED. Technical Report WTD71-0083/2015 WB 34 pp, 2015b.

Knoll, M., Borrione, I., Fiekas, H.-V., Funk, A., Hemming, M. P., Kaiser, J., Onken, R., Queste, B., and Russo, A. Hydrography and circulation west of Sardinia in June 2014. *Ocean Science*, 13(6):889–904, 2017.

Le Quéré, C., Moriarty, R., Andrew, R. M., Peters, G. P., Ciais, P., Friedlingstein, P., Jones, S. D., Sitch, S., Tans, P., Arneth, A., Boden, T. A., Bopp, L., Bozec, Y., Canadell, J. G., Chini, L. P., Chevallier, F., Cosca, C. E., Harris, I., Hoppema, M., Houghton, R. A., House, J. I., Jain, A. K., Johannessen, T., Kato, E., Keeling, R. F., Kitidis, V., Klein Goldewijk, K., Koven, C., Landa, C. S., Landschützer, P., Lenton, A., Lima, I. D., Marland, G., Mathis, J. T., Metzl, N., Nojiri, Y., Olsen, A., Ono, T., Peng, S., Peters, W., Pfeil, B., Poulter, B., Raupach, M. R., Regnier, P., Rödenbeck, C., Saito, S., Salisbury, J. E., Schuster, U., Schwinger, J., Séférian, R., Segschneider, J., Steinhoff, T., Stocker, B. D., Sutton, A. J., Takahashi, T., Tilbrook, B., van der Werf, G. R., Viovy, N., Wang, Y.-P., Wanninkhof, R., Wiltshire, A., and Zeng, N. Global carbon budget 2014. *Earth System Science Data*, 7(1):47–85, 2015. doi: 10.5194/essd-7-47-2015.

Le Quéré, C., Andrew, R. M., Friedlingstein, P., Sitch, S., Pongratz, J., Manning, A. C., Korsbakken, J. I., Peters, G. P., Canadell, J. G., Jackson, R. B., et al. Global Carbon Budget 2017. *Earth System Science Data*, 10(1):405–448, 2018.

Lee, K., Sabine, C. L., Tanhua, T., Kim, T.-W., Feely, R. A., and Kim, H.-C. Roles of marginal seas in absorbing and storing fossil fuel CO 2. *Energy & Environmental Science*, 4(4):1133–1146, 2011.

Lee, Z., Weidemann, A., Kindle, J., Arnone, R., Carder, K. L., and Davis, C. Euphotic zone depth: Its derivation and implication to ocean-color remote sensing. *Journal of Geophysical Research: Oceans*, 112(C3), 2007.

Lefevre, D., Denis, M., Lambert, C., and Miquel, J.-C. Is DOC the main source of organic matter remineralization in the ocean water column? *Journal of Marine Systems*, 7(2-4): 281–291, 1996.

Lefèvre, N. and Merlivat, L. Carbon and oxygen net community production in the eastern tropical Atlantic estimated from a moored buoy. *Global Biogeochemical Cycles*, 26(1), 2012.

Legaard, K. R. and Thomas, A. C. Spatial patterns of intraseasonal variability of chlorophyll and sea surface temperature in the California Current. *Journal of Geophysical Research: Oceans*, 112(C9), 2007.

Liao, H.-K., Wu, C.-L., Chou, J.-C., Chung, W.-Y., Sun, T.-P., and Hsiung, S.-K. Multi-structure ion sensitive field effect transistor with a metal light shield. *Sensors and Actuators B: Chemical*, 61(1):1–5, 1999.

Lozier, M. S. and Stewart, N. M. On the temporally varying northward penetration of Mediterranean Overflow Water and eastward penetration of Labrador Sea Water. *Journal of Physical Oceanography*, 38(9):2097–2103, 2008.

Mahadevan, A. and Campbell, J. Biogeochemical patchiness at the sea surface. *Geophysical Research Letters*, 29(19):32–1, 2002.

Martin, A. Phytoplankton patchiness: the role of lateral stirring and mixing. *Progress in oceanography*, 57(2):125–174, 2003.

Marty, J.-C. and Chiavérini, J. Seasonal and interannual variations in phytoplankton production at DYFAMED time-series station, northwestern Mediterranean Sea. *Deep Sea Research Part II: Topical Studies in Oceanography*, 49(11):2017–2030, 2002.

Martz, T. R., Carr, J. J., French, C. R., and DeGrandpre, M. D. A submersible autonomous sensor for spectrophotometric pH measurements of natural waters. *Analytical chemistry*, 75(8):1844–1850, 2003.

Martz, T. R., Connery, J. G., and Johnson, K. S. Testing the Honeywell Durafet® for seawater pH applications. *Limnology and Oceanography: Methods*, 8(5):172–184, 2010.

Mayot, N., D'Ortenzio, F., Uitz, J., Gentili, B., Ras, J., Vellucci, V., Golbol, M., Antoine, D., and Claustre, H. Influence of the phytoplankton community structure on the spring and annual primary production in the northwestern mediterranean sea. *Journal of Geophysical Research: Oceans*, 122(12):9918–9936, 2017.

McGranahan, G., Balk, D., and Anderson, B. The rising tide: assessing the risks of climate change and human settlements in low elevation coastal zones. *Environment and urbanization*, 19(1):17–37, 2007.

McNeil, C. L. and D'Asaro, E. A. A calibration equation for oxygen optodes based on physical properties of the sensing foil. *Limnol. Oceanogr.: Methods*, 12:139–154, 2014.

Mehrbach, C., Culberson, C., Hawley, J., and Pytkowics, R. Measurement of the apparent dissociation constants of carbonic acid in seawater at atmospheric pressure. *Limnology and Oceanography*, 18(6), 1973.

Merlivat, L., Boutin, J., and Antoine, D. Roles of biological and physical processes in driving seasonal air–sea CO_2 flux in the southern ocean: new insights from CARIOCA pCO_2. *Journal of Marine Systems*, 147:9–20, 2014.

Merlivat, L., Boutin, J., Antoine, D., Beaumont, L., Golbol, M., and Vellucci, V. Increase of dissolved inorganic carbon and decrease in pH in near-surface waters in the Mediterranean Sea during the past two decades. *Biogeosciences*, 15(18):5653–5662, 2018.

Millero, F. J. Thermodynamics of the carbon dioxide system in the oceans. *Geochimica et Cosmochimica Acta*, 59(4):661–677, 1995.

Millot, C. Circulation in the western Mediterranean Sea. *Journal of Marine Systems*, 20(1): 423–442, 1999.

Millot, C. and Taupier-Letage, I. Circulation in the Mediterranean Sea. In *The Mediterranean Sea*, pages 29–66. Springer, 2005.

Mintrop, L., Pérez, F. F., González-Dávila, M., Santana-Casiano, M., and Körtzinger, A. Alkalinity determination by potentiometry: Intercalibration using three different methods. 2000.

Miquel, J.-C., Martín, J., Gasser, B., Rodriguez-y Baena, A., Toubal, T., and Fowler, S. W. Dynamics of particle flux and carbon export in the northwestern Mediterranean Sea: A two decade time-series study at the DYFAMED site. *Progress in oceanography*, 91(4): 461–481, 2011.

Murphy, J. and Riley, J. P. A modified single solution method for the determination of phosphate in natural waters. *Analytica chimica acta*, 27:31–36, 1962.

Niewiadomska, K., Claustre, H., Prieur, L., and d'Ortenzio, F. Submesoscale physical-biogeochemical coupling across the Ligurian current (northwestern Mediterranean) using a bio-optical glider. *Limnology and Oceanography*, 53(5part2):2210–2225, 2008.

Okazaki, R. R., Sutton, A. J., Feely, R. A., Dickson, A. G., Alin, S. R., Sabine, C. L., Bunje, P. M., and Virmani, J. I. Evaluation of marine ph sensors under controlled and natural conditions for the wendy schmidt ocean health xprize. *Limnology and Oceanography: Methods*, 15(6):586–600, 2017.

Oke, P. and Sakov, P. Assessing the footprint of a regional ocean observing system. *Journal of Marine Systems*, 105:30–51, 2012.

Olita, A., Ribotti, A., Fazioli, L., Perilli, A., and Sorgente, R. Surface circulation and upwelling in the Sardinia Sea: A numerical study. *Continental Shelf Research*, 71:95–108, 2013.

Onken, R., Fiekas, H.-V., Beguery, L., Borrione, I., Funk, A., Hemming, M., Hernandez-Lasheras, J., Heywood, K. J., Kaiser, J., Knoll, M., et al. High-resolution observations in the western Mediterranean Sea: the REP14-MED experiment. *Ocean Science*, 14(2): 321–335, 2018.

Orr, J., Epitalon, J.-M., and Gattuso, J.-P. Comparison of ten packages that compute ocean carbonate chemistry. *Biogeosciences*, 12(5):1483–1510, 2015.

Pastor, F., Valiente, J. A., and Palau, J. L. Sea surface temperature in the Mediterranean: Trends and spatial patterns (1982–2016). *Pure and Applied Geophysics*, pages 1–13, 2017.

Pingree, R., Maddock, L., and Butler, E. The influence of biological activity and physical stability in determining the chemical distributions of inorganic phosphate, silicate and nitrate. *Journal of the Marine Biological Association of the United Kingdom*, 57(4): 1065–1073, 1977.

Piterbarg, L., Taillandier, V., and Griffa, A. Investigating frontal variability from repeated glider transects in the Ligurian Current (North West Mediterranean Sea). *Journal of Marine Systems*, 129:381–395, 2014.

Porter, M., Inall, M., Hopkins, J., Palmer, M., Dale, A., Aleynik, D., Barth, J., Mahaffey, C., and Smeed, D. Glider observations of enhanced deep water upwelling at a shelf break canyon: A mechanism for cross-slope carbon and nutrient exchange. *Journal of Geophysical Research: Oceans*, 121(10):7575–7588, 2016.

Pujo-Pay, M., Conan, P., Oriol, L., Cornet-Barthaux, V., Falco, C., Ghiglione, J.-F., Goyet, C., Moutin, T., and Prieur, L. Integrated survey of elemental stoichiometry (c, n, p) from the western to eastern mediterranean sea. *Biogeosciences*, 8(4):883–899, 2011.

Queste, B. Y., Heywood, K. J., Kaiser, J., Lee, G., Matthews, A., Schmidtko, S., Walker-Brown, C., Woodward, S. W., et al. Deployments in extreme conditions: Pushing the boundaries of Seaglider capabilities. In *Autonomous Underwater Vehicles (AUV), 2012 IEEE/OES*, pages 1–7. IEEE, 2012.

Raven, J., Caldeira, K., Elderfield, H., Hoegh-Guldberg, O., Liss, P., Riebesell, U., Shepherd, J., Turley, C., and Watson, A. *Ocean acidification due to increasing atmospheric carbon dioxide*. The Royal Society, 2005.

Rhein, M., Rintoul, S., Aoki, S., Campos, E., Chambers, D., Feely, R., Gulev, S., Johnson, G., Josey, S., Kostianoy, A., et al. Chapter 3: Observations: Ocean. *Climate Change*, pages 255–315, 2013a.

Rhein, M. a., Rintoul, S. R., Aoki, S., Campos, E., Chambers, D., Feely, R. A., Gulev, S., Johnson, G., Josey, S., Kostianoy, A., et al. Observations: ocean. *Climate change*, pages 255–316, 2013b.

Ridame, C. and Guieu, C. Saharan input of phosphate to the oligotrophic water of the open western mediterranean sea. *Limnology and Oceanography*, 47(3):856–869, 2002.

Rivaro, P., Messa, R., Massolo, S., and Frache, R. Distributions of carbonate properties along the water column in the Mediterranean Sea: Spatial and temporal variations. *Marine Chemistry*, 121(1):236–245, 2010.

Roemmich, D. H., Davis, R. E., Riser, S. C., Owens, W. B., Molinari, R. L., Garzoli, S. L., and Johnson, G. C. The argo project. global ocean observations for understanding and prediction of climate variability. Technical report, DTIC Document, 2003.

Roquet, F., Madec, G., McDougall, T. J., and Barker, P. M. Accurate polynomial expressions for the density and specific volume of seawater using the TEOS-10 standard. *Ocean Modelling*, 90:29–43, 2015.

Roughan, M., Terrill, E. J., Largier, J. L., and Otero, M. P. Observations of divergence and upwelling around Point Loma, California. *Journal of Geophysical Research: Oceans*, 110(C4), 2005.

Rudnick, D. L. Ocean research enabled by underwater gliders. *Annual review of marine science*, 8:519–541, 2016.

Ruhl, H. A., André, M., Beranzoli, L., Çağatay, M. N., Colaço, A., Cannat, M., Dañobeitia, J. J., Favali, P., Géli, L., Gillooly, M., et al. Societal need for improved understanding of climate change, anthropogenic impacts, and geo-hazard warning drive development of ocean observatories in European Seas. *Progress in Oceanography*, 91(1):1–33, 2011.

Saba, G. K., Wright-Fairbanks, E., Miles, T. N., Chen, B., Cai, W.-J., Wang, K., Barnard, A. H., Branham, C. W., and Jones, C. P. Developing a profiling glider ph sensor for high resolution coastal ocean acidification monitoring. In *OCEANS 2018 MTS/IEEE Charleston*, pages 1–8. IEEE, 2018.

Schaeffer, A., Roughan, M., Jones, E. M., and White, D. Physical and biogeochemical spatial scales of variability in the East Australian Current separation from shelf glider measurements. *Biogeosciences*, 13(6):1967–1975, 2016.

Schneider, A., Tanhua, T., Körtzinger, A., and Wallace, D. W. High anthropogenic carbon content in the eastern Mediterranean. *Journal of Geophysical Research: Oceans*, 115 (C12), 2010.

Schofield, O., Kohut, J., Aragon, D., Creed, L., Graver, J., Haldeman, C., Kerfoot, J., Roarty, H., Jones, C., Webb, D., et al. Slocum gliders: Robust and ready. *Journal of Field Robotics*, (6):473–485.

Schroeder, K., Chiggiato, J., Bryden, H., Borghini, M., and Ismail, S. B. Abrupt climate shift in the western Mediterranean Sea. *Scientific reports*, 6:23009, 2016.

Seidel, M. P., DeGrandpre, M. D., and Dickson, A. G. A sensor for in situ indicator-based measurements of seawater ph. *Marine chemistry*, 109(1-2):18–28, 2008.

Shaltout, M. and Omstedt, A. Recent sea surface temperature trends and future scenarios for the Mediterranean Sea. *Oceanologia*, 56(3):411–443, 2014.

Sherman, J., Davis, R. E., Owens, W., and Valdes, J. The autonomous underwater glider ”spray”. *IEEE Journal of Oceanic Engineering*, 26(4):437–446, 2001.

Shitashima, K., Kyo, M., Koike, Y., and Henmi, H. Development of in situ pH sensor using ISFET. In *Underwater Technology, 2002. Proceedings of the 2002 International Symposium on*, pages 106–108. IEEE, 2002.

Shitashima, K. Evolution of compact electrochemical in-situ pH-pCO_2 sensor using ISFET-pH electrode. In *Oceans 2010 MTS/IEEE Seattle*, pages 1–4, 2010.

Shitashima, K., Maeda, Y., Koike, Y., and Ohsumi, T. Natural analogue of the rise and dissolution of liquid co2 in the ocean. *International journal of greenhouse gas control*, 2 (1):95–104, 2008.

Shitashima, K., Maeda, Y., and Ohsumi, T. Development of detection and monitoring techniques of CO_2 leakage from seafloor in sub-seabed CO_2 storage. *Applied geochemistry*, 30:114–124, 2013.

Siokou-Frangou, I., Christaki, U., Mazzocchi, M. G., Montresor, M., Ribera d'Alcalà, M., Vaqué, D., and Zingone, A. Plankton in the open mediterranean sea: a review. 2010.

Skliris, N., Marsh, R., Josey, S. A., Good, S. A., Liu, C., and Allan, R. P. Salinity changes in the World Ocean since 1950 in relation to changing surface freshwater fluxes. *Climate dynamics*, 43(3-4):709–736, 2014.

Steele, J. H. *Spatial pattern in plankton communities*, volume 3. Springer Science & Business Media, 1978.

Stommel, H. The slocum mission. *Oceanography*, 2(1):22–25, 1989.

Stramski, D., Boss, E., Bogucki, D., and Voss, K. J. The role of seawater constituents in light backscattering in the ocean. *Progress in Oceanography*, 61(1):27–56, 2004.

Strickland, J. D. and Parsons, T. R. A practical handbook of seawater analysis. 1972.

Sverdrup, H. On vernal blooming of phytoplankton. *J. Conseil Exp. Mer*, 18:287–295, 1953.

Takahashi, T., Olafsson, J., Goddard, J. G., Chipman, D. W., and Sutherland, S. Seasonal variation of CO_2 and nutrients in the high-latitude surface oceans: A comparative study. *Global Biogeochemical Cycles*, 7(4):843–878, 1993.

Takahashi, T., Sutherland, S. C., Sweeney, C., Poisson, A., Metzl, N., Tilbrook, B., Bates, N., Wanninkhof, R., Feely, R. A., Sabine, C., et al. Global sea–air CO_2 flux based on climatological surface ocean $p\mathrm{CO}_2$, and seasonal biological and temperature effects. *Deep Sea Research Part II: Topical Studies in Oceanography*, 49(9):1601–1622, 2002.

Takahashi, T., Sutherland, S. C., Wanninkhof, R., Sweeney, C., Feely, R. A., Chipman, D. W., Hales, B., Friederich, G., Chavez, F., Sabine, C., et al. Climatological mean and decadal change in surface ocean $p\mathrm{CO}_2$, and net sea–air CO_2 flux over the global oceans. *Deep Sea Research Part II: Topical Studies in Oceanography*, 56(8-10):554–577, 2009.

Takeshita, Y., Martz, T. R., Johnson, K. S., and Dickson, A. G. Characterization of an ion sensitive field effect transistor and chloride ion selective electrodes for pH measurements in seawater. *Analytical chemistry*, 86(22):11189–11195, 2014.

Tandeo, P., Autret, E., Chapron, B., Fablet, R., and Garello, R. SST spatial anisotropic covariances from METOP-AVHRR data. *Remote Sensing of Environment*, 141:144–148, 2014.

Todd, R. E., Gawarkiewicz, G. G., and Owens, W. B. Horizontal scales of variability over the Middle Atlantic Bight shelf break and continental rise from finescale observations. *Journal of Physical Oceanography*, 43(1):222–230, 2013.

Touratier, F. and Goyet, C. Impact of the Eastern Mediterranean Transient on the distribution of anthropogenic CO_2 and first estimate of acidification for the Mediterranean Sea. *Deep Sea Research Part I: Oceanographic Research Papers*, 58 (1):1–15, 2011.

Uppström, L. R. The boron/chlorinity ratio of deep-sea water from the Pacific Ocean. In *Deep Sea Research and Oceanographic Abstracts*, volume 21, pages 161–162. Elsevier, 1974.

Van Der Loeff, M. M. R., Friedrich, J., and Bathmann, U. V. Carbon export during the spring bloom at the Antarctic Polar Front, determined with the natural tracer 234 Th. *Deep Sea Research Part II: Topical Studies in Oceanography*, 44(1):457–478, 1997.

Van Heuven, S., Pierrot, D., Rae, J., Lewis, E., and Wallace, D. MATLAB program developed for CO_2 system calculations, ORNL/CDIAC-105b, Carbon Dioxide Inf. *Anal. Cent., Oak Ridge Natl. Lab., US DOE, Oak Ridge, Tennessee*, 2011.

Wanninkhof, R. Relationship between wind speed and gas exchange over the ocean revisited. *Limnology and Oceanography: Methods*, 12(6):351–362, 2014.

Wanninkhof, R. and Thoning, K. Measurement of fugacity of CO_2 in surface water using continuous and discrete sampling methods. *Marine Chemistry*, 44(2-4):189–204, 1993.

Webb, D. C., Simonetti, P. J., and Jones, C. P. SLOCUM: An underwater glider propelled by environmental energy. *IEEE Journal of oceanic engineering*, 26(4):447–452, 2001.

Weiss, R. Carbon dioxide in water and seawater: the solubility of a non-ideal gas. *Marine chemistry*, 2(3):203–215, 1974.

Williams, R. G. and Follows, M. J. *Ocean dynamics and the carbon cycle*. Cambridge University Press, first edition edition, 2011.

Wlodarski, W., Bergveld, P., and Voorthuyzen, J. Threshold voltage variations in n-channel MOS transistors and MOSFET-based sensors due to optical radiation. *Sensors and Actuators*, 9(4):313–321, 1986.

Woolf, D. K. and Thorpe, S. Bubbles and the air-sea exchange of gases in near-saturation conditions. *Journal of Marine Research*, 49(3):435–466, 1991.

Yao, K. M., Marcou, O., Goyet, C., Guglielmi, V., Touratier, F., and Savy, J.-P. Time variability of the north-western Mediterranean Sea pH over 1995–2011. *Marine environmental research*, 116:51–60, 2016.

Yates, K. K., Dufore, C., Smiley, N., Jackson, C., and Halley, R. B. Diurnal variation of oxygen and carbonate system parameters in Tampa Bay and Florida Bay. *Marine Chemistry*, 104(1):110–124, 2007.

Yoder, J. A., McClain, C. R., Blanton, J. O., and Oeymay, L.-Y. Spatial scales in CZCS-chlorophyll imagery of the southeastern US continental shelf 1. *Limnology and Oceanography*, 32(4):929–941, 1987.

Zavatarielli, M. and Mellor, G. L. A numerical study of the Mediterranean Sea circulation. *Journal of Physical Oceanography*, 25(6):1384–1414, 1995.

Zeebe, R. E. and Wolf-Gladrow, D. A. *CO2 in seawater: equilibrium, kinetics, isotopes*. Gulf Professional Publishing, 2001.

Zunino, P., Schroeder, K., Vargas-Yánez, M., Gasparini, G., Coppola, L., García-Martínez, M., and Moya-Ruiz, F. Effects of the Western Mediterranean Transition on the resident water masses: Pure warming, pure freshening and pure heaving. *Journal of Marine Systems*, 96:15–23, 2012.

A

Supplementary Figures

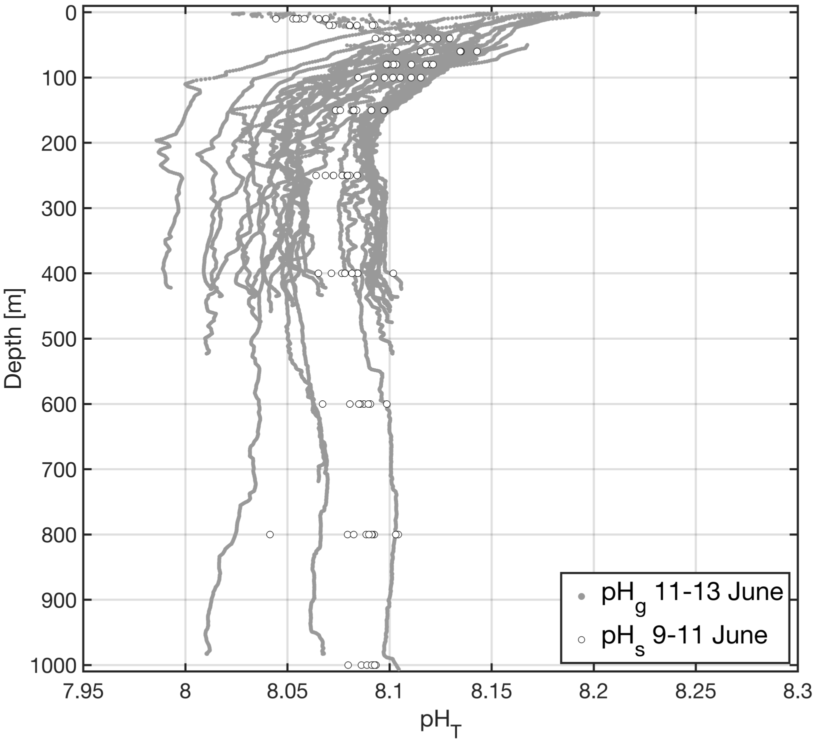

Figure A.1: pH obtained by the glider ISFET sensor (pH_g, grey) between June 11 and 13 is compared with mean pH obtained by the ship (pH_s, white) between June 9 and 11.

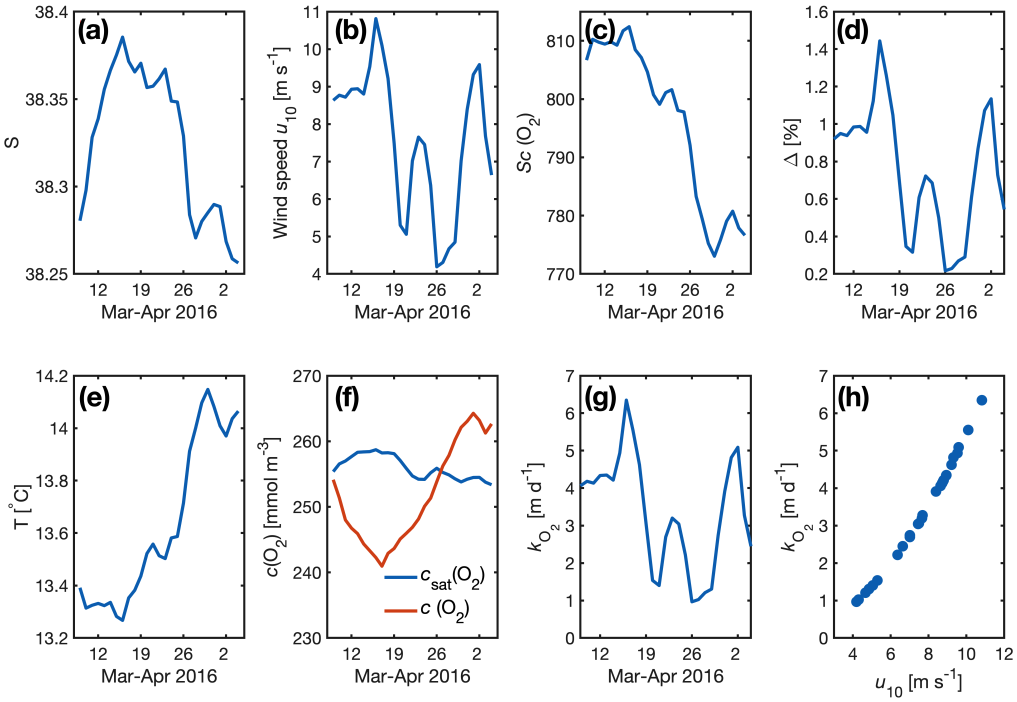

Figure A.2: Glider (a) salinity (S), (e) *in situ* temperature, and (f) dissolved oxygen concentrations ($c(\mathrm{O_2})$) along with the concentration of saturation at the surface ($c_{\mathrm{sat}}(\mathrm{O_2})$), (b) wind speed ($u_{10}$) at 10 m collected at the meteorological Azur buoy (Fig. 1), (c) calculated Schmidt number, (d) bubble saturation, and (g) $\mathrm{O_2}$ gas transfer velocity ($K_{\mathrm{O_2}}$)). (h) The relationship between u_{10} and $K_{\mathrm{O_2}}$.

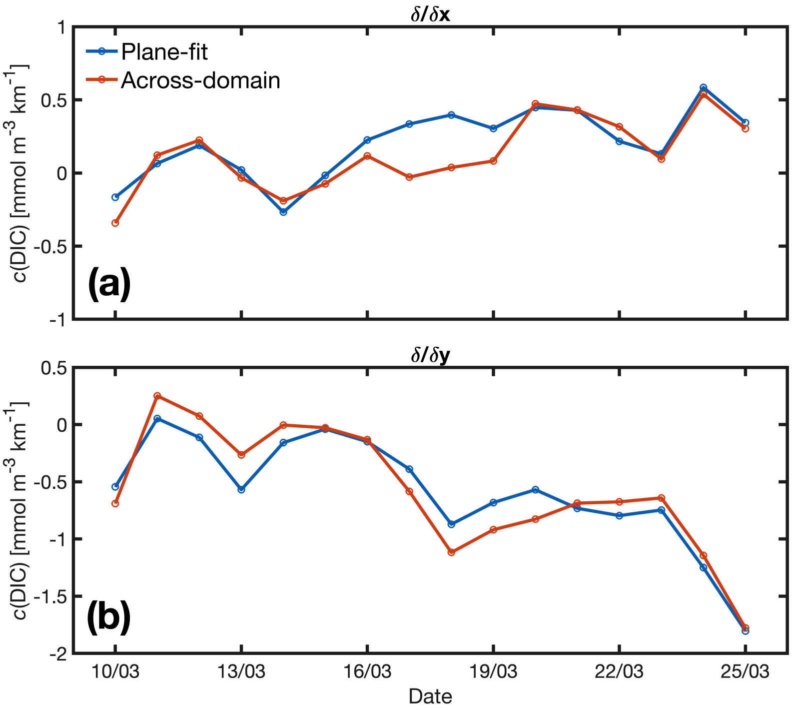

Figure A.3: (a) Zonal and (b) meridional horizontal c(DIC) gradients calculated using the plane-fit (blue) and Across-domain (red) methods within a 4 day moving time window.

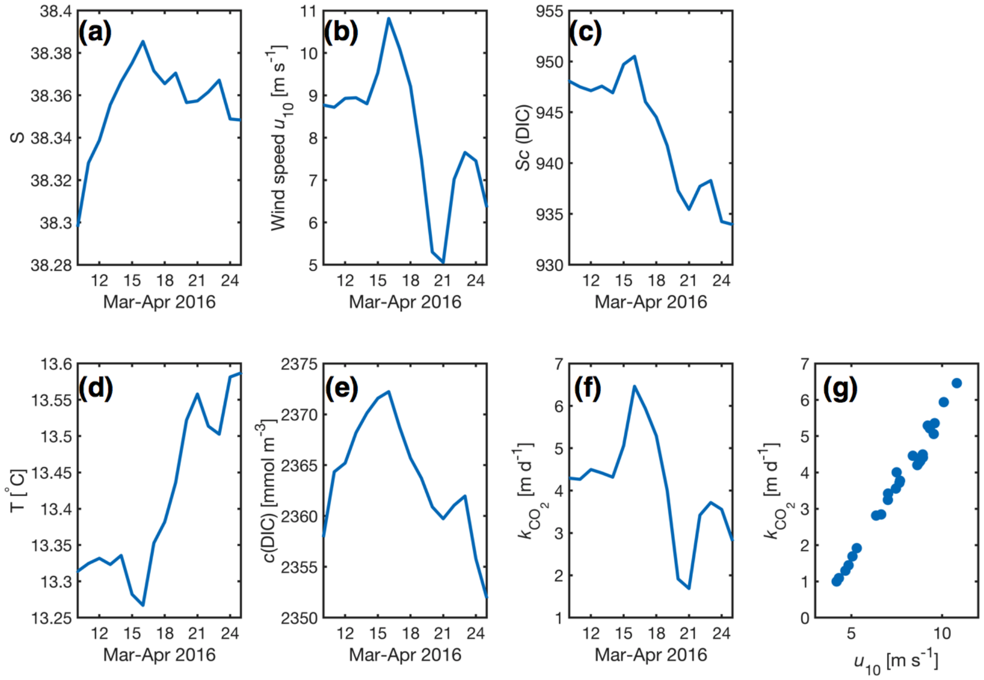

Figure A.4: Glider (a) salinity (S), (d) *in situ* temperature, and (e) dissolved inorganic carbon concentrations (c(DIC)), (b) wind speed (u_{10}) at 10 m collected at the meteorological Azur buoy (Fig. 1), (c) calculated Schmidt number, and (g) CO_2 gas transfer velocity (K_{CO_2})). (h) The relationship between u_{10} and K_{CO_2}.

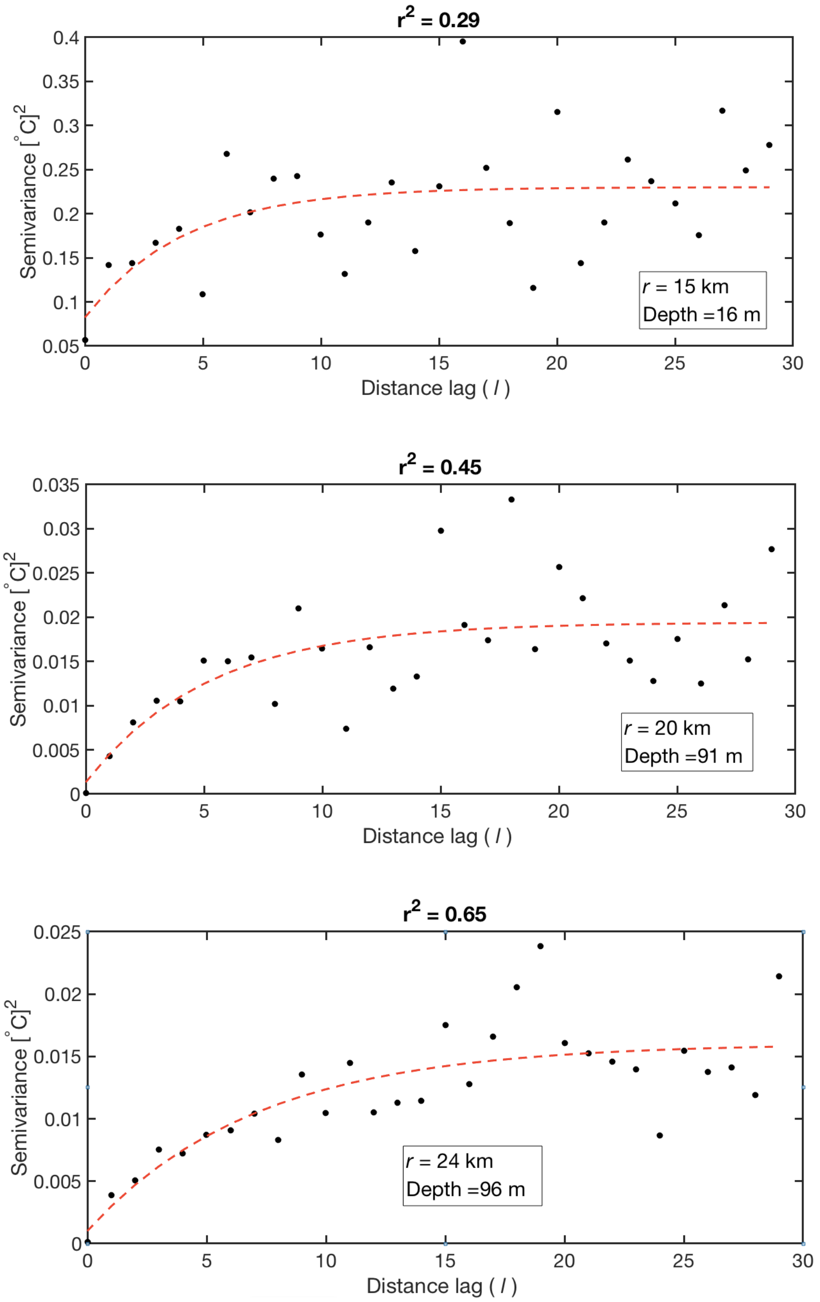

Figure A.5: Examples of temperature domain-wide semivariograms with exponential model fits with different resulting r^2 statistics. The corresponding ranges (r) and the depth level (metres) of the semivariogram is also displayed.

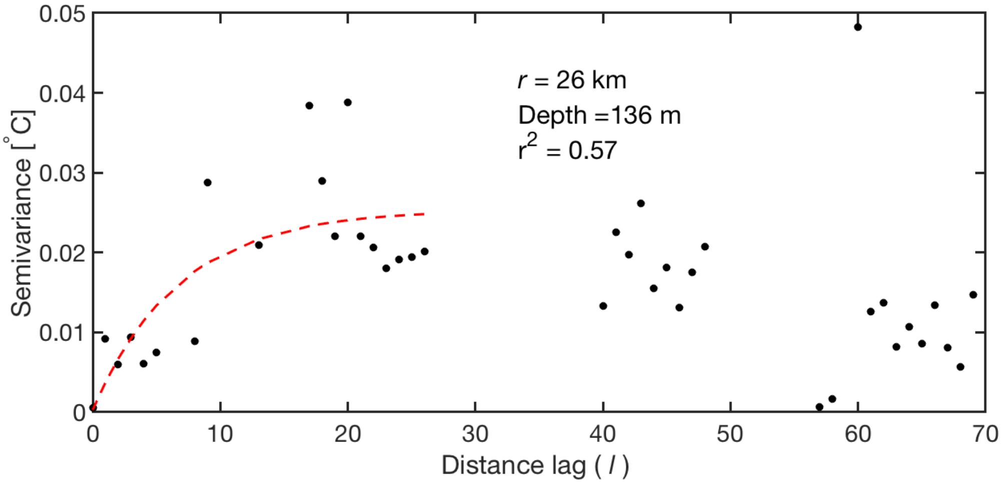

Figure A.6: An example of a temperature semivariogram using R14 values in a latitude direction. The exponential model fit is plotted, and the resulting range, depth, and r^2 statistic is shown.